

First direct mass measurement of the two and four neutron halos ${}^6\text{He}$ and ${}^8\text{He}$ using the TITAN Penning trap mass spectrometer

by

Maxime Brodeur

B.Sc., L'Université de Montréal, 2004
M.Sc., The University of British Columbia, 2006

A THESIS SUBMITTED IN PARTIAL FULFILLMENT OF
THE REQUIREMENTS FOR THE DEGREE OF

DOCTOR OF PHILOSOPHY

in

The Faculty of Graduate Studies

(Physics)

THE UNIVERSITY OF BRITISH COLUMBIA

(Vancouver)

April, 2010

© Maxime Brodeur 2009

Abstract

Neutron halo nuclei are distinguished by an extended matter radius and a small neutron separation energy compared to other nuclei. They are comprised of a core surrounded by at least one loosely bound neutron forming a halo structure. The size of the core is associated with the charge radius while the extent of the diffuse halo region, owing to quantum mechanical leakage of the valence neutron(s) wavefunction, depends exponentially on their separation energy. Predicting accurately the extreme behaviour of these nuclei is challenging for nuclear theory. These nuclei provide an ideal testing grounds of nuclear theory, leading to a deeper understanding of the strong force and nuclear interactions. Halo nuclei can be found amongst light nuclei and hence have few ($A \sim 10$) nucleons. This makes them treatable using ab-initio methods. To test these theoretical approaches and consequently refine our knowledge of the nucleus, one requires both precise and accurate experimental data, such as ground state properties: masses (or separation energies) and sizes (charge and matter radii). In this thesis we present the mass measurement of the two- and four-neutrons halo ${}^{6,8}\text{He}$ ($t_{1/2} = 808$ ms, 119 ms respectively) using the TITAN Penning trap as well as systematic studies of this system. The obtained mass are $m({}^6\text{He}) = 6\,018\,885.883(57)$ u and $m({}^8\text{He}) = 8\,033\,934.435(114)$ u. These values show deviations with literature of 4.0 and 1.7σ . Using our new masses, we re-evaluated the charge radius and obtained $\langle r^2 \rangle_c^{1/2}({}^6\text{He}) = 2.056(10)$ fm and $\langle r^2 \rangle_c^{1/2}({}^8\text{He}) = 1.955(18)$ fm, which correspond to an improvement in the precision of 9% and 36% respectively. Using the charge radii and the binding energies of ${}^{6,8}\text{He}$, obtained from our more precise and accurate masses, we show that one can test the predictions of advanced ab-initio nuclear theories for these extreme systems. Using such comparison, we point to the needs of three-body interactions in order to explain the experimental observables.

Table of contents

Abstract	ii
Table of contents	iii
List of tables	vi
List of figures	viii
Acknowledgements	xi
1 Introduction	1
1.1 Nuclear halos	2
1.1.1 Motivations for the mass measurement of ${}^6\text{He}$ and ${}^8\text{He}$	5
1.1.2 The different types of halo nuclei and characteristics of ${}^6\text{He}$ and ${}^8\text{He}$	8
1.1.2.1 Neutron separation energies	9
1.1.2.2 Cross section comparison	12
1.1.2.3 Charge radius of halo nuclei	14
1.1.2.4 ${}^6\text{He}$ and ${}^8\text{He}$ charge radius measurements	15
1.2 Nuclear halo and nuclear models	17
1.2.1 Nuclear potential for ab-initio methods	18
1.2.2 The construction of the wave function	22
1.2.2.1 Green function Monte Carlo	22
1.2.2.2 No-core shell model	23
1.2.2.3 Hyperspherical harmonics expansion	24
1.2.2.4 Coupled cluster theory	26
1.2.3 Summary of the methods and need for three-nucleon potential	27
1.3 Other motivations for precise mass measurement: change in nuclear structure	28
1.4 Other motivations for precise mass measurement: test of the CKM matrix unitarity	30

Table of contents

2	The experimental setup	35
2.1	Beam production and separation at ISAC	36
2.2	Beam preparation: the radio-frequency quadrupole (RFQ) cooler and buncher	38
2.3	Beam preparation: beam transport to the Penning trap	40
2.4	Beam preparation: the electron beam ion trap (EBIT)	44
2.5	The mass measurement Penning trap	45
2.5.1	Three-dimensional confinement	46
2.5.2	The TITAN Penning trap electrode structure	47
2.5.3	Ion motion in an ideal Penning trap	48
2.5.4	The TOF-ICR mass measurement technique	52
2.5.5	The mass determination	56
3	Systematic studies of the TITAN Penning trap and data analysis	60
3.1	Frequency ratio deviation for a real Penning trap	60
3.2	Trapping potentials of a real Penning trap and trap-related systematic error	61
3.2.1	Penning trap magnetic field inhomogeneities	63
3.2.2	Harmonic distortion and misalignment of the magnetic field axis	64
3.2.2.1	Harmonic distortion of the electrical potential in the Penning trap	66
3.2.2.2	Misalignment of the magnetic field axis with the Penning trap electrode geometry	70
3.2.3	Non-harmonic imperfections of the trapping potential	73
3.3	Compensation of the Penning trap electrical potential	74
3.3.1	Calculated correction tube and guard potentials	75
3.3.2	Penning trap compensation using a dipole excitation	80
3.3.3	Penning trap compensation using a quadrupole excitation	83
3.3.4	Effect of the incomplete compensation of the trapping potential of the TITAN Penning trap on the measured frequency ratio	88
3.4	TITAN Penning trap trap-independent systematic errors	90
3.4.1	Effects of nonlinear magnetic field fluctuations	90
3.4.2	Effect of ion-ion interaction in the Penning trap	92
3.4.3	Relativistic effects on the cyclotron frequency	95
3.4.3.1	Case study of relativistic shift at the TITAN Penning trap: ${}^6\text{Li}$	96

Table of contents

3.4.3.2	Case study of relativistic shift at the TITAN Penning trap: ${}^6\text{He}$ and ${}^8\text{He}$	98
3.5	Summary of the systematic errors	102
3.6	Benchmark high-precision mass measurement at TITAN Penning trap: ${}^6\text{Li}$	103
3.6.1	The ${}^6\text{Li}$ mass measurement	104
4	${}^6\text{He}$ and ${}^8\text{He}$ mass measurement results and discussion	107
4.1	First ${}^8\text{He}$ mass measurement	107
4.2	Second ${}^8\text{He}$ and the ${}^6\text{He}$ mass measurements	109
4.3	Calculation of the binding energy and point-proton radius for ${}^6\text{He}$ and ${}^8\text{He}$	113
4.3.1	Binding and two-neutron separation energy of ${}^{6,8}\text{He}$	114
4.3.2	Charge and point-proton radius of ${}^{6,8}\text{He}$	114
4.4	Comparison of the results for ${}^{6,8}\text{He}$ with theory	116
4.4.1	Green Function Monte-Carlo results for ${}^6\text{He}$ and ${}^8\text{He}$	118
4.4.2	No-Core Shell Model results for ${}^6\text{He}$ and ${}^8\text{He}$	122
4.4.3	Hyperspherical harmonics expansion results for ${}^6\text{He}$ and coupled cluster theory results for ${}^8\text{He}$	123
4.4.4	Summary	124
5	Summary and outlook	126
	Bibliography	129
 Appendix		
A	Ion beam capture optimization	135

List of tables

1.1	Relative contributions of various sources of errors on the charge radius of $^{6,8}\text{He}$	6
1.2	Main contributions to the AME03 $^{6,8}\text{He}$ masses.	7
1.3	Measured charge radius for $^{6,8}\text{He}$	17
2.1	Possible ISAC contaminants for $^{6,8}\text{He}$	38
2.2	$^6\text{Li}^+$ ion frequencies in TITAN's Penning trap.	51
3.1	Fitting parameters describing the quadratic change in $\bar{\nu}_c$ with the amplitude V_{quad}	69
3.2	Frequency shift due to the various electric potential multipoles.	73
3.3	Calculated correction potentials and corresponding C_4 and C_6 coefficients.	77
3.4	ν_c for symmetric over-converted TOF spectra.	87
3.5	Slope and y-intercept of the linear fits shown in figure 3.14.	87
3.6	Determination of the error due to the incomplete trap compensation.	90
3.7	Error due to the magnetic field fluctuations	91
3.8	ν_c shift due to the interaction of multiple ions in the Penning trap.	94
3.9	$(\Delta R/R)_{ion}$ error due to the interaction of multiple ions in the Penning trap.	94
3.10	$\bar{R}_{meas.}$ and $\bar{R}_{rel.corr.}$ for different $\rho_{-,ini}$	98
3.11	Evaluation of the beam energy from the RFQ.	100
3.12	Steering strength obtained from simulation.	102
3.13	$(\Delta R/R)_{rel.}$ for ^4He , ^6Li , ^6He and ^8He using ^7Li as calibration.	102
3.14	Systematic error budget for the TITAN Penning trap	103
3.15	Frequency ratios for ^6Li versus ^7Li	104
3.16	Error budget of the ^6Li mass measurement.	105
4.1	Measured cyclotron frequency ratios for ^8He using ^6Li as calibration.	108

List of tables

4.2	The ${}^6\text{Li}$ mass as used to determine the mass of ${}^8\text{He}$	108
4.3	$\overline{R}_{meas.}$ for ${}^4\text{He}$, ${}^6\text{Li}$, ${}^6\text{He}$ and ${}^8\text{He}$ using ${}^7\text{Li}$ as calibration. . .	111
4.4	Error budget of the ${}^{6,8}\text{He}$ mass measurements.	112
4.5	Difference between TITAN's and the literature mass excess.	112
4.6	Mean corrected cyclotron frequency ratios \overline{R}_{final} of ${}^{6,8}\text{He}$	113
4.7	TITAN Masses and mass excesses of ${}^{6,8}\text{He}$	113
4.8	Binding and two-neutrons separation energies of ${}^{6,8}\text{He}$	114
4.9	Mass shift $\delta\nu_{MS}^{A,4}$ term for ${}^{6,8}\text{He}$ using AME03 and TITAN masses.	115
4.10	New charge and point-proton radii of ${}^{6,8}\text{He}$ using TITAN masses.	116

List of figures

1.1	Chart of nuclei	2
1.2	Charge and matter radius of He and Li isotopes.	3
1.3	Dependance of the field shift and mass shift with the mass number	6
1.4	Compilation of the lightest halo nuclei.	9
1.5	S_N and S_{2N} of He, Li and Be isotopes.	10
1.6	Borromeo coats of arms	11
1.7	Schematic of a Borromean nuclei	12
1.8	Possible two-neutrons correlations for ${}^6\text{He}$	14
1.9	Schematic of the electromagnetic and nuclear interaction for three bodies.	19
1.10	Examples of 2- and 3-body interactions.	21
1.11	Particle, Jacobi and hyperspherical coordinates systems.	24
1.12	Construction of the coupled cluster single-double (CCSD) correlated wave function using particle excitation.	26
1.13	Tjon-line and three-body potentials	27
1.14	S_{2N} of nuclei in the range $N = 22$ to 45	29
1.15	Q -value difference between [Von77] and the weighted average of all other data.	33
2.1	A schematic view of the ISAC experimental hall.	35
2.2	Schematic of the TITAN experimental setup.	36
2.3	The ISAC production and separation room.	37
2.4	Schematic of TITAN's RFQ.	39
2.5	Block diagram of the TITAN beam line.	41
2.6	Schematic of the Lorentz steerer.	43
2.7	Schematic of TITAN's EBIT.	44
2.8	Schematic view of the hyperbolic structure of a Penning trap.	45
2.9	Penning trap quadrupolar electric potential.	47
2.10	Illustration of TITAN's Penning trap.	48
2.11	Epitrochoid motion of an ion inside a Penning trap.	50

List of figures

2.12	Change in r_{\pm} and E_r with the conversion factor.	54
2.13	Change in E_r with the detuning $\Delta\nu_{RF}$	55
2.14	Axial magnetic field compared with change in E_r	56
2.15	${}^6\text{Li}^+$ cyclotron frequency resonance	57
2.16	Linear interpolation of the calibration ν_c	58
3.1 Harmonic distortion and misalignment of the magnetic field		
	axis	64
3.2	Photo of TITAN's Penning trap.	67
3.3	Ring electrode tilt schematic.	68
3.4	Effect of the harmonic distortion on the measured cyclotron	
	frequency.	70
3.5	Electron gun alignment of the vacuum chamber	71
3.6	Trap misalignment with the magnetic field	72
3.7	Axial potential produced by the Penning trap electrodes.	75
3.8	Residual of a quadratic fit of a realist Penning trap potential.	77
3.9	Linear variation in C_4 and C_6 coefficients with the correction	
	potential.	78
3.10	Axial oscillations versus capture timing.	80
3.11	Shift in the reduced cyclotron frequency with the capture	
	timing.	81
3.12	Shift in the reduced cyclotron frequency with the capture	
	timing for various k_{tube}	82
3.13	Change in the reduced cyclotron frequency shift with k_{tube}	83
3.14	Optimal k_{guard} and k_{tube}	84
3.15	Radial energy gain E_r for non-zero C_4	85
3.16	Variation of the frequency shift with C_4 and η	86
3.17	Change in the fitted cyclotron frequency with k_{tube}	88
3.18	ν_c as a function of η for different correction potential.	89
3.19	Temporal variation of the ${}^7\text{Li}$ cyclotron frequency.	91
3.20	Typical count rate analysis for one ${}^6\text{Li}$ spectrum.	93
3.21	Decrease in ν_c for ${}^6\text{Li}$ and ${}^7\text{Li}$ due to the relativistic correction.	97
3.22	$\bar{R}_{meas.}$ and $\bar{R}_{rel.corr.}$ for different ion velocities.	99
3.23	Beam energy as a function of the optimal bending voltage.	101
3.24	TITAN's ${}^6\text{Li}$ M.E. compared to previous measurements.	106
4.1 ${}^{6,8}\text{He}$ time-of-flight resonance spectra.		
		109
4.2	${}^{6,8}\text{He}$ frequency ratio measurements R	110
4.3	${}^{6,8}\text{He}$ binding energies from ab-initio methods compared to	
	TITAN.	117

List of figures

4.4	$^{6,8}\text{He}$ two-neutrons separation energies from ab-initio methods compared to TITAN.	119
4.5	$^{6,8}\text{He}$ point-proton radius from ab-initio methods compared to TITAN.	120
4.6	GFMC point-proton radii for $^{6,8}\text{He}$	121
A.1	^7Li TOF spectra for improper capture timing.	136
A.2	Axial oscillations amplitude variations.	137
A.3	Injection optimization of ^6Li	137
A.4	Variation of the mean TOF versus the extraction time	138

Acknowledgements

This thesis would not have been possible without the dedicated support of many people. First, I would like to express my gratitude to my supervisor Jens Dilling for his continuous support and guidance. I also want to thank Paul Delheij and Mathew Pearson for their assistance. Je voudrais aussi remercier Dave Lunney et George Audi pour mousser mon intérêt pour les mesures de masses.

I was very fortunate to learn from and work with the post-docs Vladimir Ryjkov, Ryan Ringle, Ernesto Mané et Alain Lapierre. They were always offered a great assistance in the laboratory. Their enthusiasm and willingness to share their knowledge was inspiring. I also want to express my thanks for the excellent technical support from Mel Good. We owe him a lot for the success of the experiment.

I greatly appreciated the support of the other students: Mathew Smith, Thomas Brunner, Christian Champagne, Stephan Ettenaer, Aaron Gallant and Vanessa Simon, as well as the various undergraduates students who offered valuable help.

I am very grateful to Sonia Bacca from whom I've learned a lot on nuclear theory as well as Gordon Drake that calculated the new mass shift values for $^{6,8}\text{He}$ using our masses. I want to acknowledge Jens, Ryan, Alain, Sonia, Aaron as well as my wife Tiffany for their patience in proofreading and reviewing the thesis. Their invaluable comments were greatly appreciated.

Je voudrais remercier mes parents pour leurs encouragements ainsi que mon frère Cédric pour me tenir au courant des déboire du tricolore. Finally, I want to thank my wife Tiffany who always stood by and encouraged me.

Chapter 1

Introduction

Nuclear physics is the field of physics that studies the structure, interactions and properties of atomic nuclei as well as the laws governing the forces between their constituents. Each nucleus is made of at least one of the two constituents: the proton and the neutron. The nucleus can be characterized according to several parameters including its radius, density and binding energy. Nuclei are described by two types of radii: the matter radius and charge radius. The first is a measure of the extent of both the neutron and the proton distributions in the nucleus, while the second is a measure the extent of the proton distribution only. It is generally observed that both radii are equal within 0.1 fm [Kra88]. Other common feature of nuclei is the near-constant radial density, $\rho(r)$, of the nucleons within the nucleus:

$$\rho(r) \approx \frac{A}{\frac{4\pi}{3}R^3} = \text{constant} \quad (1.1)$$

where $R = \langle r_m^2 \rangle^{1/2}$ is the rms (root-mean-square) matter radius (in the following all radii are understood as rms-radii) and A is the total number of proton and neutrons in the nucleus, also known as the mass number. This near-constant number of nucleons per volume results in a cube root dependance of the matter radius with the mass number:

$$\langle r_m^2 \rangle^{1/2} \propto A^{1/3}. \quad (1.2)$$

Lastly, nuclei are characterized by their binding energy. This quantity is the energy necessary to disassemble the nucleus into individual protons and neutrons. The binding energy defines the boundaries of the nuclear landscape, named driplines. These driplines are where an additional neutron or proton can no longer be confined within the nucleus due to lack of binding energy. Driplines exists on both side of the chart of nuclei (see figure 1.1). When approaching, for example, the neutron dripline, each additional neutron decreases the energy necessary to separate one neutron from the nucleus. Eventually, this separation energy becomes less than zero, and at this point the additional neutron is not bound to the nucleus. For small positive separation energy (less than 1 MeV) compared to the average 8 MeV,

1.1. Nuclear halos

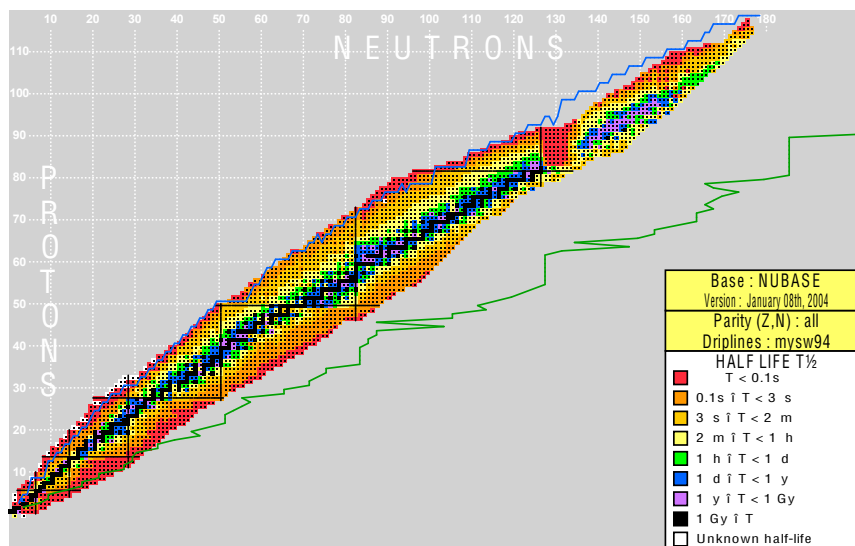


Figure 1.1: Chart of nuclei showing all known nuclei. The nuclei are coloured according to their half-life. The green line indicates the predicted position of the neutron dripline and the blue line the proton dripline according to one of several existing mass model (labeled “mys94” [Mye96]). Figure created by Nucleus-AMDC.

an interesting phenomenon occurs. The combination of the low neutron separation and the short range of the nuclear force results in their quantum mechanical leakage forming an extended halo structure. These type of nuclei are called nuclear halos and they are very specific and atypical.

1.1 Nuclear halos

The first experimental evidence for the existence of halo nuclei came from interaction cross section measurements of helium and lithium isotopes carried out by Tanihata et al. [Tan85a, Tan85b, Tan88]. Using Glauber-model analysis [Gla58], they extracted the matter radii values (presented in figure 1.2) and discovered an abrupt increase in matter radius for ^{11}Li that went beyond the normal $A^{1/3}$ dependence. Comparatively, the matter radius of ^{11}Li is larger by 5 standard deviations when compared to ^{12}C , making it a significant increase. Furthermore, equation (1.2) predicts that the rms matter radius of a nucleus should be independent of the neutron-to-proton

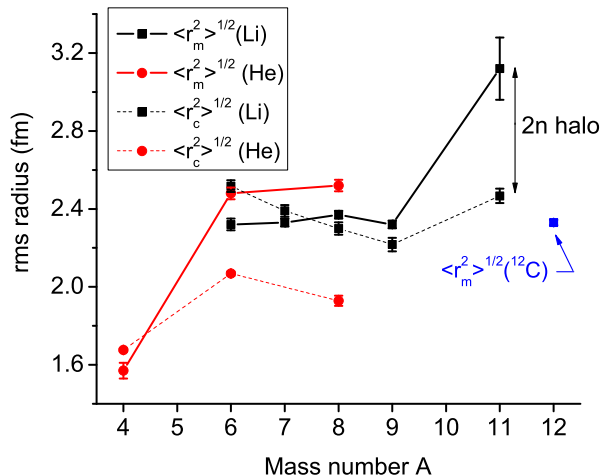


Figure 1.2: The solid lines connects the matter $\langle r_m^2 \rangle^{1/2}$ radius of the helium and lithium isotopes [Tan88] and the dashed lines connects the charge radius $\langle r_c^2 \rangle^{1/2}$ of helium [Mue07] and lithium [San06]. The matter radius of ^{12}C [Oza01] is shown for comparison. Note that the large difference between charge and matter radius for ^6He , ^8He and ^{11}Li , illustrates the characteristic of a halo structure.

ratio for given a mass number (hence isobar-independent). However, for two cases with equal number of nucleons: ^6He - ^6Li and ^8He - ^8Li different radii are found.

For most nuclei the charge and matter radius are equal within 0.1 fm, however for the three peculiar cases: ^6He , ^8He and ^{11}Li , larger differences are found as shown by figure 1.2. In the case of ^{11}Li , for instance, while the matter radius increases by 0.8(2) fm, the charge radius only increase by 0.25(5) fm compared to ^9Li . The increase in charge radius indicates that the added two neutrons have some effect on the proton distribution. However, the comparatively larger increase in matter radius indicates that the neutron distribution is more affected by the added neutrons. This leads to a representation of ^{11}Li as formed of a ^9Li core surrounded by two loosely bound neutrons.

In their landmark study, P.G. Hansen and B. Jonson [Han87] proposed a simple model to explain the non-typical increase (or enlargement) in the

1.1. Nuclear halos

matter radii for certain isotopes. In their model ^{11}Li is described as system composed of a ^9Li core and a di-neutron. The finite-range nuclear potential of the system is approximated to be a three-dimensional square well of radius R and can be approximated as being the size of the ^9Li core. Outside the potential well, the wavefunction is given by spherical Hankel functions and for relative angular momentum $l = 0$ between the core and the di-neutron, the wave function has the form

$$\psi(\vec{r}) = (2\pi\rho)^{-1/2} \frac{e^{-r/\rho}}{r} \frac{e^{R/\rho}}{(1 + R/\rho)^{1/2}} \quad (1.3)$$

where r is the distance between the core centre and di-neutron mid-separation and

$$\rho = \hbar/(2\mu S_{2N})^{1/2}, \quad (1.4)$$

is the decay length of the wave function. The decay length depends on the two-neutron separation energy S_{2N} and the reduced mass μ , defined as

$$\mu = \frac{m(^9\text{Li}) \cdot 2m_n}{m(^9\text{Li}) + 2m_n} \quad (1.5)$$

where $m(^9\text{Li})$ is the atomic mass of ^9Li and m_n is the neutron mass. The two-neutrons separation energy is the energy necessary to remove two neutrons from a nucleus, and is given by:

$$S_{2N}(Z, N) = m(Z, N - 2) + 2m_n - m(Z, N) \quad (1.6)$$

where $m(Z, N)$ is the atomic mass for a nucleus with Z protons and N neutrons and m_n is the neutron mass. For this expression, we assume the speed of light $c = 1$. From equation (1.3), the two-neutron separation energy determines how much the two-neutron wave function extends out of the nuclear potential and, consequently, the size of the matter radius. Therefore, within the Hansen and Jonson model, the two-neutron separation energy is a key parameter in defining two-neutron halo nuclei.

More generally, the nuclear halo is defined as a nucleus composed of a core surrounded by a diffuse region created by the quantum mechanical leakage of the valence nucleons [Jon04]. There are two kinds of halo nuclei, named according to the type of nucleon that form the halo structure: the neutron and the proton halo. Proton halos are considerably less abundant than neutron-halos. This is due to the stronger Coulomb barrier seen by the weakly bound proton. This barrier attenuates the leakage of the proton wave function outside the potential well. In this thesis we mainly concentrate on

the more predominant neutron halo. From this point, we refer to neutron halo nuclei as simply halo nuclei.

There are two quantities needed to identify halo nuclei: the size of the core and the size of the diffuse halo structure outside the core. Being quantum mechanical objects, it is not possible to define a “total” radius for the core and the halo structure. However, it is possible to distinguish the size of the valence neutrons distribution from the core. The size of the core is given by the extent of the proton distribution, namely the charge radius and the extent of the valence neutron wave function which is given by the matter radius. Thus, in order to qualify as halo nuclei there needs to be a significant difference between their charge and matter radii. Figure 1.2 shows that two nuclei qualify as halo nuclei along the helium isotopic chains: ${}^6\text{He}$ and ${}^8\text{He}$. This thesis reports a new determination of the binding energy and subsequent reevaluation of the charge radius of ${}^6\text{He}$ and ${}^8\text{He}$ based on the mass measurement of these nuclei. In the following we outline the motivations for measuring their masses.

1.1.1 Motivations for the mass measurement of ${}^6\text{He}$ and ${}^8\text{He}$

We showed in the previous section that a halo structure can be identified from a large difference between charge and matter radii. The charge radius of halo nuclei also gives valuable insight into the correlations between the neutrons forming the halo, as we show in section 1.1.2.3.

The charge radius of ${}^6\text{He}$ and ${}^8\text{He}$ have been recently determined using isotopic shift measurements: ${}^6\text{He}$ at the Argonne National Laboratory [Wan04] and ${}^8\text{He}$ at the GANIL facility [Mue07]. In this method a transition frequency is measured for two isotopes of the same element. The increase in number of neutrons in the nucleus causes a change in the transition frequency called isotopic shift. This shift has two components: the mass shift and the field shift. The former include the effects on the energy level arising from the change in reduced mass of the electron and is inversely proportional to the nuclear mass. The field shift is caused by the change in volume and hence effective electric fields of the nucleus and is proportional to the change in charge radius. For light nuclei, the mass shift is considerably larger than the field shift. For instance, the mass shift of ${}^8\text{He}$ is 72 000 times larger than its field shift. This large difference is explained by both the larger fractional change in the mass for light nuclei and the smaller volume of light nuclei. The strength of the two components of the isotopic shift as a function of the atomic number Z are shown in figure 1.3.

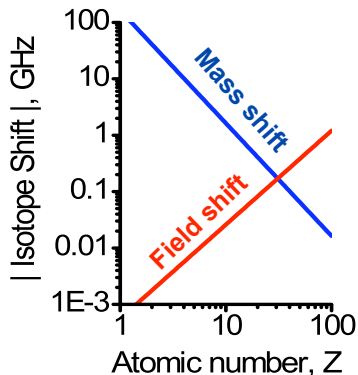


Figure 1.3: Dependence of the field shift and mass shift on mass number.

Error	${}^6\text{He}$ (%)	${}^8\text{He}$ (%)
Statistical	6	18
Atomic mass	19	58
Other systematics	75	24

Table 1.1: Relative contributions, in percent, of various sources of errors on the charge radius of ${}^6,8\text{He}$ coming from the isotopic shift measurement [Mue07]. Note that the error from the atomic mass of ${}^8\text{He}$ accounts for over half of the total error, while it is almost 20% for ${}^6\text{He}$.

The comparatively large size of the mass shift term compared to the field shift term requires that in order for both terms to be known to a similar absolute precision, the mass shift term must be known to a considerably larger relative precision. Since the mass shift term is inversely proportional to the atomic mass and the field shift term is proportional to the charge radius, in order to have a reliable charge radius a precise mass determination is important. In the case of ${}^8\text{He}$, the atomic mass value is, in fact, the dominant source of systematic uncertainty on the charge radius. Table 1.1 shows that the atomic mass constitutes 58% of the uncertainty on the results of the isotopic shift measurement of ${}^8\text{He}$ and 19% for the case of ${}^6\text{He}$ [Mue07].

In order to minimize the contribution of the atomic mass to the charge radius uncertainty, we estimate that the mass excesses of ${}^6\text{He}$ and ${}^8\text{He}$ need to be known at levels of 350 eV and 730 eV, respectively. Mass excess is generally referred to as the difference between the atomic mass and the mass

1.1. Nuclear halos

Isotope	Ref.	M.E. (keV)
${}^6\text{He}$	[Aud03]	$17\,595.11 \pm 0.76$
${}^8\text{He}$	[Aud03]	$31\,598.0 \pm 6.9$
${}^8\text{He}$	[Tri77]	$31\,593 \pm 8$
${}^8\text{He}$	[Kou75]	$31\,613 \pm 17$

Table 1.2: ${}^6\text{He}$ and ${}^8\text{He}$ mass excesses from the AME03 and the major contributions to the AME03 ${}^8\text{He}$ mass evaluation.

number, which is expressed in units of keV. However, table 1.2 shows that the mass excesses of ${}^6\text{He}$ and ${}^8\text{He}$ from the 2003 Atomic Mass Evaluation (AME2003) [Aud03] are 760 eV and 6.9 keV respectively. This means that, in the case of ${}^8\text{He}$, an improvement in the precision of almost a factor of ten is needed to offset the impact of the mass uncertainty whereas an improvement of a factor of two is necessary for ${}^6\text{He}$.

In addition to improving the precision level, there is a need to verify the accuracy of the mass values for ${}^6\text{He}$ and ${}^8\text{He}$. The precision is a measure of the reproducibility of the measurement, while the accuracy measure its correctness. The best way to confirm the accuracy of a measurement is to have an independent verification of this measurement at a similar or better level of precision. Table 1.2 shows the two major contributions ([Kou75] and [Tri77]) to the mass evaluation of ${}^8\text{He}$. These two results differ by 20 ± 19 keV, which means that the value of the charge radius of ${}^8\text{He}$ is uncertain by as much as 40%. Therefore, precise and accurate mass values for the halo nuclei ${}^6\text{He}$ and ${}^8\text{He}$ are important to increase the reliability of the charge radius value.

With a precise and accurate knowledge of the charge radius and binding energies of the ${}^6\text{He}$ and ${}^8\text{He}$ halos, one can test the validity of the current nuclear theories all of which attempt to explain the complex interactions within the nucleus. For example, ab-initio (from first principle) methods are one of the more sophisticated approaches to investigating the nuclear system. These methods use nucleons as the building block and the Schrödinger equation to compute the nuclear properties (see section 1.3 for more details). However, the complexity of the calculation increases rapidly with the number of nuclei and it is currently limited to systems with mass number $A \lesssim 10$. Within this mass range, there are two systems that offer unique opportunity to test these ab-initio methods, the neutron halo nuclei ${}^6\text{He}$ and ${}^8\text{He}$. Explaining the extreme properties of halo nuclei such as their very low

valence neutron separation energy, large matter radius and large difference between charge and matter radius poses a challenge to the ab-initio methods. For example, for some methods [Pie07], the calculation of the charge radius is particularly sensitive to the neutron separation energy. The small neutron separation energy of halo nuclei is close enough to zero to cause the nuclei to “break apart” if the initial parameters of the calculations are not set properly. Therefore, explaining both the binding energy and charge radius of ${}^6\text{He}$ and ${}^8\text{He}$ is challenging for ab-initio methods.

In order to compare the predictions of ab-initio methods with the measured binding energies and charge radius, one needs to have precise and accurate values for both quantities. However, the current uncertainty on the charge radius of ${}^6\text{He}$ and ${}^8\text{He}$ is in the same range as the theoretical values. The atomic mass being an important contributor to the uncertainty of the charge radius, a precise and accurate mass measurement of these nuclei is critical for having a reliable test of the ab-initio method predictions. In order to remove the atomic mass as being an important contributor to the uncertainty of ${}^6\text{He}$ and ${}^8\text{He}$ charge radius, their masses needs to be known to the 10^{-7} level.

Currently, the only type of spectrometer that can achieve such level of precision and accuracy are Penning traps. Therefore, we conducted a mass measurement of ${}^6\text{He}$ and ${}^8\text{He}$ using the TRIUMF Ion Trap for Atomic and Nuclear science (TITAN) Penning trap. Extensive systematic studies of the TITAN Penning trap have been performed (see chapter 2) with the purpose of reaching the precision and accuracy needed for the ${}^6\text{He}$ and ${}^8\text{He}$ mass measurement. As a result of these studies, we also performed a mass measurement on ${}^6\text{Li}$, in order to resolve an existing 1.6×10^{-8} disagreement between two previous Penning mass measurements [Hea01, Nag06]. This also represents a milestone regarding the level of precision the experiment can presently achieve.

1.1.2 The different types of halo nuclei and characteristics of ${}^6\text{He}$ and ${}^8\text{He}$

Halo nuclei are classified as proton and neutron halos. Proton-halo are considerably less abundant than the neutron-halos because of the stronger Coulomb barrier experienced by the weakly bound protons. To date, only ${}^8\text{B}$ [Min92] has been identified as a one proton-halo.

Comparatively, the weakly bound neutrons are not affected by the coulomb barrier and thus more neutron-halos have been identified, such as ${}^6\text{He}$, ${}^8\text{He}$, ${}^{11}\text{Li}$, ${}^{11}\text{Be}$ and ${}^{14}\text{Be}$ (figure 1.4). Generally, there are three types of neutron

1.1. Nuclear halos

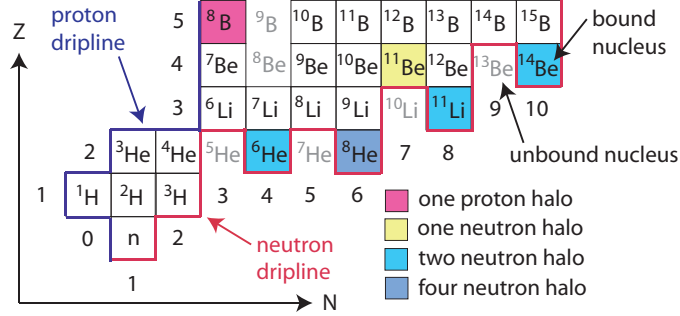


Figure 1.4: Section of the chart of nuclides, showing the lightest halo nuclei: the one proton halo ${}^8\text{B}$, the one neutron ${}^{11}\text{Be}$, the two-neutrons ${}^6\text{He}$, ${}^{11}\text{Li}$ and ${}^{14}\text{Be}$ and the four neutron halo ${}^8\text{He}$ labeled by colour code. Also shown are the neutron and proton driplines.

halos: one neutron halo such as ${}^{11}\text{Be}$, two neutron halos such as ${}^6\text{He}$, ${}^{11}\text{Li}$ and ${}^{14}\text{Be}$ and four neutron halo such as ${}^8\text{He}$ (see figure 1.4). Not all halo nuclei are listed in the chart in figure 1.4, for instance, the one-neutron halo ${}^{19}\text{C}$ [Baz95] and the two-neutron halo ${}^{22}\text{C}$ [Tan10]. In addition, the halo nature of some nuclei such as ${}^{15}\text{C}$, ${}^{17}\text{C}$ and ${}^{14}\text{B}$ [Baz98], not shown in the graph, are still under debate. Furthermore, more halo nuclei are expected to be found as the production of heavier dripline nuclei in larger quantities will become possible.

1.1.2.1 Neutron separation energies

The identified neutron halos share the common feature of being located along the neutron dripline (see figure 1.4). The proton and neutron driplines set the boundary between bound and unbound systems. A nucleus is bound when energy is required to remove one or two nucleons. This means that the one-neutron separation energy, defined as

$$S_N(Z, N) = m(Z, N - 1) + m_n - m(Z, N) \quad (1.7)$$

as well as the two-neutrons separation energy (see equation (1.6)) of the nuclei needs to be positive for the nucleus to be bound. The type of halo to be formed is strongly influenced by the values of the one- and two-neutron separation energies.

To illustrate this principle, we looked at the one- and two-neutron separation energies for helium, lithium and beryllium isotopes (figure 1.5) and

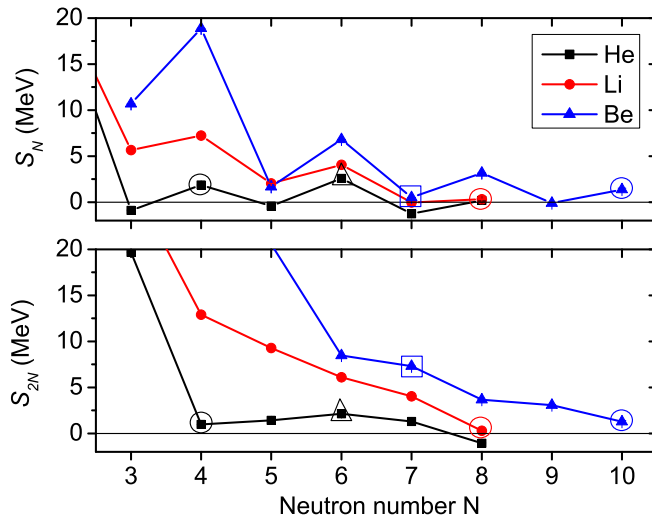


Figure 1.5: One- and two-neutron separation energies S_N (top) and S_{2N} (bottom), as a function of neutron number for helium, lithium and beryllium isotopes. One-neutron halo is squared, two-neutron halos circled and four-neutron halo triangled. The error bars are not visible at this scale.

the effects of nucleon pairing. Nucleon pairing is the phenomenon where nucleons of the same type tend to pair up to form a more stable structure. This results in the even-neutron, even-proton number nucleus to form a more energetically favorable configuration than when one or both number of nucleon are odd. As a result, for a given number of protons, the nucleus with an even number of neutrons are more tightly bound and present a larger one-neutron separation energy than its odd neutron number counterpart.

Figure 1.5 shows the staggering pattern in the one-neutron separation energy among the three series of isotopes which is caused by nucleon pairing. We now show how this staggering explains the different types of halo structures. Taking ${}^4\text{He}$ as an example, the addition one neutron to ${}^4\text{He}$ reduces the one-neutron separation energy to below zero, which means that the added neutron is readily expelled and thus ${}^5\text{He}$ is non-existing. However, when adding an additional neutron to ${}^5\text{He}$, the one-neutron separation energy rises slightly above zero. This means the valence neutron pair forms a

1.1. Nuclear halos

weak and stable bond with the ${}^4\text{He}$ core. The weakness of that neutron pair is evidenced by the small (below 1 MeV) two-neutron separation energy of ${}^6\text{He}$, as shown in the bottom half of figure 1.5. Therefore, a two-neutron ${}^6\text{He}$ halo is formed. Similarly, when adding one extra neutron to ${}^6\text{He}$, the one-neutron separation energy again falls below zero, and yet it returns to above zero after adding an additional neutron. Hence, this new valence neutron pair forms a weak and stable bond with the ${}^6\text{He}$ structure. A four-neutron ${}^8\text{He}$ halo is then formed (See later section 1.2.1 for more elaborate account). Regarding the formation of one-neutron halos, the same principle applies. For example, ${}^{10}\text{Be}$ has six neutrons. Adding one neutron reduces the one-neutron separation energy but not below zero. Therefore, the new neutron forms a weak, stable bond with the ${}^{10}\text{Be}$ core. The one-neutron halo ${}^{11}\text{Be}$ is thus formed. It is noteworthy to note that all neutron halos occur in nuclei close to the neutron dripline where the valence binding energy approaches zero.

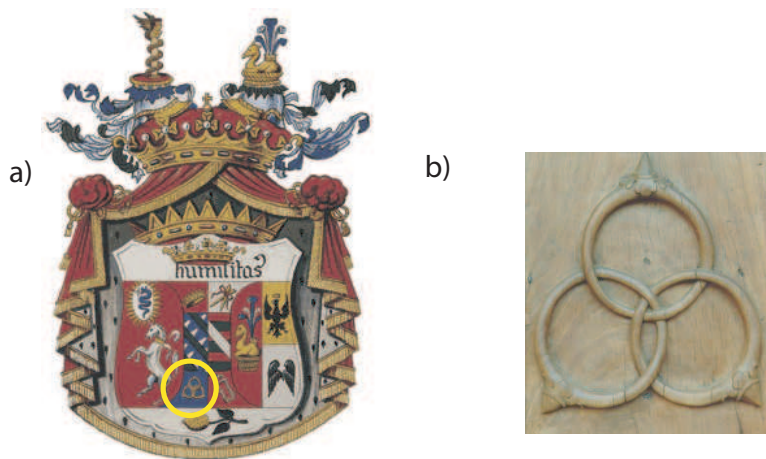


Figure 1.6: a) The Borromeo family coats of arms figuring the famous borromeoan rings (circled). b) Borromeo rings carved on the door of the Church of San Sigismondo in Cremona.

Borromeoan halos are a special type of two-neutron halo nuclei. Examples are the two-neutron halos ${}^6\text{He}$, ${}^{11}\text{Li}$ and ${}^{14}\text{Be}$. Borromeoan halos are named after the aristocratic Borromeo family who used a special ring configuration on their coat of arms (see figure 1.6). These three rings are interlocked in such a way that if one ring is removed, it disentangles the other two. Figure 1.7 illustrates the case for ${}^6\text{He}$. Both the ${}^4\text{He} + n$ system (${}^5\text{He}$) and

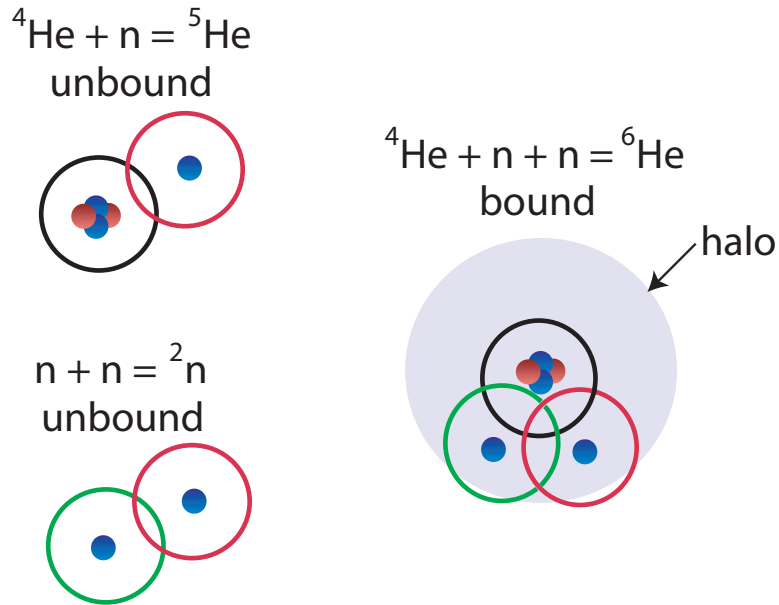


Figure 1.7: Comparative illustration of the borromean nucleus ${}^6\text{He}$ and the borromean rings. The Borromean rings shown around the different compounds, indicate that when one of the constituent of the borromean nuclei is missing, the system is unlocked.

the two-neutron system (2n) are unbound, while the ${}^4\text{He} + n + n$ system (${}^6\text{He}$) is bound.

1.1.2.2 Cross section comparison

Evidence for the two-neutron halo structure in ${}^6\text{He}$ is based on the comparison of the interaction cross section, σ_I , of ${}^4\text{He}$ and ${}^6\text{He}$ with the two-neutron removal cross section, σ_{-2n} , of ${}^6\text{He}$. The interaction cross section is the total cross section for process of proton and neutron removal. This cross section was measured using transmission-type experiment where a 790 MeV/nucleon beam of ${}^{6,8}\text{He}$ impinge a ${}^{12}\text{C}$ target. The nuclei that are transmitted through the target then goes into a dipole magnet where they are identified according to their bending angle. In order to determine the interaction cross-section, the number of incoming nuclei is measured before the target and the number of transmitted nuclei from the same isotope is also counted after the dipole magnet. The total interaction cross section between the beam and

the target material is then calculated using:

$$\sigma_I = \frac{1}{N_t} \ln \left(\frac{\gamma_0}{\gamma} \right) \quad (1.8)$$

where γ is the number of non-interacting ${}^{6,8}\text{He}$ transmitted over the number of incoming ${}^{6,8}\text{He}$, γ_0 is the same ratio but without the target in place and N_t is the number of target nuclei per cm^2 . The two-neutron removal cross section of the isotope ${}^A\text{He}$ is simply the production cross section of the isotope ${}^{A-2}\text{He}$ from the interaction of ${}^A\text{He}$ with the target material.

Based on the small two-neutron separation energy of ${}^6\text{He}$, we can assume that ${}^6\text{He}$ is composed of a ${}^4\text{He}$ core surrounded by two neutrons. If one assumes that the ${}^4\text{He}$ core is not modified from the free ${}^4\text{He}$, Ogawa, Yabana and Suzuki [Oga92] showed using a Glauber model analysis that the cross section for the removal of two neutrons from ${}^6\text{He}$ is equal to the difference in interaction cross section of ${}^4\text{He}$ and ${}^6\text{He}$:

$$\sigma_{-2n}({}^6\text{He}) = \sigma_I({}^6\text{He}) - \sigma_I({}^4\text{He}). \quad (1.9)$$

Using the measured values for these cross sections using 790 MeV/nucleon beam on a ${}^{12}\text{C}$ target [Tan92], we get

$$\sigma_{-2n}({}^6\text{He}) = 189 \pm 14 \text{ mb} \quad (1.10)$$

$$\sigma_I({}^6\text{He}) - \sigma_I({}^4\text{He}) = 219 \pm 8 \text{ mb}, \quad (1.11)$$

which agrees within two standard deviations. This verifies that ${}^6\text{He}$ is composed of a ${}^4\text{He}$ core and two loosely bound neutrons.

To test whether ${}^8\text{He}$ is comprised of a ${}^6\text{He}$ core surrounded by two neutrons or of a ${}^4\text{He}$ core plus four neutrons, we apply the same cross section comparison. Firstly, we examine the ${}^6\text{He}$ plus two neutron possibility by comparing the measured two neutron removal cross section of ${}^8\text{He}$ with the interaction cross section of ${}^6\text{He}$ (again for 790 MeV/nucleon beam on a ${}^{12}\text{C}$ target [Tan92]):

$$\sigma_{-2n}({}^8\text{He}) = 202 \pm 17 \text{ mb} \quad (1.12)$$

$$\sigma_I({}^8\text{He}) - \sigma_I({}^6\text{He}) = 95 \pm 9 \text{ mb}. \quad (1.13)$$

This yields an inconsistent value and therefore ${}^8\text{He}$ cannot be interpreted as a ${}^6\text{He}$ core plus two neutrons.

Secondly, we examine the possibility of a ${}^4\text{He}$ plus four neutron system. We assume that ${}^8\text{He}$ is formed of an unperturbed ${}^4\text{He}$ core surrounded by

four neutrons. Modifying equation (1.9) to account for the removal of four neutrons [Tan92], we get:

$$\sigma_{-2n}({}^8\text{He}) + \sigma_{-4n}({}^8\text{He}) = \sigma_I({}^8\text{He}) - \sigma_I({}^4\text{He}). \quad (1.14)$$

Using this expression, we find:

$$\sigma_{-2n}({}^8\text{He}) + \sigma_{-4n}({}^8\text{He}) = 297 \pm 19 \text{ mb} \quad (1.15)$$

$$\sigma_I({}^8\text{He}) - \sigma_I({}^4\text{He}) = 314 \pm 8 \text{ mb}. \quad (1.16)$$

The result is in agreement and it suggests that ${}^8\text{He}$ can be described as a ${}^4\text{He}$ core surrounded by four neutrons.

1.1.2.3 Charge radius of halo nuclei

Halo nuclei are defined as a core surrounded by valence nucleons that tunnel outside the core. In Figure 1.2 we observe that in a neutron-halo, the difference between the extension of the proton wave function and the neutron wave function is observed as a difference in charge and matter radii. A determination of both quantities is important to characterize a neutron halo.

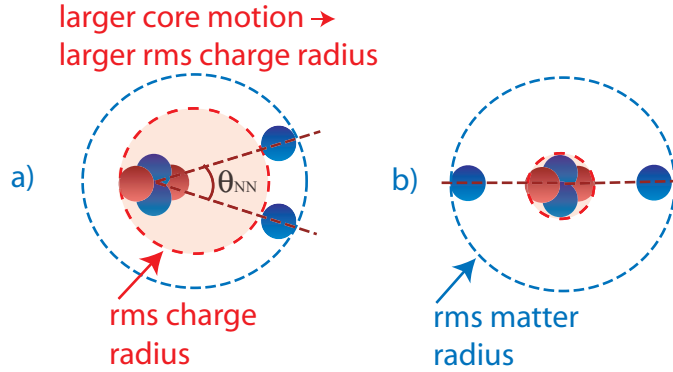


Figure 1.8: Classical representation of a ${}^6\text{He}$ nucleus comprising a ${}^4\text{He}$ core and two neutrons. The movement around the centre of mass depends on the relative position of the valence neutrons in the halo structure. a) larger movement induced by neutrons being predominantly on one side of the core b) smaller movement caused by neutrons predominately on the opposite side of the core. See text for more explanations.

In addition, the charge radius provides valuable information on the size of the halo structure as well as the relative positions and motion of the valence neutron. In figure 1.8, we illustrate that for a given matter radius the ${}^6\text{He}$ halo has a larger charge radius if the two valence neutrons predominately reside on one side of the ${}^4\text{He}$ core. However, if the two valence neutrons reside mainly on the opposite ends of the core, the charge radius of ${}^6\text{He}$ becomes much smaller.

With the knowledge of charge radius, one can determine the average classical angle θ_{NN} between the two valence neutrons (figure 1.8(a)) using the charge radius. C.A. Bertulani and M.S. Hussein [Ber07] have determined the opening angle of the two valence neutrons of ${}^6\text{He}$ using the charge radius from [Wan04]. They calculated an angle of $\theta_{NN} = 78_{-18}^{+13}$. This means that the two neutrons are, in a classical picture, located on the same side of the core. Similarly as for ${}^6\text{He}$, a change in the charge radius of ${}^8\text{He}$ compared to ${}^4\text{He}$ would be a consequence of the correlation between the neutrons forming the halo. Then within this classical approach, comparing the charge radius of ${}^8\text{He}$ with ${}^6\text{He}$ would reveal whether the distribution of the four neutron is more symmetric around the core or if the neutrons are more paired.

1.1.2.4 ${}^6\text{He}$ and ${}^8\text{He}$ charge radius measurements

The ${}^6\text{He}$ and ${}^8\text{He}$ charge radii were determined [Wan04, Mue07] using isotopic shift measurements. This is a method that measures the variations in atomic energy levels due to changes within the nucleus. These are changes in the fine and hyperfine splitting of the atomic energy levels.

In this method, the frequency of a given atomic transition is measured for two different isotopes. Then, the isotopic shift $\delta\nu^{A,A'}$, which is the difference between the frequencies ($\nu^{A'}$, ν^A) of transitions of isotope A and A' of the same element [Ott87]:

$$\delta\nu^{A,A'} = \nu^A - \nu^{A'} = \delta\nu_{MS}^{A,A'} + \delta\nu_{FS}^{A,A'} \quad (1.17)$$

is calculated. The right-hand side of equation (1.17) shows that the isotopic shift is composed of two components; a mass shift $\delta\nu_{MS}^{A,A'}$ and a field shift $\delta\nu_{FS}^{A,A'}$.

The mass shift is given as [Ott87]:

$$\delta\nu_{MS}^{A,A'} = (K_{NMS} + K_{SMS}) \frac{M_A - M_{A'}}{M_A M_{A'}}, \quad (1.18)$$

where K_{NMS} is the normal mass shift coefficient and K_{SMS} is the specific mass shift coefficient. K_{NMS} takes into account the recoil of the nucleus

due to the motion of the electrons and K_{SMS} represent the influence of the electron motion correlation on the motion of the nucleus. The mass shift is produced by a change in the reduced mass of the electron $\mu_e = m_e M_A / (m_e + M_A)$ for the different isotopes. This different reduced mass then results in a different binding energy for the electron. The mass shift is dominant for light nuclei as the relative change in nuclear mass with the number of neutrons is larger than for heavier nuclei.

The field shift is produced by a change in the charge density distribution in the nucleus due to the different number of neutrons. The field shift is given as

$$\delta\nu_{FS}^{A,A'} = K_{FS} \cdot \delta\langle r_c^2 \rangle^{A,A'}, \quad (1.19)$$

where K_{FS} is the electronic field shift constant. This constant depends on the nuclear charge and reflects the change in the electron charge density between the two transition states. $\delta\langle r_c^2 \rangle^{A,A'}$ is the difference in mean square charge radius between isotope A and A' .

As the isotopic shift method allows one to extract the difference in charge radius $\delta\langle r_c^2 \rangle^{A,A'}$, one needs a reference isotope with which the absolute charge radii can be obtained. It is often possible to use as a reference the mean-square charge radius of a stable isotope $\langle r_c^2 \rangle^{A'}$. For the ${}^6,8\text{He}$ charge radius determination, the charge radius of ${}^4\text{He}$, obtained from electron scattering was used. One can calculate the mean-square charge radius of the isotope of interest using:

$$\langle r_c^2 \rangle^A = \langle r_c^2 \rangle^{A'} + \frac{\delta\nu^{A,A'} - \delta\nu_{MS}^{A,A'}}{K_{FS}}, \quad (1.20)$$

where $\langle r_c^2 \rangle^{A'}$ is the mean-square charge radius of the stable isotope. The root-mean-square radius is then given as $r_c = \sqrt{\langle r_c^2 \rangle^A}$.

In the case of the helium isotopes, the field constant K_{FS} , as well as the mass shift $\delta\nu_{MS}^{A,A'}$ are precisely calculated quantities from exact solution of the three body (one nucleus, two electrons) Schrödinger equation where relativistic and quantum electrodynamic effects have been treated perturbatively [Dra04].

The first charge radius measurement of a halo nucleus using isotopic shift measurement was ${}^6\text{He}$ performed at the Argonne National Laboratory [Wan04]. The charge radius of ${}^6\text{He}$ has been determined from the measurement of the $2^3S_1 - 3^3P_2$ transition frequency and found to be 2.054(14) fm [Wan04]. The charge radius of ${}^6\text{He}$ was remeasured afterwards, together with ${}^8\text{He}$ at the GANIL facility by the same group and the results [Mue07] are shown in table 1.3. Both ${}^6\text{He}$ charge radius values were consistent.

1.2. Nuclear halo and nuclear models

Isotope	Charge radius (fm)
${}^6\text{He}$	2.068(11)
${}^8\text{He}$	1.929(26)

Table 1.3: Charge radii of ${}^{6,8}\text{He}$ as determined from isotopic shift measurement [Mue07].

1.2 Nuclear halo and nuclear models

One of the central questions in nuclear physics is the understanding of the relevant fundamental forces (electromagnetic, weak and strong) and how they translate into the rich and complex observed phenomena. Over the last century, since the first atomic and nuclear models have been developed, more and more sophisticated approaches have been investigated. Some of the best systems to test these models are halo nuclei.

In order for a model to successfully describe a halo nucleus, it needs to reproduce the experimental properties of halos: very low valence neutron separation energy, large matter radius and large difference between charge and matter radii. These conditions pose a challenge to the various models. However, halo nuclei are typically few nucleon systems and can be tackled with a rigorous approach in theory. Halo nuclei therefore represent good test cases for theory in extreme conditions, refining our understanding of nuclear physics.

There are two classes of models aimed at describing nuclear halos: cluster models and ab-initio methods. Cluster models group the neutrons (n) and protons (p) in sub-structures called clusters. Examples of such clusters include the deuteron ($d = p + n$), the triton ($t = p + 2n$) and the alpha particle ($\alpha = 2p + 2n$). For ${}^{6,8}\text{He}$, there exist a wide variety of cluster models. Some of these models describe ${}^8\text{He}$ as $\alpha + 2n + 2n$ [Yos07, Nes01] structures while others describe ${}^{6,8}\text{He}$ as $\alpha + 2n$ and $4n$ structures [Var94]. As halo nuclei are formed of a core and a valence nucleon substructure, it seems natural to describe them using cluster models. However, cluster models offer a simplified picture of halo nuclei, by freezing parts of the nucleus, they could neglect important effects. Example of such effects for ${}^{6,8}\text{He}$ would include changes in the size of α -particle core compared to the free α -particle due to the interaction between the valence nucleons and the nucleons forming the core.

Ab-initio (from first principle) methods, on the other hand, treat all the

nucleons on the same footing. By considering nucleons as building blocks in nuclei, ab-initio methods are the most fundamental approach to nuclei so far. However, these methods become more computationally intensive as the number of nucleons involved increases. As a result, ab-initio methods are typically limited to light nuclei with $A \lesssim 10$. Among the limited number of systems that ab-initio method can describe, halo nuclei are important because of their extreme properties. The only halos that are described using several ab-initio approaches are ${}^6,8\text{He}$. These approaches includes: the Green Function Monte Carlo (GFMC) [Pie05], the No-Core Shell Model (NCSM) [Cau06], the Coupled Cluster (CC) theory [Hag07a] and the Hyperspherical Harmonics expansion (HH) [Bac09a].

Theoretical predictions for the charge radius of the halo nuclei ${}^6,8\text{He}$ were made using both ab-initio methods and cluster models. A previous study [Wan04] found that several cluster models were under-predicting the ${}^6\text{He}$ charge radius compared to the measured value. On the other hand, the prediction from ab-initio methods were found to be in agreement with the experimental charge radius of ${}^6,8\text{He}$ [Mue07]. As the ab-initio methods seem to provide more accurate predictions for the ${}^6,8\text{He}$ charge radius than the cluster models, in this thesis we will concentrate on the prediction of ab-initio methods. Moreover, being the only halo nuclei with $A \lesssim 10$, ${}^6,8\text{He}$ are a unique test-bench for ab-initio methods. However, being less computationally intensive than ab-initio methods, cluster models can provide useful predictions about experimental observables for system with $A > 10$.

As the study done in [Mue07], we will compare ab-initio method predictions for the charge radius of ${}^6,8\text{He}$ with the new values obtained using the TITAN masses. Moreover, we go a step further than this study and also compare the ab-initio method predictions for the binding energies with the values calculated from the TITAN masses. By testing the ab-initio method predictions for two different observables, one can find where the methods limitations reside and possibly motivate improvement of the methods.

1.2.1 Nuclear potential for ab-initio methods

The interaction among nucleons forming the nucleus is governed by the strong force and the theoretical description of the strong force is Quantum Chromodynamics (QCD). However, QCD cannot be treated perturbatively at the energy scales of the nucleus, which makes it a complex problem to solve. Therefore, ab-initio method's do not use quark and gluons as their basic constituents, but instead use nucleons. By neglecting the quark interaction within the nucleons, the nucleons become the effective degrees of

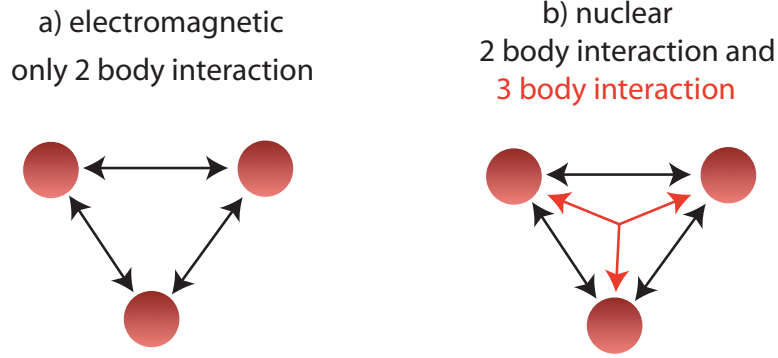


Figure 1.9: Schematic of the interaction of three bodies due to a) the Coulomb potential. b) the nuclear potential. The two-body interactions between pairs of nucleons is symbolized by the black arrow. The three-body interaction between three nucleons is symbolized by the red arrows. The Coulomb potential is only generated from two-body interactions, while the nuclear potential involves both two- and three-body interactions.

freedom of the theory.

To solve the quantum mechanical nuclear many-body problem, ab-initio methods need thus to construct a Hamiltonian and a wave function. Then, using these constructions, one calculates various properties of nuclei by solving the Schrödinger equation

$$H\Psi = E\Psi \quad (1.21)$$

where H is a Hamiltonian that can be of the general form

$$H = T + V = \sum_i \frac{p_i^2}{2m} + \sum_{i<j} V_{ij}^{2N} + \sum_{i<j<k} V_{ijk}^{3N} + \dots \quad (1.22)$$

T is the kinetic energy of the individual nucleons and V_{ij}^{2N} , V_{ijk}^{3N} are two and three-nucleon potentials. Figure 1.9 shows a schematic of the interactions between three bodies for the Coulomb and nuclear potential. Figure 1.9 shows (a) for the Coulomb potential, only two-body interactions are present. However, this is not the case for the nuclear potential. When more than two nucleons are involved, the different nucleons are also affected by three-nucleon interactions (shown by the red arrows in figure 1.9 (b)). Higher order potentials are typically neglected as the potential strength is expected to decrease with the number of nucleons, N , involved [Mac07].

1.2. Nuclear halo and nuclear models

Several modern models describe the strong interaction in terms of meson exchange between structureless nucleons. The concept of meson exchange as mediator of the strong force was first proposed by Yukawa [Yuk34] in the form of the attractive potential

$$V(r) \propto \frac{e^{-m_\pi r}}{r} \quad (1.23)$$

where the pion mass m_π sets the range of the interaction. The interaction range is approximated using the Heisenberg uncertainty principle:

$$\Delta t \Delta E \geq \hbar \quad (1.24)$$

where t is the time over which the meson exist and E is its energy. Using equation (1.24), the range of interaction for the π exchange is estimated to be $\Delta x \approx 1/m_\pi = (140 \text{ MeV})^{-1} = 1.4 \text{ fm}$ (using $c = \hbar = 1$). The modern version of the Yukawa potential is called the one-pion exchange potential. This potential still features the radial exponential decrease, but also includes terms to account for spin and isospin. The isospin is defined as $T = (Z - N)/2$ where Z is the number of protons and N the number of neutrons in the nucleus. Equation (1.22) shows that the nuclear potential is divided mainly into two and three body potentials. In the following, we describe these two types of potentials.

A potential that describes the interaction between two nucleons is called a two-body (2N) potential. We previously showed that the interaction between two nucleons can be described using the one-pion exchange potential (see figure 1.10 (a)). This figure shows the Feynman diagram for the interactions of two nucleons (N) through the exchange of a π . In this diagram, the direction of time in the process is shown by the arrow. The one-pion exchange potential describes the long-range part of the nuclear potential, but it fails to describe shorter ranges. Therefore, the shorter range of the nuclear potential needs to be described with other types of interactions. For intermediate ranges, the two-body potential can be described using higher-order π interactions such as 2π (0.7 fm interaction range) (see figure 1.10 (b)) and 3π (0.5 fm interaction range) exchange. Both intermediate and long range interactions are attractive in order to hold the nucleons forming the nuclei together. However, at short ranges the two nucleon potential becomes repulsive, a consequence of the Pauli exclusion principle between the quarks. As the short range interaction cannot be explained using π -exchanges, it has to be treated with contact terms (see figure 1.10 (c)), which are direct nucleon-nucleon interactions (called contact-interaction) or

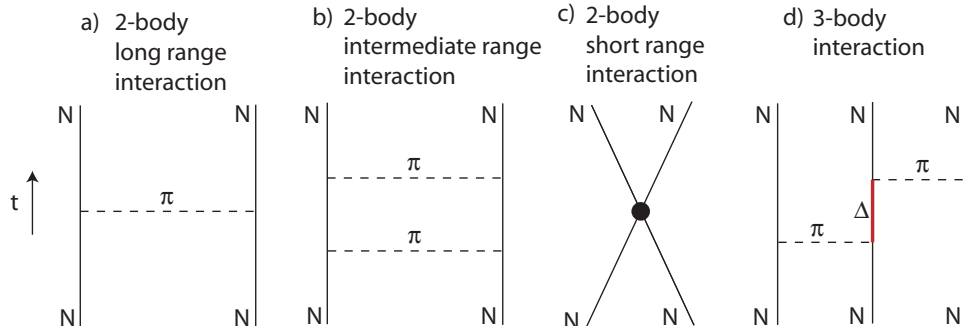


Figure 1.10: Example of two-body interactions Feynman diagrams: a) Long-range one-pion interaction, b) intermediate-range two-pion interaction and c) contact-term short-range two-pion interaction (symbolized by the filled circle). Example of three-body interaction Feynman diagram: d) Two-pion exchange between three nucleons through the first excited state Δ of one of the nucleon. The direction of time t is shown by the arrow. Nucleons are denoted by N .

phenomenologically. Ab-initio interactions typically use a similar long-range one pion exchange potential, while differences reside in their description of intermediate and short range interaction. Since the nuclear potential is not an observable, several two-nucleon potentials have been developed. These include the Argonne v_{18} [Wir95], the Charge-Dependant (CD)-Bonn [Mac01], the V_{lowk} [Bog03] and the JISP16 [Mar09] potentials. All these potentials are used in ab-initio methods to describe the properties of ${}^6,8\text{He}$.

Three-body potentials describe the interaction between three nucleons. The three-body interaction is a consequence of the quark structure of the nucleons. An example of an interaction forming a three-body potential is shown in figure 1.10 (d). This shows that a π is exchanged between two nucleons, one of which gets excited into a Δ (see figure 1.10 (d)) for a short time before releasing a π that mediates the interaction between the second and third nucleon. A Δ is the first excited of the nucleons and it has a mass of 1232 MeV. Three-body potentials are important to accurately describe the binding energy of nuclei with more than two nucleons [Pie01b]. In fact, in order to properly explain the experimental values of light nuclei like ${}^3\text{H}$ and ${}^4\text{He}$, three-nucleon potential are needed, since with two-nucleon potential nuclei are usually underbound [Nog04, Jur09].

However, calculations involving a three-body potential are more com-

plex and require longer computation time. Therefore, very few methods have made calculations using such potentials [Pie01b], [Nav07], [Gaz06], [Hag07a]. Examples of three-body potentials include the Urbana [Pud95], Illinois [Pie01b] and the chiral three-body potentials [Epe02].

1.2.2 The construction of the wave function

Once a suitable potential is found, one needs a method to construct the wave function and solve the Schrödinger equation. There are a number of methods to perform this task and we briefly describe the ones that have calculated the binding energies and radii of ${}^6\text{He}$ and ${}^8\text{He}$. In section 4.4, we compare the results from these calculations with experimental values.

1.2.2.1 Green function Monte Carlo

The Green Function Monte Carlo (GFMC) is an ab-initio method that calculates the nuclear properties by solving the Schrödinger equation (for a detail review, refer to [Pie05]). In order to construct its wave function, the GFMC method uses a trial wave function obtained from Variational Monte Carlo (VMC). This trial wave function is created using the variational approximation which states that the real ground state wave function is the one that gives the lowest energy E_0 :

$$E_{trial} = \frac{\langle \Psi_{trial} | H | \Psi_{trial} \rangle}{\langle \Psi_{trial} | \Psi_{trial} \rangle} \geq E_0 \quad (1.25)$$

where E_{trial} is the ground state energy of the trial wave function. The trial wave function $\Psi_{trial} = \sum_k c_k |k\rangle$ is a sum of states $|k\rangle$ with variable coefficients c_k that are adjusted in order to minimize the energy E_{trial} [Pie01a]. The GFMC method then uses the Ψ_{trial} that minimized the energy E_{trial} to calculate the ground state energy E_0 . The ground state wave function is obtained through the propagation in imaginary time of the wave function under the Hamiltonian:

$$\Psi_0 = \lim_{n\Delta t \rightarrow \infty} \left[e^{-(H-E_0)\Delta t} \right]^n \Psi_{trial} \quad (1.26)$$

where n is the number of iterations of step size Δt . At the limit $n\Delta t \rightarrow \infty$, Ψ_0 is the true ground state of energy E_0 .

The GFMC method performs its calculations using the AV18 [Wir95] two-body potential and the Illinois [Pie01b] as three-body potentials. The AV18 potential is a sum of electromagnetic, one-pion exchange and short

range phenomenological interactions. The Illinois potential [Pie01b] includes a series of two-pions exchange terms as well as short range phenomenological terms. The GFMC method calculates the binding energy of the ground state and low-lying excited states of several nuclei in the range $A = 3$ to 12 with an accuracy of 1-2% compared to the experimental binding energies.

1.2.2.2 No-core shell model

The No-Core Shell Model (NCSM) approach [Nav07], as any ab-initio methods, solve the many-body problem using equation (1.21). The NCSM uses a truncated harmonic oscillator basis, which facilitates the construction of the wave function. Once the wave function is constructed and the potential chosen, the eigenvalues of the Schrödinger equation are obtained by matrix diagonalization which needs in principle an infinite basis. The NCSM solves the problem by dividing the infinite basis space in a model space, where the calculation is performed, and an excluded space. It then derives an effective hamiltonian from the original hamiltonian that is used in the truncated space to accelerate the convergence as a function of the model space size determined by N_{max} (maximal allowed harmonic oscillator excitation above the unperturbed ground state).

One of the features with the NCSM approach is that its wave function present a Gaussian (e^{-r^2}) asymptotic behaviour. We saw from the P.G. Hansen and B. Jonson model [Han87] in equation (1.3), that the halo nuclei wave function decays exponentially. Having an exponential asymptotic behaviour of the wave function is critical to have a correct representation of halo nuclei. The consequence of using a faster Gaussian fall off in a truncated model space is that it truncates terms in the wave function which induces errors in the calculated quantities.

Several different potentials can be used in the NCSM, including chiral effective theory two- and three-body potentials [Nav07]. However, calculation of halo nuclei have been performed with two-body potential like the Inside Non-local Outside Yukawa (INOY) potential [Dol03] and the Charge-Dependant (CD)-Bonn 2000 potential [Mac01]. The INOY potential includes a short range phenomenological two-body potential that mimics three-body interactions. The CD-Bonn 2000 is a two-body meson exchange theory potential.

A recent development of the NCSM method is the No-Core Full Configuration (NCFC) approach [Mar09]. This method is essentially a NCSM calculation where instead of deriving an effective potential in the truncated space, it performs the calculations using the original Hamiltonian and a softer po-

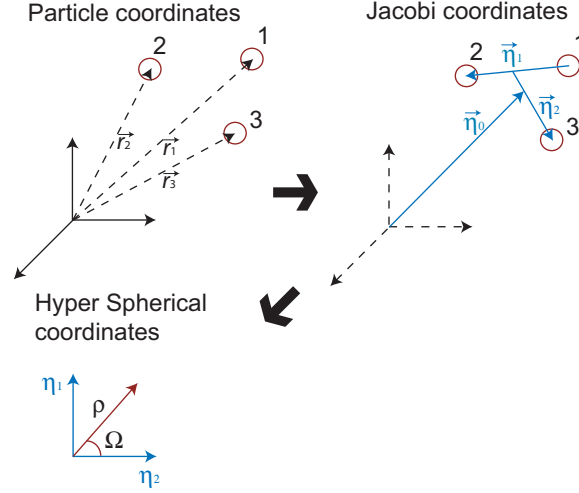


Figure 1.11: Jacobi coordinate system compared to the usual particle coordinate system. Hyperspherical coordinates are based on the $\vec{\eta}_i$ Jacobi coordinate, where the contribution of the centre of mass has been removed.

tential. For the ${}^6\text{He}$ and ${}^8\text{He}$ binding energy calculations, the NCFC uses the JISP16 potential. This potential uses an “ab-exitu” approach, which compared to “ab-initio” approaches, uses the calculated two-body properties from NCFC to generate a two-body potential that minimizes the effects of three-body interactions. This allows rapid convergence of the calculation.

1.2.2.3 Hyperspherical harmonics expansion

The hyperspherical harmonic expansion (HH) method is an ab-initio method that calculates the nuclear properties by performing a matrix diagonalization on a wave function constructed using hyperspherical coordinates [Bar97]. Hyperspherical coordinates are a generalization in a multi-dimensional space of the usual spherical coordinates in three dimensions. The usage of these coordinates helps to shorten the computation time when intrinsic properties of the nuclei such as the binding energies and charge radii are calculated as it reduces the number of degrees of freedom by working in a coordinate system that does not involve the centre of mass. This is a particularity of the HH method as most ab-initio methods use particle coordinates, where the origin of the coordinate system is situated outside the nucleus.

In order to remove the motion of the centre of mass (CM), the hy-

perspherical harmonic expansion method converts particle coordinates into Jacobi coordinates as shown in figure 1.11. The first Jacobi coordinate η_0 is linked to the CM by

$$\vec{\eta}_0 = \frac{1}{\sqrt{A}} \sum_i^A \vec{r}_i = \sqrt{A} \cdot \vec{R}_{CM}, \quad (1.27)$$

where A is the number of nucleons in the nucleus and \vec{R}_{CM} is the centre of mass position with respect to the particle coordinates origin. The other Jacobi coordinates η_i , with $i > 0$, are defined by the relative position of the different nucleons. As the Jacobi coordinates form an orthonormal set, one can use them as basis to create an other sets of coordinates. One possibility are the hyperspherical ones. In general, one uses a radial coordinate, the hyperradius $\rho = \sqrt{\sum_i \eta_i^2}$ and a set of $3A-4$ hyperangles [Bar97]. Once constructed, the hyperspherical wave function presents a key feature to describe halo nuclei: an exponential asymptotic behaviour. This arises from the exponential decay describing the hyperradial dependance of the wave function.

The binding energy and radius of ${}^6\text{He}$ were calculated using the so-called V_{lowk} potential [Bog03]. This is a realistic potential just as the AV18 [Wir95] and CD-Bonn [Mac01] but it needs much smaller Hilbert space to converge. The V_{lowk} potential is derived from effective field theory [Mac07], which is a low-energy approximation of QCD.

One important parameter of the V_{lowk} potential is the cut-off Λ . This cut-off parameter defines the size of the basis in momentum space in which the calculation is performed. In principle, once all the terms in the Hamiltonian (equation (1.22)) are included, the calculation results should not depend on the parameter Λ [Bog03]. However, if the calculations are restricted to the use of two-nucleon potential, then varying the cut-off Λ one observes Λ -dependence on the results which is primarily due to the missing short range many-body potentials. Therefore, one can probe the effect of the missing many-body potential by varying the cut-off parameter. Such test is performed on the binding energy calculations of ${}^6\text{He}$ (see section 5.2).

While the transformation into hyperspherical coordinates is beneficial for nuclei with mass number $A \leq 6$, the antisymmetrisation of Jacobi coordinates becomes complicated when $A > 6$. Hence, hyperspherical harmonics expansions have not yet been used for ${}^8\text{He}$.

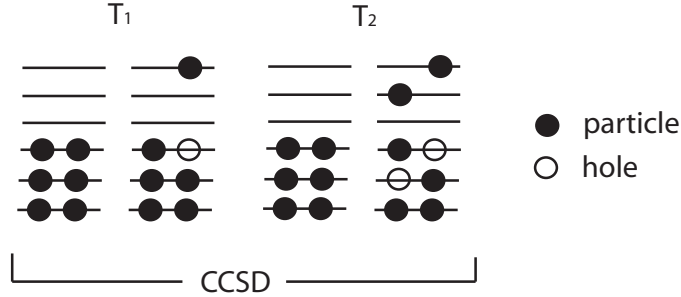


Figure 1.12: Construction of the coupled cluster single-double (CCSD) correlated wave function using particle excitation.

1.2.2.4 Coupled cluster theory

Coupled cluster (CC) theory is an ab-initio method that calculates the binding energy of a nucleus using

$$E_B = \langle \Psi_0 | e^{-T} H e^T | \Psi_0 \rangle, \quad (1.28)$$

where H is a general Hamiltonian, as in equation (1.22). In CC, the nuclear wave function is constructed by using the ansatz $|\Psi\rangle = e^{-T}|\Psi_0\rangle$ on an uncorrelated Slater determinant wave function $|\Psi_0\rangle$ called the reference state. T is an operator that imprints many-particles, many-holes excitation onto the reference state, as shown in figure 1.12. This operator is expanded into clusters, where clusters are referred to as the T_i in the expression $T = T_1 + T_2 + \dots$. If T is truncated at the T_2 level, then only singles-doubles interactions are allowed and the model terminology used is coupled cluster single double (CCSD).

The choice of the starting Slater determinant depends on the application. For ${}^8\text{He}$, a Hartree-Fock (HF) wave function was chosen as it displays an exponential asymptotic behaviour important for halo nuclei [Hag06]. To calculate the properties of ${}^8\text{He}$, coupled cluster theory used the same V_{lowk} potential as for the hyperspherical harmonic expansion calculation of ${}^6\text{He}$.

Coupled cluster (CC) theory [Hag07a] is exact only if T is expanded up to an A -body operator, but CCSD has proven to work very well for nuclei which have a closed sub-shell. Since ${}^8\text{He}$ has the $p_{3/2}$ sub-shell closed (e.g. ${}^{16}\text{O}$ and ${}^{40}\text{Ca}$ [Hag07b]), it can be treated using CC.

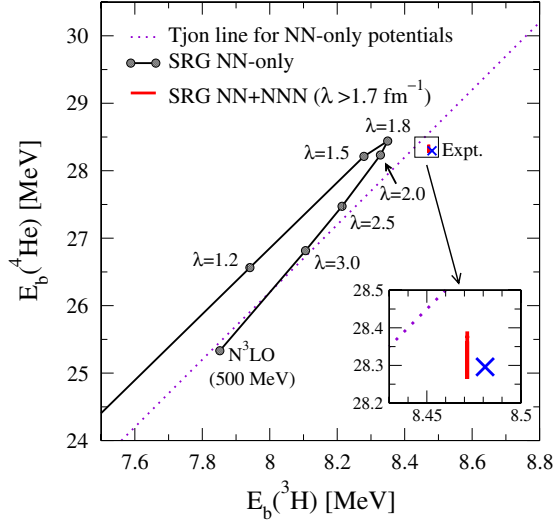


Figure 1.13: Effect of varying the cut-off λ on the NCSM calculation results for the ^4He and ^3H binding energies E_b using evolved chiral two-body potential (black line) and when including three-body potentials (red line). The dotted line indicates the so-called Tjon-line. The cross shows the experimental value. Figure from [Jur09].

1.2.3 Summary of the methods and need for three-nucleon potential

In this section we introduced four different ab-initio methods: the Green Function Monte-Carlo, the No-Core Shell Model, the Hyperspherical Harmonic expansion and the Coupled Cluster theory. In chapter 4 we compare these different methods with the experimental values for the binding energies and the radii of ^6He and ^8He . We expect to see larger deviations in the predicted binding energies for the methods that uses only two-body potentials compared to the one that includes three-body potentials. The effect of the missing three-nucleon potential has been studied using different methods and potentials for ^4He and ^3H . In fact, there exist a correlation between the calculated binding energies of ^4He and ^3H using various potentials. All these binding energies fall along a straight line called “Tjon-line”, after J.A. Tjon who first observed this correlation in calculated binding energies between ^4He and ^3H [Tjo75]. Figure 1.13 shows the Tjon-line (dotted in the figure) derived from many-body calculations using CD-Bonn and AV18

1.3. Other motivations for precise mass measurement: change in nuclear structure

potentials [Nog04]. Note that this line does not intersect the experimental values for the binding energies. Figure 1.13 also shows the effect of varying the cut-off parameter λ (analogous to the cut-off parameter Λ for V_{lowk}) on the calculated binding energies of ${}^4\text{He}$ and ${}^3\text{H}$. These calculations are done by the NCSM method using evolved chiral potentials [Jur09]. When only two-body potentials (NN) are considered, there are large variations in the binding energies for both ${}^4\text{He}$ and ${}^3\text{H}$ with the cut-off λ . For none of the cut-off parameters the calculated binding energies of ${}^4\text{He}$ and ${}^3\text{H}$ simultaneously agree with the experimental ones. However, once a three-body potential (NNN) is included, the results change weakly with λ , while offering closer values to experiment. Note that only the binding energy of ${}^4\text{He}$ changes with λ . This could be an effect of the missing four-body potential, which are not present for the three-nucleons nuclei ${}^3\text{H}$. In summary, we anticipate to see deviations between the calculated binding energies for ${}^6\text{He}$ and ${}^8\text{He}$ compared to experiment when only two-body potentials are used. Being the only method to use three-body potentials for ${}^6\text{He}$ and ${}^8\text{He}$, the GFMC is expected to give a better description of the experimental data. More details are discussed in chapter 4, section 4.4.

1.3 Other motivations for precise mass measurement: change in nuclear structure

One of the features of a nucleus is that its mass is lower than the sum of the mass of its constituents. This difference in mass is called the mass defect and is reflected in the binding energy of the nucleus. As we already saw for halo nuclei, the binding energy of a nucleus depends on the nature of the interaction within the nucleus. Therefore, explaining the binding energy of nuclei is an important question in nuclear physics. There are several approaches developed over the years at aiming to explain the binding energy of nuclei.

Historically, the most well-known of these models is the liquid drop model for which the binding energy is given by

$$E_B(N, Z) = -a_v A + a_{sf} A^{2/3} + a_c Z(Z-1)A^{-1/3} + a_{sym} (Z-N)^2/A \pm \delta(A) \quad (1.29)$$

where a_i are coefficients and $\delta(A)$ is the pairing term. The term given by the coefficient a_v is the volume term, a_{sf} represent a surface-tension term, a_c is a consequence of the coulomb interaction among nuclei and a_{sym} is a phenomenological term to explain the larger binding energy of $N = Z$

1.3. Other motivations for precise mass measurement: change in nuclear structure

nuclei. The pairing term $\delta(A)$ is negative for even number of protons and neutrons, positive for odd number of protons and neutrons and zero if either the number of protons or neutrons is odd. The saw-tooth pattern seen in figure 1.5 for the one-neutron separation energy is caused by this pairing term. Change in the binding energy along an isotopic chain are seen through the two-neutron separation energy S_{2N} .

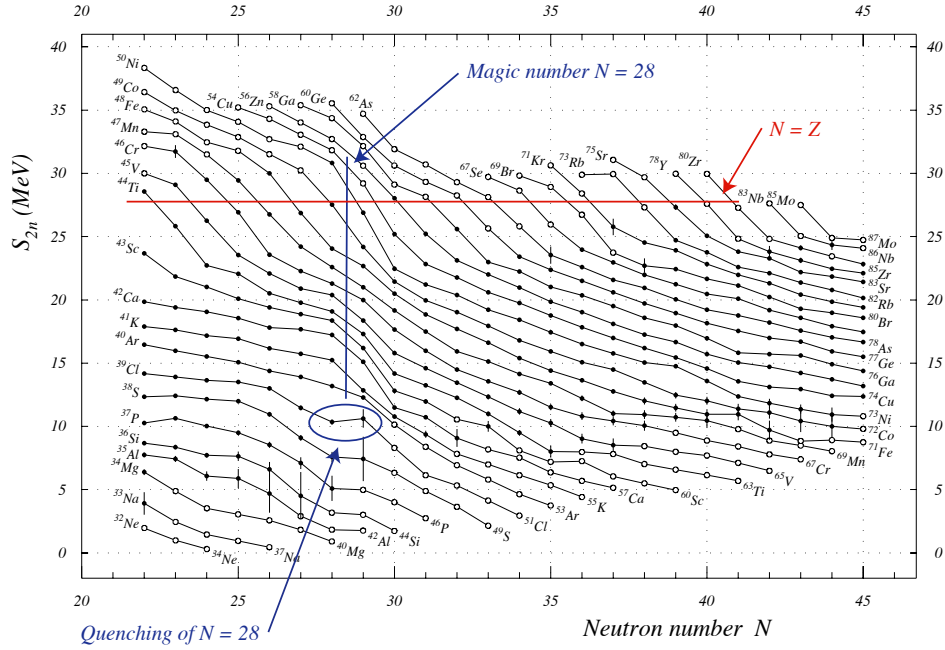


Figure 1.14: Two-neutron separation energies from the AME03 [Aud03]. Shown are the drop in S_{2N} due to the symmetry term in equation (1.29) for $N = Z$, the drop at magic number $N = 28$, as well as the quenching of this magic number for ^{45}Cl . The solid circles are derived from measured masses, while the open circles are extrapolated values. Original figure from [Aud03].

Figure 1.14 shows the S_{2N} values for the isotopic chains in the range $N = 22$ to 45 using the mass values from the AME03 [Aud03]. The steady decrease in S_{2N} with N is a consequence of the nuclear force saturation. This results in a decrease in the binding energy when more nucleons are added and it is taken into account in equation (1.29) by the surface term $a_{sf}A^{2/3}$. An other feature of equation (1.29), shown in figure 1.14, is the large gap in S_{2N} caused by the symmetry term $a_{sym}(Z - N)^2/A$ for $N = Z$.

1.4. Other motivations for precise mass measurement: test of the CKM matrix unitarity

However, one particular feature can be seen in figure 1.14 which cannot be explained by the liquid-drop model, and it is the sudden drop in S_{2N} happening at $N = 28$. This is explained by the shell structure of nuclei [Hax49, May49], which is analogous to the electronic shell structure found in atomic physics. As in atomic physics, there is closed-shell structure leading to enlarge spacing in energy between shells. The nuclear physics equivalent of a noble gas is the so-called *magic number* nuclei, which are those with N and/or $Z = 2, 8, 20, 28, 50, 82, 126$.

However, one of the main differences between electronic and nuclear structure, is that the later involves two different particles (neutrons and protons) that interact with each another. As a consequence, when there is a large N -to- Z imbalance, the *magicity* of a certain nucleon number (either N or Z) start to fade. This is shown in figure 1.14, by the quenching of the observed drop in two-neutron separation energy of $N = 28$ for ^{45}Cl . At the same time, new magic numbers start to emerge, like $N = 16$ [Oza00] which was discovered through a survey of the S_N of neutron-rich nuclei. This migration of magic numbers due to changes in the shell structure have been studied extensively [Kan02] and an accurate knowledge of atomic masses has proven to be a critical and sensitive tool [Gue06, Hak08].

1.4 Other motivations for precise mass measurement: test of the CKM matrix unitarity

The Standard Model (SM) of particle physics, which describes the interactions of elementary particles, is currently tested by many experiments. One of the tests of the Standard Model is the verification of the unitarity of the Cabibbo-Kobayashi-Maskawa (CKM) matrix [Cab63, Kob73]. Within the Standard Model, the quarks are the basic constituents that are affected by both the strong and weak interactions. The different types of quarks can be divided in two groups that have identical charges and different masses. The first group comprise the up, charm and top quarks and the second group the down, strange and bottom quarks. These quarks represent the eigenstates of the strong interaction. However, these are not the eigenstates of the weak interactions and the coupling matrix between the eigenstates of these two interactions is called the CKM matrix. This matrix couples the

1.4. Other motivations for precise mass measurement: test of the CKM matrix unitarity

weak eigenstates with the strong eigenstates as follows:

$$\begin{pmatrix} |d_w\rangle \\ |s_w\rangle \\ |b_w\rangle \end{pmatrix} = \begin{pmatrix} V_{ud} & V_{us} & V_{ub} \\ V_{cd} & V_{cs} & V_{cb} \\ V_{td} & V_{ts} & V_{tb} \end{pmatrix} \begin{pmatrix} |d_s\rangle \\ |s_s\rangle \\ |b_s\rangle \end{pmatrix}$$

where d , s and b are the down, strange and bottom quarks respectively and w , s respectively denotes the weak and strong eigenstates. The square of each CKM matrix element V_{ij} represents a probability of transition of a quark state under the weak interaction. For example, $|V_{ud}|^2$ is the probability of a u -quark mixed into a d -quark. Under the Standard Model assumption that there are only six types of quarks, the CKM matrix has to be unitarity:

$$\sum_i |V_{ui}|^2 = |V_{ud}|^2 + |V_{us}|^2 + |V_{ub}|^2 = 1. \quad (1.30)$$

The violation of the CKM matrix unitarity could be caused by quantum loop corrections in the quark mixing resulting in unobserved new particles such as the neutral gauge boson Z_χ [Mar87]. From the last compilation of all available experimental data, including all theoretical corrections, the CKM matrix agrees with unitarity [Har09]:

$$\sum_i V_{ui}^2 = 0.99995 \pm 0.00061. \quad (1.31)$$

However, this was not always the case, as previous evaluations the CKM matrix were found to disagree with unitarity by 2.4σ [Har05]. This deviation was corrected with re-evaluations of the V_{us} [Sci08] and V_{ud} [Har09] matrix elements (note that V_{ub} matrix element, due to its small size, contributes to a negligible 0.001% to unitarity).

Measuring the V_{us} and V_{ub} terms is the domain of particle physics. However, the V_{ud} term only involves the up and down quarks, which are the constituents of protons ($p = u+u+d$) and neutrons ($n = u+d+d$). Therefore, this term is accessible through nuclear physics experiments and it can be determined from the measurement of the ft -values of super-allowed $0^+ \rightarrow 0^+$ β -decays. The ft -value, or ‘‘comparative half-life’’, is given by the product of the partial half-life of the decay with the phase-space factor, f . The super-allowed $0^+ \rightarrow 0^+$ β -decays are decays between states of spin $J = 0$ and positive parity, hence $J^P = 0^+$. This type of transition, where the change in spin $\Delta J = \Delta S = \Delta L = 0$, is called a Fermi transition. In the Fermi theory of β -decay, the ft -value is given by [Kra88]:

$$ft = \frac{K}{G_V^2 |M_F|^2} \quad (1.32)$$

1.4. *Other motivations for precise mass measurement: test of the CKM matrix unitarity*

where G_V is the vector coupling constant, K is a numerical constant and M_F is the Fermi matrix element. The vector coupling constant is linked to the weak-interaction coupling constant G_F of a purely leptonic muon decay through the matrix element V_{ud} :

$$G_V = V_{ud}G_F. \quad (1.33)$$

For nuclei with isospin $T = 1$, $M_F = \sqrt{2}$.

The conserved vector current (CVC) hypothesis asserts that the ft -value should be independent of the parent and daughter nuclei of a $0^+ \rightarrow 0^+$ β -decay. This means that there is no coupling between the vector components of the weak and the strong interactions. In reality, equation (1.32) needs to be modified to account for several effects. Firstly, the isospin is not an exact symmetry in the nuclei, which means that the Fermi matrix element needs to be corrected (e.g. for $T = 1$ transitions, $M_F = \sqrt{2(1 - \delta_c)}$), where δ_c is called the isospin-symmetry-breaking correction. Secondly, the ft -values needs to be adjusted to account for radiative corrections that are nucleus-dependant, δ_R , and nucleus-independent, Δ_R^V . With these corrections, the ft -values for $T = 1$ becomes:

$$Ft = ft(1 - \delta_c)(1 + \delta_R) = \frac{K}{2|V_{ud}|^2 G_F^2 (1 + \Delta_R^V)} = \text{constant} \quad (1.34)$$

The experimental part of the Ft -value comes from the half-life $T_{1/2}$, the branching ratio BR and the Q -value of the $0^+ \rightarrow 0^+$ transitions [Har05]. The Q -value of a nuclear reaction is given by the difference of mass between the reactant and the product:

$$Q = m(\text{reactant}) - m(\text{product}). \quad (1.35)$$

The correctness of the Conserved Vector Current (CVC) hypothesis can be verified by taking the weighted mean of the measured Ft -values and looking for non-statistical deviations from the mean. However, the current data set is consistent and is in agreement with the CVC at the 1.3×10^{-4} level [Har09]. The matrix element V_{ud} is then calculated from the average \overline{Ft} -value,

$$|V_{ud}|^2 = \frac{K}{2G_F^2 (1 + \Delta_R^V) \overline{Ft}}, \quad (1.36)$$

of 13 well-known $0^+ \rightarrow 0^+$ transitions [Har09].

The importance of high accuracy mass measurements comes from the calculation of the statistical rate function f , which is strongly dependent on

1.4. Other motivations for precise mass measurement: test of the CKM matrix unitarity

the Q -value of the transitions. Therefore, direct mass measurements, which lead to a precise determination of Q -values, play an important role in the determination of V_{ud} .

In 2005, after measuring the Q -value for the super-allowed $0^+ \rightarrow 0^+$ emitter ^{46}V [Sav05], the Canadian Penning Trap (CPT) experiment found a 2.19 keV difference between their results and the last compilation of all available experimental data. After further investigation, they discovered a

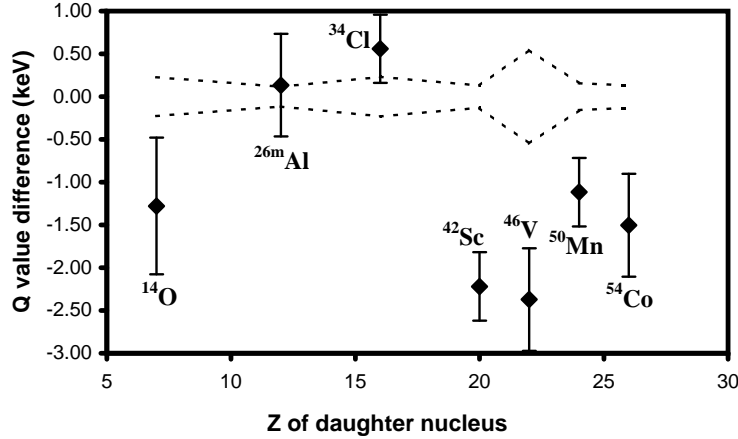


Figure 1.15: Q -value difference between [Von77] and the weighted average of all other data. The dotted line represents the uncertainty (from [Sav05]).

set of seven measurements [Von77] which measured Q -values were off by 2 to 5σ from the rest of the compilation data (see Figure 1.15). After removing the inconsistent data, the new value of V_{ud} became 0.9745(16), which brought the CKM matrix closer to unitarity:

$$|V_{ud}|^2 + |V_{us}|^2 + |V_{ub}|^2 = 0.9985(12) \quad (1.37)$$

compared to the previous result of 0.9966(14) [Har05]. Since the measurement from [Sav05], the ^{46}V decay Q -value has been confirmed by the JYFLTRAP experiment [Ero06] and deviations of the ^{42}Sc [Ero06] and ^{50}Mn , ^{54}Co [Ero08] decay Q -values with respect to [Von77] has been observed.

Currently, the dominant source of uncertainty in the V_{ud} determination comes from the theoretical correction δ_c , which does not currently reside on solid footing. Depending on the calculation method used, conflicting theoretical correction δ_c results are obtained. In their 2005 V_{ud} evaluation,

1.4. *Other motivations for precise mass measurement: test of the CKM matrix unitarity*

Towner and Hardy showed that when using δ_c based on Wood-Saxon calculations [Tow77, Tow02] a $\overline{Ft} = 3072.6(8)$ s is obtained, while calculation using Hartree-Fock eigenfunctions [Orm95] leads a higher value of $\overline{Ft} = 3074.5(8)$ s. In the most recent evaluation [Har09], Towner and Hardy indicated that the previous Hartree-Fock calculations could be, in their words, flawed. Therefore such inconsistency requires the need for an independent calculation of the correction δ_c . Such calculations are on their way and there is also a new calculation approach being proposed [Aue09, Lia09, Mil09]. On the experimental side, more precise and accurate data are needed to be used as test-bench for these different calculation approaches.

One of the nuclei for which the correction δ_c is important is ^{74}Rb . The most important experimental source of uncertainty on this decay comes from the atomic mass of ^{74}Rb [Kel04]. In order to have a similar error on the Q -value for this decay, as the other β -decays presented in [Har09], one needs to perform a mass measurement of this nucleus to a level of precision of 5×10^{-9} . An accurate mass measurement at that level of precision can only be achieved using a Penning trap mass spectrometer. The mass measurement of ^{74}Rb is planned to be measured at the TITAN facility using highly charged ions.

Chapter 2

The experimental setup

The TITAN (TRIUMF Ion Trap for Atomic and Nuclear science) facility [Dil06] includes a Penning trap mass spectrometer capable of performing high precision mass measurements on radioactive species. Example of such measurement are the halo nuclei ^{11}Li [Smi08b], ^{11}Be [Rin09a], ^8He [Ryj08] and ^6He . The TITAN facility is situated in the low-energy section of the

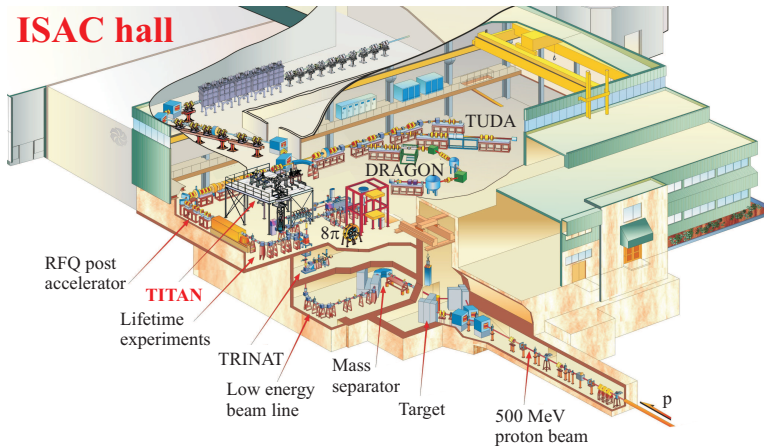


Figure 2.1: Layout of the TITAN facility inside the ISAC experimental hall at TRIUMF.

Isotope Separator and ACcelerator (ISAC) experimental hall [Dom00] of TRIUMF, as indicated in figure 2.1. At TITAN, there are various research activities taking place; yet the possibility to perform high-precision mass measurements of highly-charged unstable ions (HCI) is the distinctive feature of TITAN. The use of HCI is due to the fact that the precision level of the measurements linearly increases with the charge state.

High-precision mass measurements are carried out at TITAN, which require a preparation of the ion through several processes. The ISAC continuous ion beam is delivered to TITAN. There, it is cooled and bunched using a

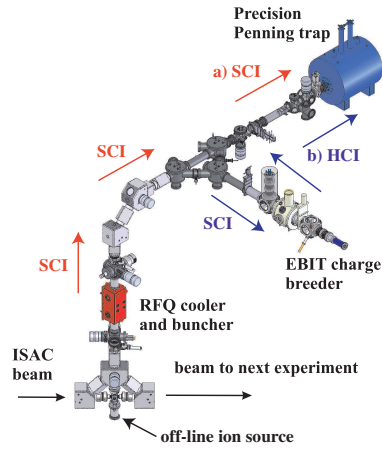


Figure 2.2: The TITAN experimental setup which includes a RFQ, a high-precision Penning trap, an EBIT and an off-line ion source. a) Shown in red is the path of the beam when mass measurement on singly charge ions (SCI) is performed. b) In blue is the path for highly charged ions (HCI) mass measurement.

gas-filled linear radio-frequency quadrupolar (RFQ) trap ([Smi06, Smi08a]). The subsequent step depends on whether a mass measurement using singly charged ions (SCI), or highly charged ions is performed. The ions can either be transferred to an electron-beam ion trap (EBIT) [Fro06], where charge breeding takes place (blue path in figure 2.2) or directly sent to the Penning trap (MPET) where the mass of the ion of interest is determined (red path in Figure 2.2).

In this chapter, we present how an ion beam is produced and delivered by the ISAC facility, how the beam preparation devices (i.e. the RFQ, the EBIT and the transport optics) are employed, and how the mass of an ion is determined by the TITAN Penning trap. The Penning trap is presented in more detail as this device is at the core of this thesis.

2.1 Beam production and separation at ISAC

The Isotope Separation and ACceleration (ISAC) facility produces radioactive ion beams by the Isotope Separator On-Line (ISOL) method [Dom02]. In this well-established method, unstable ions are produced by bombarding a thick target, such as the one shown in figure 2.3, with a 500 MeV con-

2.1. Beam production and separation at ISAC

tinuous proton beam coming from the TRIUMF cyclotron. The current on target of that beam can go as high as $100 \mu\text{A}$. Once produced, different nu-

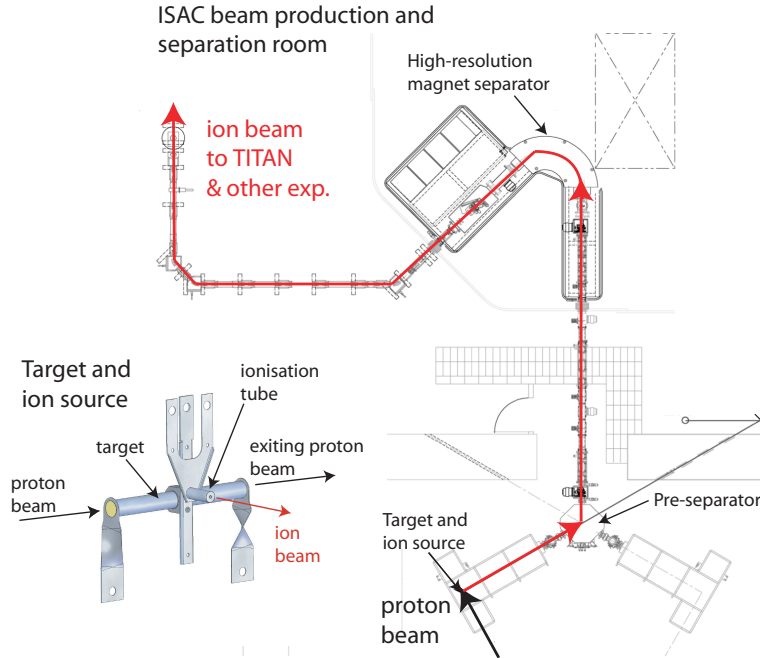


Figure 2.3: The ISAC production and separation room. This room includes two target stations, target and ion sources, a pre-separator and a high-resolution ($m/\Delta m = 3000$) magnet separator. Also shown is a rendering of the target and a surface ion source.

clei diffuse out of the target and are then ionized by an ion source [Dom02]. Subsequently, the ionized isotopes are extracted and formed into a beam which is electrostatically accelerated to an energy of 12 to 60 keV. It is later guided to a two-stage dipole magnet separator that include a pre-separator and a high-resolution magnet separator (figure 2.3). This separates and selects the ions of interest according to their mass-to-charge ratio (m/q) at a resolving power of typically $m/\Delta m = 3000$. Finally, the separated beam is delivered to the ISAC hall where various experiments are located.

The two species of interest to this thesis, ${}^6\text{He}$ and ${}^8\text{He}$, are produced using a SiC target and ionized by the so-called Forced Electron Beam Ion Arc Discharge (FEBIAD) source [Bri08]. Using this technique, ionization is done via a plasma generated by injecting atomic gas into a chamber where

2.2. Beam preparation: the radio-frequency quadrupole (RFQ) cooler and buncher

Isotope	Isotope Δ (keV)	contaminant	cont. Δ (keV)	$m/\Delta m$
${}^6\text{He}$	17 592.09(6)	${}^6\text{Li}$	14 086.88(2)	1600
${}^8\text{He}$	31 609.74(12)	${}^8\text{Li}$	20 945.80(11)	700

Table 2.1: Resolution $m/\Delta m$ required to separate ISAC contaminants for ${}^6\text{He}$ and ${}^8\text{He}$. The ${}^8\text{Li}$ mass excess (Δ) is from [Smi08b] and the others are from this work.

a hot filament produces electrons. The feature of this technique is that it is non-selective and can ionize various gas molecules in the chamber. This leads to an ion beam with possible isobaric contamination. However, because of their light mass, there is very limited contamination close to the mass of ${}^6\text{He}$ and ${}^8\text{He}$ in the beam. In fact, the two contaminants with the closest mass to ${}^6\text{He}$ and ${}^8\text{He}$, were ${}^6\text{Li}$ and ${}^8\text{Li}$. Their mass excess, together with the mass excess of the ions of interest, are presented in table 2.1. The relative mass difference of ${}^6\text{Li}$ compared to ${}^6\text{He}$ is 1600, while for ${}^8\text{Li}$ compared to ${}^8\text{He}$ it is 700. Since the relative mass difference $m/\Delta m$ of both species is less than the resolving power of the mass separator, which is 3000, they can both be separated from the helium isotopes.

2.2 Beam preparation: the radio-frequency quadrupole (RFQ) cooler and buncher

The RFQ is a beam preparation device for accumulating, cooling and bunching the continuous ion beam coming from either the TITAN off-line ion source or ISAC. Prior to its injection in this device, the beam is decelerated to tens of eV which is achieved by floating the electrode structure of the trap on a high voltage (HV) potential slightly below the beam energy. This allows one to stop and accumulate the beam in the RFQ.

In the RFQ the beam energy spread is dissipated through collisions with inert buffer gas. This leads to cooling of the beam, thus reducing its transverse and longitudinal emittance. The emittance is a measure of the departure of the beam properties from the ideal case. Ideally, all particles within the beam should travel at the same velocity and along the same direction. However, in reality it is not the case and leads to a diverging beam with a certain energy spread. The “divergence” of the beam is quantified by the transverse emittance which measure the area occupied by the beam in the x - θ_x space. The TITAN RFQ has been designed in order to accept an ISAC

2.2. Beam preparation: the radio-frequency quadrupole (RFQ) cooler and buncher

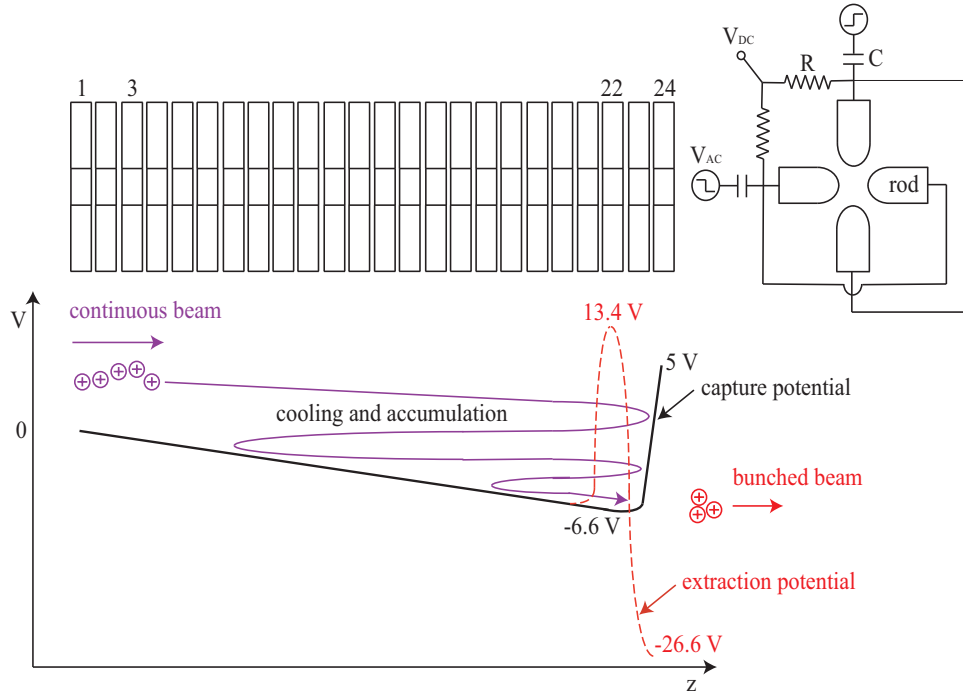


Figure 2.4: Top: Schematic sideview of TITAN’s RFQ which is composed of four 24-segmented rods that create a longitudinal trapping potential. A well allows for beam accumulation and subsequent bunching. A square-wave RF is applied to the opposite segments to provide radial confinement. Bottom: Schematic potential distribution for accumulation (solid line) and bunch extraction (dashed line).

beam with $\epsilon_{99\%} = 50 \pi$ mm mrad transverse emittance at 60 keV energy [Smi08a]. The transverse emittance of the beam leaving the RFQ is approximately $\epsilon_{99\%} \approx 10 \pi$ mm mrad at 1 keV. The measured full width half maximum (FWHM) of the beam energy spread at this energy is typically around 6 eV [Cha09].

The typical buffer gas used to cool the beam is helium, due to its inert nature and light mass allowing favorable momentum transfers for efficient energy spread dissipation. However, for the ${}^6,8\text{He}$ mass measurements the beam was cooled using hydrogen to avoid resonant charge exchange reactions. Figure 2.4 shows that the TITANs RFQ is composed of a four rod structures on which a radio-frequency quadrupolar field is applied to create

2.3. Beam preparation: beam transport to the Penning trap

a net centring force. This force is strong enough to counter the dispersion of the beam caused by reactions with the buffer gas. Note that the centring of the ion depends not only on the applied RF frequency and amplitude, but also on its mass. Therefore, the RFQ can be operated with a certain mass selectivity.

The four rods are longitudinally segmented in 24 segments that provide a potential gradient which guides the ions towards a potential well near the end of the structure. Hence, the beam is accelerated along the RFQ and accumulated in the well for subsequent bunching. Bunching is achieved by periodically switching the voltages at the 22th and 24th segments.

As a final remark, inside the RFQ, the beam can charge exchange with the residual gas and this leads to beam loss and potentially generates other ions which contributes to produces beam contamination. However, part of that contamination can be removed from the RFQ by the choice of RF amplitude and RF frequency. This mass selectivity is sufficient to remove the identified contaminants, such as H_2O , from the ${}^{6,8}\text{He}$ beam.

2.3 Beam preparation: beam transport to the Penning trap

The beam line connecting the RFQ and the Penning trap allows for an efficient, close to 100%, transmission of the ions between the two traps. This section describes ion optical elements that are discussed in more detail later in the text. Figure 2.5 shows a schematic of the transport beamline between the RFQ and the Penning trap. Some of the main components include a pulse drift tube (PB5) situated after the RFQ, two 45 degrees benders (B1) connecting the vertical and horizontal sections, a time-of-flight gate, one micro-channel plate (MCP) detector for beam diagnosis, a Lorentz steerer (LS) and another pulse drift tube (PLT). In this section we follow the progression of the ion beam as it goes through these various components.

Initially, upon extraction from the RFQ the ion beam is accelerated into the pulse drift tube (PB5). The purpose of this device is to transfer the beam from the high voltage (HV) RFQ section to the beam line that is at ground potential. Moreover, it sets the transport beam energy. In detail, the pulse drift tube shares the same potential as the RFQ but uses an off-set of 1 to 2 kV below the RFQ (HV) potential. Hence, the ion bunch is accelerated from the RFQ into the PB5 and gains 1 to 2 keV kinetic energy. While the bunch is inside the drift tube, it is switched to the ground potential. Subsequently, when the bunch leaves the PB5, it is not accelerated and keeps its kinetic

2.3. Beam preparation: beam transport to the Penning trap

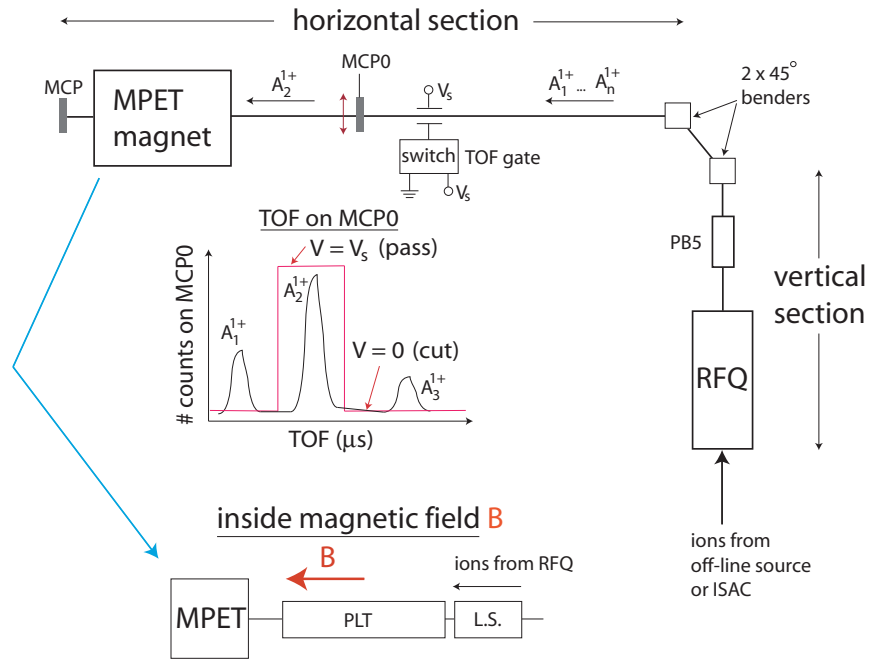


Figure 2.5: Block diagram of a section of the TITAN beam line. Shown are the RFQ, RFQ pulse drift tube (PB5), the two 45 degrees benders, the time-of-flight gate (TOF gate), the MCP0 and the Penning trap magnet. Inside the magnetic field, we show the Lorentz steerer (LS), MPET pulse drift tube (PLT) and the Penning trap (MPET).

2.3. Beam preparation: beam transport to the Penning trap

energy constant. This process does not perturb the beam and allows for its transportation at an adjustable energy of 1-2 keV.

Two 45 degrees benders are located between the vertical and horizontal sections of the beam line (see figure 2.5). The role of these benders is to electrostatically deflect the ions between the two sections with minimal losses. This is done by applying a potential difference $\Delta B1$ between two sets of spherical plates. The transfer efficiency through the bending section is particularly sensitive to the potential on these electrodes with respect to the beam energy. In section 3.4.3.2 we show how we can estimate the beam energy from the bend potential difference $\Delta B1$.

The beam is further transported using conventional ion optics elements and enters a so-called time-of-flight (TOF) gate. The purpose of this gate is to reduce remaining non-isobaric contamination before the Penning trap. The principle of this gate is simple; since all ions are transported at the same energy, ions of different mass arrive at different times at the position of the gate. Unwanted species can then be removed by applying a deflecting potential on a pair of electrodes. The graph in figure 2.5 shows how one single species (A_2^+) can be selected to be transferred by applying a non-deflecting potential V_s during a time interval when it arrives at the steerer plates and a deflecting potential during the rest of the time to cut the contaminant ions (A_1^+ and A_3^+). The mass resolution of this gate is $m/\Delta m = 20$, which is enough for example to resolve ${}^6\text{Li}$ from ${}^7\text{Li}$.

Prior to the capturing of the ions in the Penning trap, there are two units of ion optics that the ions pass through: the Lorentz steerer [Rin07] and the pulse drift tube (PLT). The purpose of the Lorentz steerer is to prepare the ions on an initial magnetron radius before the injection in the trap. In section 2.4.4, we show that this preparation is important for the measurement process in the Penning trap. The Lorentz steerer radially displace the ions using perpendicular quadrupolar electric and magnetic fields as shown in figure 2.6. The magnetic field is produced by the Penning trap magnet and is axial with respect to the axis of incoming ions. The quadrupolar electric field is produced by the application of a potential offset, ΔV_{LS} , on two opposite segments of the Lorentz steerer. The displacement, d , of the ions upon leaving the Lorentz steerer is proportional to the offset potential. Note that ions are decelerated when entering the Lorentz steerer by the application of a potential that is about 65 V below the beam energy.

After the ions leave the Lorentz steerer, they enter a pulse drift tube. The purpose of this device is to reduce the ion bunch kinetic energy such that it has minimal energy once it is captured in the Penning trap. This is done by biasing the pulse drift tube at about 65 V below beam energy, just

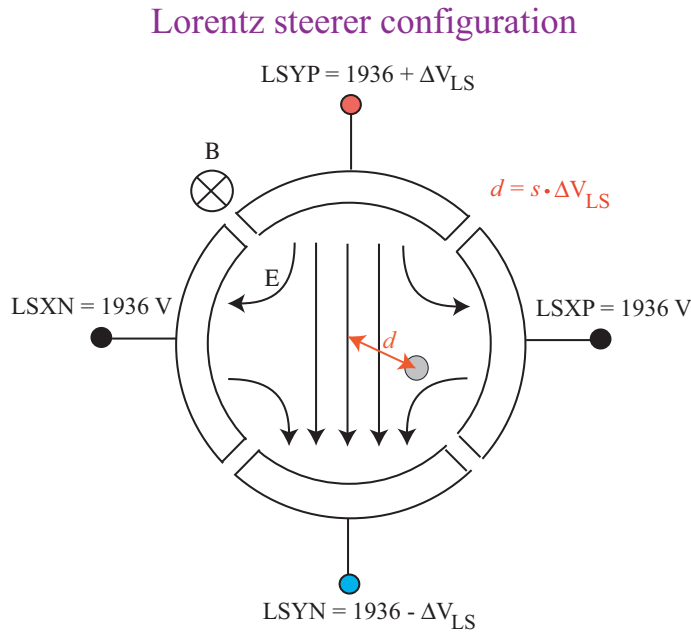


Figure 2.6: Schematic of the Lorentz steerer which comprise a quarted cylindrical electrode axially aligned with a magnetic field B . We show the potential needed to steer the beam and the corresponding electric quadrupolar field produced. The displacement, d , of the beam is proportional to the offset potential, ΔV_{LS} .

2.4. Beam preparation: the electron beam ion trap (EBIT)

as the Lorentz steerer. When the ions are in the drift tube, it is switched down to -65 V. The ions then leave the drift tube with 65 eV of kinetic energy. This is the energy needed for the ions to stop when they reach the trap centre.

2.4 Beam preparation: the electron beam ion trap (EBIT)

The purpose of the EBIT is to increase the charge state of the singly charged ions for mass measurements in the Penning trap. The TITAN EBIT pro-

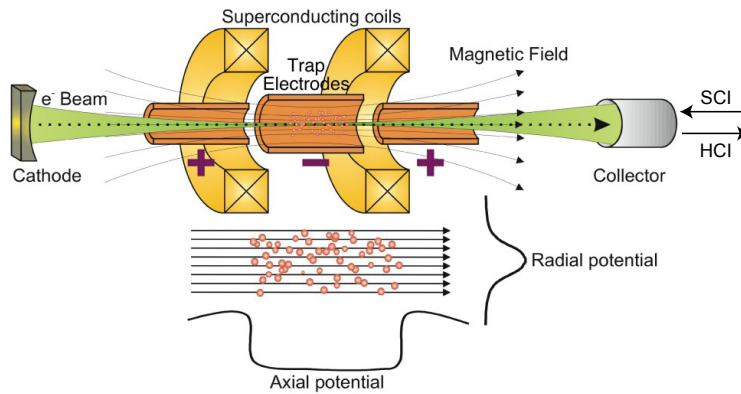


Figure 2.7: Schematic of TITAN's EBIT trapping region. Axial trapping is achieved by the application of a lower potential on the central drift-tube electrode segment with respect to the two end cap electrodes. The radial confinement of the ions is achieved by the 4-6 T magnetic field produced by Helmholtz coils and the compressed space-charge potential created by the electron beam.

duces and confines highly charged ions (HCI) by bombarding the singly charged ions with an intense, high current electron beam (figure 2.7). As the ion beam enters the trap from the collector side (see figure 2.7), it is axially confined by applying higher potential on the end cap cylindrical electrodes (indicated by a (+)) than the central trap electrode (indicated by a (-)). Inside the trap a strong (4-6 T) magnetic field, generated by a pair of Helmholtz coils, compresses and confines radially both the ion and electron beams.

A step-wise increase in charge state is achieved via a successive impact-ionization of the trapped ions with smaller ionization energy than the electron beam energy. The presence of the strong axial magnetic field at the trap centre compresses the electron beam radially, increasing the electron beam current density.

The maximum charge state of the ion beam is limited by the electron beam energy. To successfully strip off the electrons the beam energy has to be higher than the ionization potential. As electrons continue to be removed higher electron beam energy is required to remove an additional electron. Since November 2008, the EBIT is fully operational and HCI ions have been captured and masses have successfully been measured in the Penning trap.

2.5 The mass measurement Penning trap

The Penning trap is the principal trap of the TITAN facility where mass measurements are performed. Penning trap mass-spectrometer determine the mass M of a trapped ion of charge state q by measuring its cyclotron frequency

$$\nu_c = \frac{1}{2\pi} \frac{qB}{M} \quad (2.1)$$

in a magnetic field B . In the trap the ions are confined in three-dimensions by overlaying a quadrupolar potential and a magnetic field. The quadrupo-

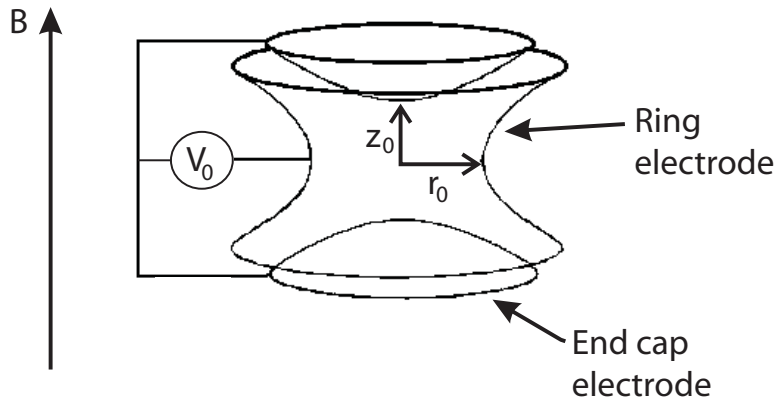


Figure 2.8: Schematic diagram of an ideal Penning trap including: a one-sheet hyperboloid forming the ring electrode, a two-sheet hyperboloid forming the end caps and an axial magnetic field.

lar potential is created by applying a potential difference V_0 between two orthogonal hyperboloids of rotations: one forming the ring electrode and the other forming the end caps electrodes, as shown in figure 2.8. This potential configuration axially traps the ions. The radial trapping is provided by an axial magnetic field, B .

This section discusses the various aspects of the ideal Penning trap such as the ion confinement and the ion motion. Afterwards, the mass measurement by time-of-flight resonance technique, used by the TITAN Penning trap is described.

2.5.1 Three-dimensional confinement

In this section we outline what type of potential and magnetic field can be used in order to confine a charged particle in three dimensions. Generally, in order to trap a charged particle in three dimensions a potential configuration that exerts such force

$$\vec{F} = -e\vec{\nabla}V, \quad (2.2)$$

is necessary. A convenient choice of potential is a harmonic potential

$$V = ax^2 + by^2 + cz^2. \quad (2.3)$$

To obey Laplace's equation, $\nabla^2 V = 0$, the sum of the different coefficients in (2.3) must be zero. This means that one of the coefficients must be negative. By having a cylindrical symmetry around the z -axis, one can simplify and set $a = b$, which leads to the condition $a = -c/2$ and:

$$V = c(z^2 - r^2/2), \quad (2.4)$$

where $r = \sqrt{x^2 + y^2}$ is the radial position of the particle.

In order to have an equipotential electrode surface, equation (2.4) must satisfy:

$$V(\text{surface}) = c(z^2 - r^2/2) = \text{constant} \quad (2.5)$$

This is the equation of two hyperboloid of revolution; where one points along the axial direction and the other along the radial direction. This is shown in figure 2.8. The value of constant c is set from the potential difference between the two hyperbolas:

$$V_0 = V(z_0, 0) - V(0, r_0) = c(z_0^2 + r_0^2/2) \quad (2.6)$$

$$c = \frac{V_0}{2d_0^2}, \quad (2.7)$$

2.5. The mass measurement Penning trap

where $d_0 = \sqrt{z_0^2/2 + r_0^2/4}$ is defined as the characteristic length of the trap. Therefore, the potential produced by the trap is:

$$V = \frac{V_0}{2d_0^2}(z^2 - r^2/2). \quad (2.8)$$

Figure 2.9 shows the feature of such potential; there is no three-dimensional

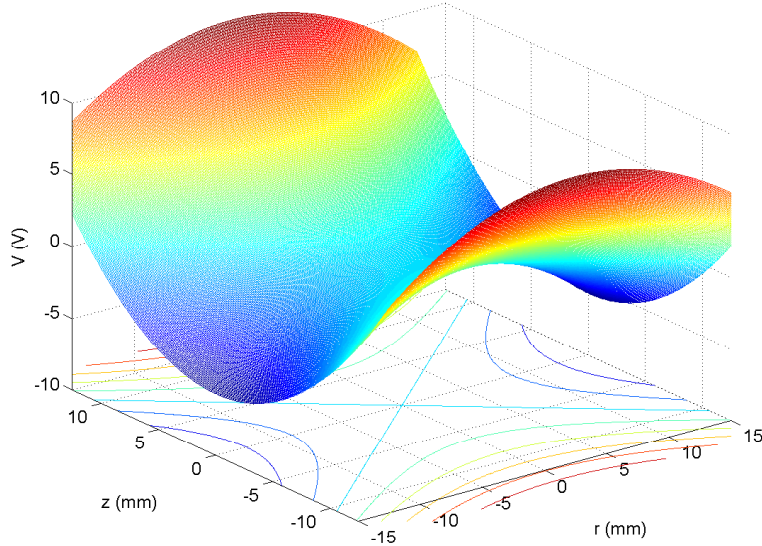


Figure 2.9: Typical quadrupolar electric potential of a Penning trap. See text for details.

minimum. Therefore, such potential cannot confine an ion in three dimensions. This is a direct consequence of the Laplace equation which does not allow local minima or maxima except along the boundaries.

This can be overcome in two possible ways, allowing one to confine a charged particle in three dimensions. Firstly, by alternating the sign of V_0 the ions will experience an average central force. This method is employed in the so-called Paul trap. Please refer to [Gos95] for a detailed discussion about Paul traps. The second method uses a magnetic field along the axial direction to radially trap the ions. This method is used in a Penning trap.

2.5.2 The TITAN Penning trap electrode structure

This section shortly introduces the various electrodes forming the TITAN Penning trap. Figure 2.10 (a) is a schematic of the TITAN Penning trap

2.5. The mass measurement Penning trap

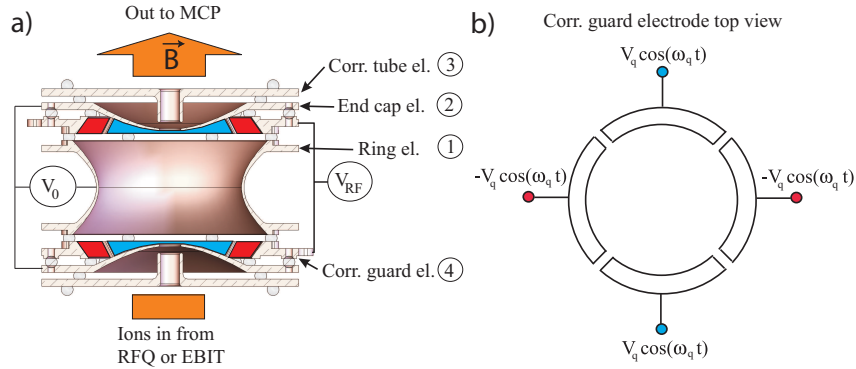


Figure 2.10: a) Illustration of the TITAN Penning trap electrode configuration formed by the hyperbolic ring (1), end cap electrodes (2), tube (3) and guard (4) correction electrodes. The RF is applied on (4). b) Application of a quadrupolar excitation on the correction guard electrode ((4) in a).

electrode structure. The trap is composed of two hyperboloids of revolution forming one ring (label (1) in figure 2.10) and two end cap electrodes (2). The ions are axially trapped by a harmonic quadrupole electrostatic potential produced by a potential difference, V_0 , between the ring and the end cap electrodes, as shown in figure 2.10. Some anharmonicities in the trapping potential are introduced by the holes in the end-cap electrodes and by the finite size of the hyperbolic electrodes. Two sets of correction electrodes (labeled (3) and (4) in figure 2.10), are used to compensate for higher-order electric field components (for more detail see section 3.3). The radial confinement is provided by a magnetic field B . Figure 2.10 (b) shows how the quadrupolar excitation necessary for the mass measurement by TOF-ICR technique is applied on the segmented correction guard electrode (see section 2.4.4 for more details).

2.5.3 Ion motion in an ideal Penning trap

In order to understand how mass spectrometry using a Penning trap is performed, one first needs to study the ion motion in such traps. In this section we derive the equations of motion for a charged particle in a Penning trap. We present the different eigen motions and calculate the energy of charged particle in a Penning trap.

In the trap, the ions are affected by the force generated by the quadrupo-

2.5. The mass measurement Penning trap

lar electric field $\vec{E} = -\vec{\nabla}V$:

$$\vec{F}_e = -q\vec{\nabla}V = -\frac{qV_0}{d_0^2}(\vec{z} - \vec{r}/2) \quad (2.9)$$

and the force produced by the homogenous axial magnetic field $\vec{B} = B\hat{z}$:

$$\vec{F}_m = -q\vec{v} \times \vec{B} = -q\dot{\vec{r}} \times B\hat{z} \quad (2.10)$$

The dot denotes partial derivative in time. Since the magnetic field is along the z -axis, the magnetic component of the Lorentz force does not affect the axial ion motion.

There are several methods to derive the equation of motions inside a Penning trap [Kre91]. In this thesis, we use a Newtonian mechanical approach. Using Newton's second law on equation (2.9) and (2.10) in cylindrical coordinates, leads to the axial and radial equations of motion:

$$\ddot{z} = -\frac{qV_0}{Md_0^2}z \quad (2.11)$$

$$\ddot{\vec{r}} = \frac{qV_0}{2md_0^2}\vec{r} - \frac{qB}{M}\dot{\vec{r}} \times \hat{z}. \quad (2.12)$$

The first equation represents an axial harmonic motion of angular frequency:

$$\omega_z = \sqrt{\frac{qV_0}{Md_0^2}}, \quad (2.13)$$

produced by the potential difference V_0 . The second equation is more complex and in order to solve it, we write the radial part in cartesian coordinates:

$$\ddot{x} - \omega_c \dot{y} - \frac{\omega_z^2}{2}x = 0 \quad (2.14)$$

$$\ddot{y} + \omega_c \dot{x} - \frac{\omega_z^2}{2}y = 0, \quad (2.15)$$

where we used equation (2.13) and ω_c is the cyclotron frequency:

$$\omega_c = \frac{qB}{M}. \quad (2.16)$$

Using $u = x + iy$ decouples equation (2.14) and (2.15) and gives:

$$\ddot{u} = -i\omega_c \dot{u} + \frac{\omega_z^2}{2}u. \quad (2.17)$$

2.5. The mass measurement Penning trap

With the ansatz $u \propto e^{-i\omega_{\pm}t + \alpha_{\pm}}$, one finds the two radial eigenfrequencies

$$\omega_{\pm} = \frac{\omega_c}{2} \pm \frac{\omega_c}{2} \sqrt{1 - \frac{2\omega_z^2}{\omega_c^2}} \quad (2.18)$$

and the following parametric equations for $x(t)$ and $y(t)$

$$u(t) = r_+ e^{-i\omega_+ t} + r_- e^{-i\omega_- t} \quad (2.19)$$

$$x(t) = r_+ \cos(\omega_+ t) + r_- \cos(\omega_- t) \quad (2.20)$$

$$y(t) = -r_+ \sin(\omega_+ t) - r_- \sin(\omega_- t) \quad (2.21)$$

where we set the phases $\alpha_+ = \alpha_- = 0$ to simplify the expression. Equation (2.20)

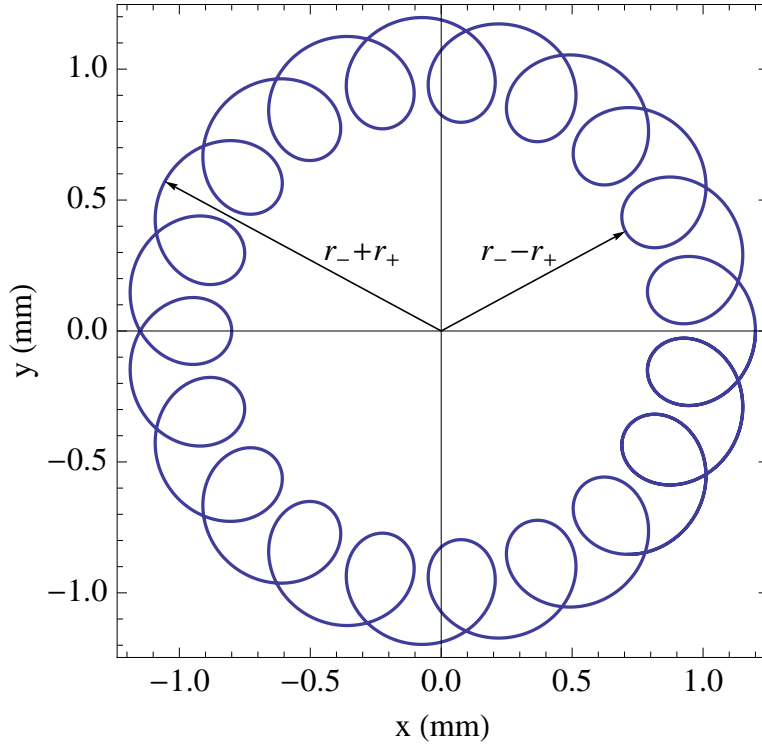


Figure 2.11: Example curve of the epitrochoid motion of an ion in a Penning trap, with parameters: $r_- = 1$ mm, $r_+ = 0.2$ mm, $\omega_- = 1$ s⁻¹ and $\omega_+ = 20$ s⁻¹. See text for details.

and (2.21) correspond to the parametrization of an epitrochoid. An example

2.5. The mass measurement Penning trap

ν_c	9.451 MHz
ν_+	9.445 MHz
ν_z	339 kHz
ν_-	6.1 kHz

Table 2.2: Different frequencies $\nu = \omega/2\pi$ for a ${}^6\text{Li}^+$ ion in TITAN's Penning trap.

curve is shown in figure 2.11 (note that the ω_{\pm} and r_{\pm} do not correspond to typical values for an ion in a Penning trap and were chosen for demonstration).

The angular frequencies ω_{\pm} obey the following relationships:

$$\omega_c = \omega_+ + \omega_- \quad (2.22)$$

$$\omega_c^2 = \omega_+^2 + \omega_-^2 + \omega_z^2 \quad (2.23)$$

$$\frac{\omega_z^2}{2} = \omega_+ \omega_- \quad (2.24)$$

Table 2.2 lists the various frequencies for a ${}^6\text{Li}^+$ ion in a Penning trap with a magnetic field of strength $B = 3.7\text{T}$, a potential difference $V_0 = 35\text{V}$ and a trap characteristic length $d_0 = 11.2\text{ mm}$. From the frequencies listed in table 2.2, we observe that $\frac{2\omega_z^2}{\omega_c^2} = 2.5 \times 10^{-3} \ll 1$. This fulfills the condition of a Taylor expansion of (2.18), which gives:

$$\omega_+ \simeq \omega_c - \frac{\omega_z^2}{2\omega_c} \quad (2.25)$$

$$\omega_- \simeq \frac{\omega_z^2}{2\omega_c}, \quad (2.26)$$

where ω_+ and ω_- are respectively the reduced cyclotron and magnetron frequencies. The reduced cyclotron frequency is a consequence of the repulsive radial electric potential that reduces the cyclotron frequency by a small amount ω_- . The magnetron frequency is a slow precession at the drift velocity \vec{v}_d caused by the cross product of the electric and magnetic fields:

$$\vec{v}_d = \frac{\vec{E} \times \vec{B}}{B^2} = \frac{\omega_z^2}{2\omega_c} \vec{r} \times \vec{z} = \omega_- \vec{r} \times \vec{z}. \quad (2.27)$$

The following quantities are the potential and kinetic energies of the

2.5. The mass measurement Penning trap

ion's radial motion in the Penning trap:

$$E_r^{pot} = qV = -\frac{M}{4}\omega_z^2 r^2 = -\frac{M}{2}\omega_-\omega_+ (r_+^2 + r_-^2 + 2r_+r_- \cos(\omega_c t)) \quad (2.28)$$

$$E_r^{kin} = \frac{m}{2}\dot{r}^2 = \frac{M}{2} (\omega_-^2 r_-^2 + \omega_+^2 r_+^2 + 2r_+r_- \omega_+\omega_- \cos((\omega_+ - \omega_-)t)). \quad (2.29)$$

Typically, the reduced cyclotron and magnetron frequencies of the ions are such that $\omega_-/\omega_+ \sim 10^{-3}$. Depending on the relative size of the magnetron and the reduced cyclotron radius, the ion energy in the radial plane is more or less potential or kinetic energy. Equations (2.28) and (2.29) shows that for a large magnetron radius ($r_- \gg r_+$), the ion energy is mainly potential. At the opposite, when the reduced cyclotron radius is larger ($r_- \ll r_+$) the ion energy is mainly kinetic. This is an important fact that is used in Penning trap mass measurement via time-of-flight ion cyclotron resonance (TOF-ICR) technique.

2.5.4 The TOF-ICR mass measurement technique

The basic concept of the TOF-ICR technique is to determine the mass of an ion by measuring its cyclotron frequency. However, the cyclotron frequency cannot be measured directly because it is not the frequency of one of the ion's eigenmotions. Nevertheless, access to the cyclotron frequency can be gained using a quadrupolar excitation of the ion motion of the form

$$V_{RF} = \frac{V_q}{2a^2} \cos(\omega_{RF} + \phi_{RF})xy, \quad (2.30)$$

where V_q is the amplitude of the RF at a radial distance a from the axis of the trap and ϕ_{RF} is the RF excitation phase. This RF excitation is applied to the segmented guard electrode, as shown in figure 2.10 (b).

This RF excitation couples the two radial eigenmotions. For a given RF amplitude and excitation time, the ion's motion will be fully converted from one eigenmotion to another if the excitation frequency corresponds to the cyclotron frequency. Therefore, the cyclotron frequency can be found through a determination of the excitation frequency for which the conversion between the two eigenmotions is complete. In the following, we explain how this is done using the TOF-ICR technique.

As mentioned, with the application of a quadrupole excitation, the magnetron and reduced cyclotron motions couple and their radii evolve as [Kon95]:

2.5. The mass measurement Penning trap

$$r^\pm(t) = \left\{ r^\pm(0) \cos(\omega_B t) \mp \left(\frac{r^\pm(0)i(\omega_{RF} - \omega_c) + r^\mp(0)k_0 e^{\pm i\Delta\phi}}{2\omega_B} \right) \sin(\omega_B t) \right\} e^{i(\omega_{RF} - \omega_c)t/2}, \quad (2.31)$$

where

$$\omega_B = \frac{1}{2} \sqrt{(\omega_{RF} - \omega_c)^2 + k_0^2}, \quad (2.32)$$

$$k_0 = \frac{V_q}{2a^2} \frac{q}{m} \frac{1}{\omega_+ - \omega_-}, \quad (2.33)$$

$$\Delta\phi = \phi_{RF} - \phi_+ - \phi_-. \quad (2.34)$$

When the RF field is applied at the cyclotron frequency, i.e. $\omega_{RF} = \omega_c$, equation (2.31) becomes:

$$r^\pm(t) = \left\{ r^\pm(0) \cos(k_0 t/2) \mp r^\mp(0) e^{\pm i\Delta\phi} \sin(k_0 t/2) \right\}. \quad (2.35)$$

If the initial condition is such that the ion is completely in the magnetron mode with radius $r^-(0) = r_0$, then both radii evolve in time as:

$$\frac{r^+(t)}{r_0} = \sin(k_0 t/2), \quad (2.36)$$

$$\frac{r^-(t)}{r_0} = \cos(k_0 t/2). \quad (2.37)$$

Figure 2.12 shows that a full conversion of the initial magnetron motion into reduced cyclotron occurs when the conversion factor η :

$$\eta = k_0 T_{RF} / \pi \quad (2.38)$$

is equal to $\eta = \eta_0 = 1, 3, 5, \dots$. At the beginning of the excitation ($\eta = 0$), the ion motion is purely magnetron. This means that the energy of the ion is dominantly potential energy. After a time $T_{RF} = \eta_0 \pi / k_0$, the situation is inverted and the motion is purely reduced cyclotron motion, leading to a full transfers of the potential energy into kinetic energy. Therefore, using equation (2.33) in order to have a full conversion from an initial magnetron motion into a reduced cyclotron motion, RF amplitude and the excitation time must satisfy:

$$V_{RF} \approx \frac{2\pi B a^2 \eta_0}{T_{RF}}. \quad (2.39)$$

2.5. The mass measurement Penning trap

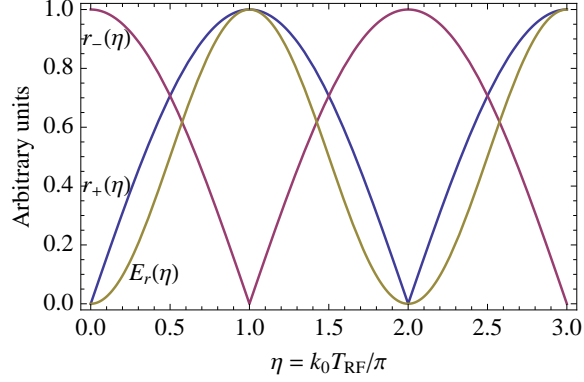


Figure 2.12: Evolution of the reduced cyclotron motion of radius r_+ , magnetron motion of radius r_- and radial kinetic energy as a function of the conversion factor $\eta = k_0 T_{RF}/\pi$.

If the applied RF frequency is detuned from the cyclotron frequency by the amount

$$\Delta\nu_{RF} = \frac{\omega_{RF} - \omega_c}{2\pi}, \quad (2.40)$$

the kinetic energy of the ion in the radial plane at the end of the conversion is given by

$$E_r = E_0 \frac{\sin^2 \left(\frac{\pi}{2} \sqrt{(2\Delta\nu_{RF} T_{RF})^2 + \eta^2} \right)}{(2\Delta\nu_{RF} T_{RF}/\eta)^2 + 1}. \quad (2.41)$$

Figure 2.13 shows that the ions which are resonantly excited ($\Delta\nu_{RF} = 0$) have maximum kinetic energy after the conversion. This means that the cyclotron frequency ν_c of the ion can be determined by taking the kinetic energy as a measure of achieving resonant conditions, hence when the excitation frequency ν_{RF} maximizes the kinetic energy of the ion. Note that the full width half maximum (FWHM) of the time-of-flight spectra is given by $\Delta\nu \cdot T_{RF} \approx 0.8$ for $\eta = 1$ and $\Delta\nu \cdot T_{RF} \approx 1.6$ for $\eta = 3$. This means that the resonance width for a full conversion is minimal when the conversion factor $\eta = 1$. Therefore, for a given excitation time T_{RF} , the smallest FWHM of a kinetic energy spectra is given by

$$\Delta\nu = \frac{0.8}{T_{RF}}. \quad (2.42)$$

A change in the ion kinetic energy during application of an RF-field with $\Delta\nu_{RF}$ is measured by ejecting the ions from the trap through a hole in

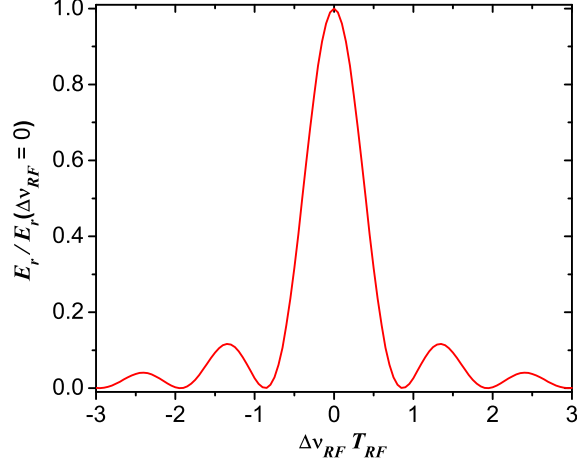


Figure 2.13: Change in the kinetic energy in the radial plane as a function of the detuning $\Delta\nu_{RF}$.

the end cap electrode (see figure 2.10 (a)). Then the change in time-of-flight taken by the ion to reach a micro-channel plate (MCP) detector is measured.

After extraction from the trap, as the ion approaches the detector (see top of figure 2.14) and travel in the fringe field produced by the magnet, the change in direction of the magnetic field applies a torque on their initial magnetic moment:

$$\vec{\mu}(\omega_{RF}) = \frac{E_r(\omega_{RF})}{B_0} \hat{z}. \quad (2.43)$$

The resulting work applied to the ions is expressed as

$$W = -\mu(\omega_{RF}) \cdot B_z(z). \quad (2.44)$$

It results in a conversion of the kinetic energy gained from the radial motion into an axial acceleration. Figure 2.14 is a simulation result which illustrates the proportionality between the kinetic energy in the radial motion and the axial magnetic field strength. From equation (2.43) and (2.44), one sees that the ions which are excited at the frequency $\nu_{RF} = \nu_c$ have the largest kinetic energy gain and thus have the shortest time-of-flight. Hence it is possible to find the cyclotron frequency by scanning through the excitation frequency and finding which ν_{RF} leads to a minimal time-of-flight.

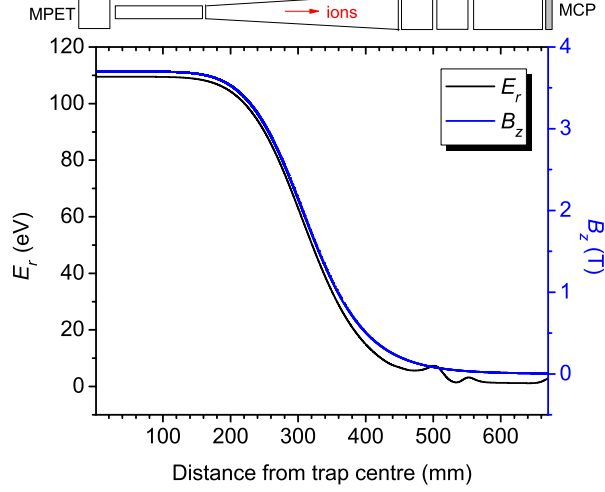


Figure 2.14: Axial B_z magnetic field strength and kinetic energy related to the radial motion E_r as a function of the distance from the trap centre. Shown on top is a schematic of the ion optics between the trap and MCP detector.

In a typical cyclotron frequency measurement, the ions are excited at a fixed frequency ν_{RF} for a given time and then released from the trap. The time-of-flight of the ions from the trap to the MCP detector is recorded. This procedure is repeated while varying ν_{RF} within the vicinity of the expected ν_c and the TOF spectrum is obtained (figure 2.15). The cyclotron frequency is determined by fitting the expected line shape to the spectrum. The following analytical expression for the TOF [Kon95]:

$$T(\nu_{RF}) = \int_{z_0}^{z_1} \left\{ \frac{M}{2 \cdot [E_0 - q \cdot V(z) - \mu(\nu_{RF}) \cdot B(z)]} \right\}^{1/2} dz \quad (2.45)$$

is used to describe the line shape.

2.5.5 The mass determination

The mass m of the trapped ion is determined from the measurement of its cyclotron frequency ν_c :

$$M = \frac{1}{2\pi} \frac{qB}{\nu_c}. \quad (2.46)$$

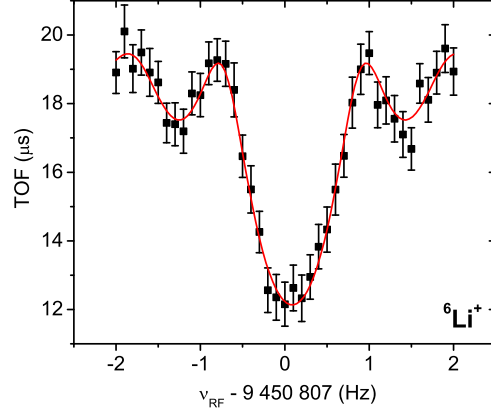


Figure 2.15: ${}^6\text{Li}^+$ cyclotron frequency resonance taken with a 997 ms excitation time. The solid line is a fit of the theoretical line shape [Kon95] to the data.

The value of ion's charge state q and the magnetic field B needs to be determined. Since all the measurements presented in this thesis were done using singly charged ions, we only consider the case where q equals to one in units of the elementary charge.

Figure 2.15 shows that the magnetic field strength B during the measurement of ν_c is determined by a linear interpolation between two measured cyclotron frequency of a calibration ion species:

$$B = \frac{M_{cal}}{q_{cal}} \nu_{c,inter} \quad (2.47)$$

where $\nu_{c,inter}$ is the interpolated cyclotron frequency, M_{cal} is the calibration ion's mass and q_{cal} equals one elementary charge. The choice of the calibrant relies on two factors: its cyclotron frequency needs to be close to the cyclotron frequency of the ion of interest and in order to not limit the precision, the calibration mass, M_{cal} should be more precisely known than the precision aimed for in the measurement.

A frequency ratio R is derived from each frequency ($\nu_{c,inter}$, ν_c) pair:

$$R = \nu_{c,inter} / \nu_c. \quad (2.48)$$

The mean frequency ratio \bar{R} is calculated by taking the weighted mean of all

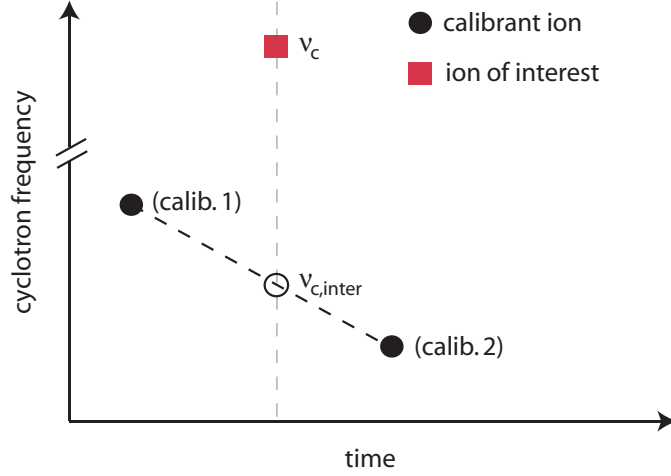


Figure 2.16: Linear interpolation of the calibration cyclotron frequency at the moment the cyclotron frequency of the ion of interest was measured.

R . The frequency ratio involves ion masses, while the quantity of interest is the (neutral) atomic mass. Hence, one has to take into account the electron's mass and binding energy. The atomic mass of interest m is then determined by:

$$m = \bar{R} \cdot (m_{cal} - m_e + B_{e,cal}) + m_e - B_e, \quad (2.49)$$

where $B_{e,cal}$ and B_e are the first ionization energies of the calibrant and the ion of interest respectively and m_e is the electron mass.

The resolving power \mathcal{R} in Penning trap mass spectrometry is given by [Bol01]:

$$\mathcal{R} = \frac{\nu_c}{\delta\nu} = 1.25 \cdot \nu_c \cdot T_{RF}, \quad (2.50)$$

where we used equation (2.42) to replace $\delta\nu$. The statistical relative uncertainty of a mass measurement is inverse proportional to the resolving power and to the square root of the number of detected ions N_{ion} [Bol01]:

$$\frac{\delta m}{m} \approx \frac{1}{\mathcal{R}} \frac{1}{\sqrt{N_{ion}}} = \frac{1.6 \cdot \pi \cdot m}{q \cdot B \cdot T_{RF} \cdot \sqrt{N_{ion}}}. \quad (2.51)$$

This relation shows that the precision on the measured mass can be improved in several ways. By increasing the excitation time T_{RF} , with a magnet having a higher magnetic field, or by increasing the charge state of the ion. For stable ions, we can increase T_{RF} to improve the precision. However, the

2.5. *The mass measurement Penning trap*

half-life of the measured species limits the excitation time, which limits the excitation time that can be used.

The precision on the mass measurement can be further improved by using a magnet with higher field strength. However, only an increase in the precision of a factor of two or three would be possible as higher field magnets have not yet been developed with the required homogeneity and stability. An other option is to increase the charge state q of the ion. This allows a precision gain proportional to the charge state used. This method is employed at the TITAN experiment as described in section 2.1.2. However, it was not used in any of the measurements presented in this thesis as the required level of precision was already reached using singly charged ions.

Chapter 3

Systematic studies of the TITAN Penning trap and data analysis

A real Penning trap is not as ideal as it is presented in section 2.4 and modification arise from a number of factors. For instance, the electrodes forming the trap do not extend to infinity and are truncated. Also, holes in the two end caps electrodes have to be made in order to inject and extract the ions from the trap. Moreover, the ideal trap assumes perfect geometrical alignment of all fields. In reality misalignment between each trap electrode and distortion in the shape of the electrodes affects the trapping potential. There are also misalignments of the trap principal axis with the magnetic field axis, and deviation from homogeneity of the magnetic field in the trapping region. Other effects due to the Coulomb interaction between ions, time fluctuations of the magnetic field and relativistic effects have to be taken into account.

This chapter discusses the effects of these factors on the accuracy of the frequency measurements used for the mass determination. These limitations in the accuracy are caused by the change (or shift) in cyclotron frequency due to the several effects that were enumerated above. Some of these shifts can be minimized through a so-called compensation of the Penning trap potential and the compensation of TITAN's Penning trap will be presented. At the end of this chapter we present the mass measurement of stable ${}^6\text{Li}$. This is a benchmark measurement regarding the level of precision and accuracy that can be achieved with the TITAN Penning trap mass spectrometer.

3.1 Frequency ratio deviation for a real Penning trap

The imperfection in the trapping potential, magnetic field and trap structure as well as the Coulomb interaction between ions, the time fluctuations of

3.2. Trapping potentials of a real Penning trap and trap-related systematic error

the magnetic field, and relativistic effects all result in a different measured cyclotron frequency than the true ν_c given by equation (2.46). These so-called frequency shifts then modify the measured frequency ratio $R_{meas.}$:

$$R_{meas.} = \frac{\nu_{c,1} + \Delta\nu_{c,1}}{\nu_{c,2} + \Delta\nu_{c,2}} \quad (3.1)$$

from the ideal frequency ratio

$$R_{ideal} = \frac{\nu_{c,1}}{\nu_{c,2}}. \quad (3.2)$$

The large value of the cyclotron frequency, in the MHz range, compared to the frequency shifts $\Delta\nu_c$, in the Hz range, allows one to state that $\Delta\nu_c/\nu_c \ll 1$. This consequently leads to a relative frequency ratio shift of

$$\frac{\Delta R}{R} = \frac{R_{meas.} - R_{ideal}}{R_{ideal}} = \frac{\Delta\nu_{c,1}}{\nu_{c,1}} - \frac{\Delta\nu_{c,2}}{\nu_{c,2}}. \quad (3.3)$$

Equation (3.3) indicates two points: first, the error of relative frequency ratio shift is in general smaller than the individual relative frequency shifts. Secondly, by measuring the frequency ratio of two species of similar ν_c , one can reduce $\Delta R/R$ by several order of magnitude. The following sections investigate the various sources of frequency shifts and estimate their size in detail.

3.2 Trapping potentials of a real Penning trap and trap-related systematic error

The first step to determine the effects of the trapping potential imperfections on the cyclotron frequency consists of deriving the potential of a realistic Penning trap. This is done by starting from the most general potential and identifying the parts of the potential that will affect the cyclotron frequency.

The most general expression for an electrical trapping potential is obtained by solving the Laplace equation in spherical coordinates. The resulting potential is

$$V(\rho, \theta, \phi) = \sum_{l=0}^{\infty} \sum_{m=-l}^l A_{l,m} \cdot \rho^l \cdot Y_l^m(\theta, \phi) \quad (3.4)$$

where (ρ, θ, ϕ) are the spherical coordinates and $Y_l^m(\theta, \phi)$ are spherical harmonics. The first term of the series (3.4), which is $l = 0$, represents a

3.2. Trapping potentials of a real Penning trap and trap-related systematic error

constant offset of the trapping potential compared to the ground potential. This term does not produce any electric field and therefore it does not modify the ions equation of motion, leaving the cyclotron frequency unaffected.

The next term, $l = 1$, is proportional to ρ and represents a constant electric field in the trap. This results in the addition of a constant term to the solution of the equation of motion, which does not modify the ion motion or shift the cyclotron frequency. Furthermore, Penning traps are symmetric under inversion $\vec{r} \rightarrow -\vec{r}$ (at the condition that the end cap and ring electrode symmetry axis cross at the centre of the trap), hence the $l = 1$ term is relatively small compared to the quadratic term. Therefore, the higher order of $l = \text{odd}$ numbers are negligible and we only consider the contributions of $l = \text{even}$ numbers to the series of equation (3.4).

The inclusion of $m \neq 0$ terms in the quadratic trapping potential ($l = 2$) induces an extra quadrupolar field in the xy-plane:

$$V_2(x, y, z) = \frac{V_0}{2d^2} \left\{ z^2 - \frac{1}{2} (x^2 + y^2) - \frac{\epsilon}{2} (x^2 - y^2) \right\}. \quad (3.5)$$

The size of the extra field is given by the asymmetry parameter ϵ . The effect of ϵ on the measured cyclotron frequency and the factors causing this asymmetry are discussed in detail in the section 3.2.2.1. For $l > 2$, we assume $m = 0$ because $|m| \geq 1$ represents a smaller perturbation of the trapping potential, hence their contribution to equation (3.4) is negligible.

The $l > 2$ terms of equation (3.4) are caused by the holes in the end cap electrodes and by the truncation of the Penning trap hyperboloid structure. The octupole ($l = 4$) and dodecapole ($l = 6$) terms [Bol90] of equation (3.4) are:

$$V_4(r, z) = C_4 \left(\frac{V_0}{2d^4} \right) \left\{ z^4 - 3z^2r^2 + \frac{3}{8}r^4 \right\} \quad (3.6)$$

$$V_6(r, z) = C_6 \left(\frac{V_0}{2d^6} \right) \left\{ z^6 - \frac{15}{2}z^4r^2 + \frac{45}{8}z^2r^4 - \frac{5}{16}r^6 \right\}. \quad (3.7)$$

Because of the $1/d^l$ dependence of the potential, the contribution of the $l > 8$ terms to equation (3.4) are increasingly smaller.

In section 3.2.3, we show that the frequency shifts arising from the non-harmonic terms in the trapping potential can produce relative frequency ratio shifts in the order of $\Delta R/R \sim 10^{-7}$, which is above the required level of precision that the TITAN mass spectrometer aims at. However, these shifts can be reduced by factors of over 100 by adjusting the potential of the correction electrodes. The contribution caused by the holes in the end caps

3.2. Trapping potentials of a real Penning trap and trap-related systematic error

are corrected for by the addition of two correction tube electrodes (label (3) in figure 2.10) before the two end caps. The distortion from the truncation of the hyperbola forming the trap electrodes is minimized by adding two sets of correction guard electrodes (label (4) in figure 2.10) between the ring and end caps electrodes. The adjustment of the potential of these correction electrode is called trap compensation and the TITAN Penning trap compensation is discussed in detail in section 3.3.

3.2.1 Penning trap magnetic field inhomogeneities

The ideal Penning trap assumes that the magnetic field is constant throughout the trapping region, i.e. $B(x, y, z) = B_0 = \text{constant}$. For real traps, however, magnetic field inhomogeneities are created by the finite size of the solenoid and the magnetic field distortion due to the magnetic susceptibilities of the trap material [Bol90]. For both cases, the lowest-order contribution to the magnetic field inhomogeneities is

$$\Delta B = B_0 \{1 + \beta_2 (z^2 - r^2/2)\} \quad (3.8)$$

where B_0 is the unperturbed magnetic field and β_2 is a material constant. As an example, β_2 is found in other systems to be $-1.7 \times 10^{-7} \text{ mm}^{-2}$ for ISOLTRAP [Bol90] and $1.3 \times 10^{-10} \text{ mm}^{-2}$ for LEBIT [Rin09b]. The frequency shift from the field inhomogeneity (3.8) is:

$$\Delta\omega_c = \beta_2\omega_c \left\{ z^2 - \frac{r_+^2}{2} \left(1 - \frac{\omega_c}{\omega_+ - \omega_-} \right) - \frac{r_-^2}{2} \left(1 + \frac{\omega_c}{\omega_+ - \omega_-} \right) \right\}. \quad (3.9)$$

Typically $\omega_+ \gg \omega_-$ and using $\omega_c = \omega_+ + \omega_-$, equation (3.9) is simplified as

$$\Delta\omega_c = \beta_2\omega_c \left\{ (z^2 - r_+^2) - \frac{\omega_-}{\omega_c} (r_+^2 + r_-^2) \right\}. \quad (3.10)$$

Because $\omega_c \gg \omega_-$, the term in curly brackets is very weakly mass dependant. This is because the magnetron frequency is very weakly mass-dependent. For a $V_0 = 36 \text{ V}$ trapping potential, the change in magnetron frequency with the mass number (u) is 0.65 Hz/u . This corresponds to a relative change in the magnetron frequency of $10^{-4}/u$ resulting in a change in the ratio ω_-/ω_c in the range of $10^{-10}/u$. This can be considered as nearly mass-independent. The overall effect on the cyclotron frequency ratio is:

$$\left(\frac{\Delta R}{R} \right)_{mag.inhom.} \simeq -\beta_2 (r_+^2 + r_-^2) \frac{\nu_- (A - A_{cal.})}{\nu_c A}. \quad (3.11)$$

3.2. Trapping potentials of a real Penning trap and trap-related systematic error

Using typical values of $(r_+^2 + r_-^2) = 1 \text{ mm}^2$, $\nu_- = 6100 \text{ Hz}$ and assuming a conservative $\beta_2 = -1.7 \times 10^{-7} \text{ mm}^{-2}$, we get a shift in the frequency ratio of $(\Delta R/R)_{\text{mag.inhom.}} < 1.8 \times 10^{-11} \cdot \Delta A$, where $\Delta A = A - A_{\text{cal.}}$. This is two orders of magnitude below the standard precision obtained with the TITAN Penning trap. Therefore, additional optimization of the magnetic field is not required at this point.

3.2.2 Harmonic distortion and misalignment of the magnetic field axis

The ideal Penning trap assumes a perfect alignment between the trap and magnetic field axis (i.e. $\vec{B} = B_0 \hat{z}$) as shown in figure 2.10. It also assumes that the electrodes are perfectly aligned with respect to each other and without surface imperfections. In reality, as Figure 3.1 (a) shows, the

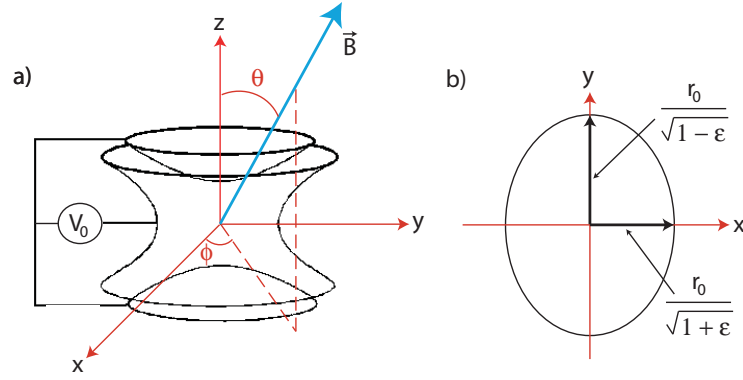


Figure 3.1: a) Schematic of the electrode structure alignment with the magnetic field axis. b) Top view of an elliptically distorted ring electrode that leads to a non-zero asymmetry parameter ϵ .

magnetic field might have some misalignment with the trap axis which can be expressed as

$$\vec{B} = B_0 (\sin \theta \cos \phi \hat{x} + \sin \theta \sin \phi \hat{y} + \cos \theta \hat{z}). \quad (3.12)$$

Also, the trap electrodes could have deformations as shown in figure 3.1 (b), as well as be misaligned with respect to each other that leads to a non-zero asymmetry parameter ϵ . This results in a distorted potential given by equation (3.5).

3.2. Trapping potentials of a real Penning trap and trap-related systematic error

These two imperfections modify the equation of motion of the ion in the Penning trap (2.11) according to:

$$\ddot{x} - \frac{\omega_z^2}{2}(1 + \epsilon)x - \omega_c(\cos\theta\dot{y} - \sin\theta\sin\phi\dot{z}) = 0 \quad (3.13)$$

$$\ddot{y} - \frac{\omega_z^2}{2}(1 - \epsilon)y + \omega_c(\cos\theta\dot{x} - \sin\theta\cos\phi\dot{z}) = 0 \quad (3.14)$$

$$\ddot{z} + \omega_z^2 z - \omega_c\sin\theta(\sin\phi\dot{x} - \cos\phi\dot{y}) = 0. \quad (3.15)$$

Assuming $x(t) \sim e^{-i\omega t}$, equations (3.13) to (3.15) become a system of linear equations. Applying linear algebra techniques it results in imperfect trap eigenfrequencies ($\bar{\omega}_i$) which depend on (ϵ, θ, ϕ) and a shifted cyclotron frequency given by

$$\Delta\bar{\omega}_c = \bar{\omega}_c - \omega_c. \quad (3.16)$$

A result obtained from solving equations (3.13) to (3.15) is the so-called invariance theorem [Bro82]:

$$\omega_c^2 = \bar{\omega}_z^2 + \bar{\omega}_+^2 + \bar{\omega}_-^2. \quad (3.17)$$

This theorem states that the sum of the squared real trap eigenfrequencies are independent of (θ, ϕ, ϵ) and are equal to the ideal trap cyclotron frequency. Typically, $\omega_+ \gg \omega_z \gg \omega_-$, which changes (3.17) as:

$$\omega_c \simeq \bar{\omega}_+ \left(1 + \frac{1}{2} \frac{\bar{\omega}_z^2}{\bar{\omega}_+^2} \right). \quad (3.18)$$

For small angles and asymmetry parameter ϵ the real trap magnetron frequency $\bar{\omega}_-$ [Bro82] is:

$$\bar{\omega}_- \simeq \frac{1}{2} \frac{\bar{\omega}_z^2}{\bar{\omega}_c^2} \left(1 + \frac{9}{4}\theta^2 - \frac{1}{2}\epsilon^2 \right). \quad (3.19)$$

Combining (3.18) and (3.19) and applying $\bar{\omega}_c = \bar{\omega}_+ + \bar{\omega}_-$ the cyclotron frequency shift (3.17) becomes

$$\Delta\bar{\omega}_c = \bar{\omega}_- \left(\frac{9}{4}\theta^2 - \frac{1}{2}\epsilon^2 \right). \quad (3.20)$$

The corresponding shift in the frequency ratio is given by

$$(\Delta R/R)_{mis.} = \left(\frac{9}{4}\theta^2 - \frac{1}{2}\epsilon^2 \right) \cdot \left(\frac{\Delta A}{A_{cal.}} \right) \cdot \left(\frac{\bar{\nu}_-}{\bar{\nu}_{+,cal.}} \right). \quad (3.21)$$

3.2. Trapping potentials of a real Penning trap and trap-related systematic error

In order to estimate the size of the frequency shifts due to the misalignment with the magnetic field and the harmonic distortion, we use the magnetron frequency for TITAN's Penning trap ($\nu_- = 6100$ Hz) and by approximating $\nu_+ \simeq \nu_c$. This results in a shift of $(\Delta R/R)_{mis.} = (\frac{9}{4}\theta^2 - \frac{1}{2}\epsilon^2) \cdot \Delta A \cdot 1.1 \times 10^{-4}$. In order to have a conservative estimate on the error, we use the conservative values for $\theta = \epsilon = 0.01$ from [Bol90]. By doing so, we get a shift in the range of $(\Delta R/R)_{mis.} = 10^{-8}$ when ions with different atomic masses are used. Such a shift is greater than the precision level at which the TITAN Penning trap aims. Therefore it is crucial to estimate and measure θ and ϵ for the TITAN Penning trap and minimize its impact.

3.2.2.1 Harmonic distortion of the electrical potential in the Penning trap

Here we estimate the size of the asymmetry parameter ϵ based on the machining tolerances of the electrodes and we measure its size by creating an artificial harmonic distortion using the correction guard electrode.

To study the effect of the asymmetry parameter ϵ on the electrical potential, we re-write the radial part of (3.5) as

$$V_{harm.dist.} = \frac{V_0}{4d_0^2} \{(1 + \epsilon)x^2 + (1 - \epsilon)y^2\}. \quad (3.22)$$

Depending on the value for ϵ the equipotential lines may form three different shapes. For $\epsilon = 0$ the lines are circular. This is the case for an ideal trap. For $0 < \epsilon < 1$ the radial equipotential lines are in an elliptical shape. For $\epsilon > 1$ the equipotentials are hyperbolic with a saddle point at the trap centre. This last case leads to unstable solutions for the ion motion. As ϵ is typically < 0.1 [Bol90], we are not considering this last case. Please refer to [Kre08] for a detailed explanation.

A non-zero asymmetry parameter, ϵ , is caused by a number of effects. We discuss them and show how they can be minimized. Patched oxidation of the electrodes surfaces cause undesired stray electric fields [Tes97], which modify the electric potential. Such effects are minimized by gold-plating the trap electrode surfaces (see figure 3.2). In addition, quadrupole deformation of the electric potential in the xy-plane is minimized by applying an RF-field on the correction guard electrode to avoid splitting the ring electrode. Thirdly, the misalignment of the ring electrode with respect to the trap axis is minimized by using high-tolerance sapphire spheres (tolerance on the sphericity of $2.5 \mu\text{m}$) on which the trap electrodes sit and by applying tight electrode machining tolerance (typical tolerance of $10 \mu\text{m}$ in the dimensions).

3.2. *Trapping potentials of a real Penning trap and trap-related systematic error*

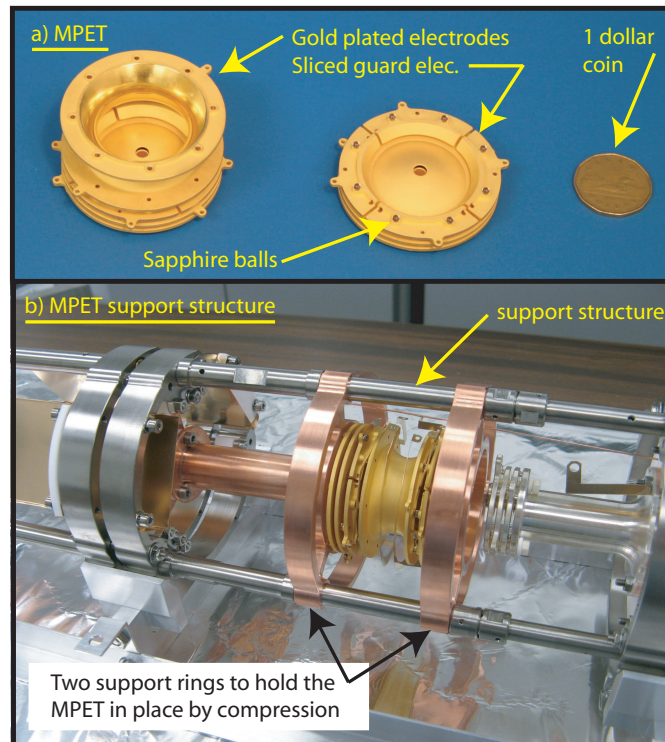


Figure 3.2: a) Left: one-piece ring electrode. Right: gold-plated Penning trap electrodes including the sapphire spheres (shown on top of the sliced guard electrode). Shown is a Canadian 1 dollar coin for scaling. b) The TITAN Penning trap placed in the support structure frame. The trap structure is held in place by compression using two support rings.

3.2. Trapping potentials of a real Penning trap and trap-related systematic error

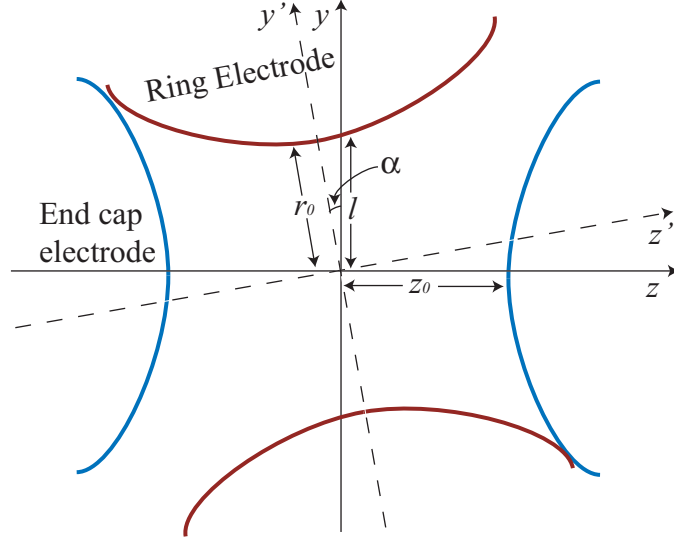


Figure 3.3: Exaggerated schematic of the tilted ring electrode that may be caused by uneven spacing between the ring and the end cap electrodes.

The Penning trap electrodes are isolated from one another using sapphire spheres placed in a groove on the surface of the electrode. The whole trap structure is then held in place by compression between two copper rings as shown in figure 3.2. Therefore, a non-zero tilting angle α (see figure 3.3) may be caused by uneven groove size where the sapphire balls sit on the opposite side of the ring electrode. Based on the design drawings, and standard machining tolerances, the maximum value for α is 0.0016 radians. Applying trigonometry and the equation for the ring electrode hyperbola, the asymmetry parameter ϵ due to tilted ring electrode is

$$\epsilon_{tilt} = \sin^2 \alpha \cdot (1 + (r_0/z_0)^2) = 1.1 \times 10^{-5}. \quad (3.23)$$

Lastly, we consider the case of an elliptical ring electrode (see figure 3.1), which is described by:

$$\frac{x^2}{(r_0/\sqrt{1+\epsilon})^2} + \frac{y^2}{(r_0/\sqrt{1-\epsilon})^2} = 1. \quad (3.24)$$

Assuming the ring electrode radius from the trap centre $r_0 = 15$ mm, and the machining tolerance $\delta = 0.01$ mm, we get

$$\epsilon_{max} = \frac{4\delta}{r_0} = 2.6 \times 10^{-3}, \quad (3.25)$$

3.2. Trapping potentials of a real Penning trap and trap-related systematic error

where we used twice the machining tolerance. This result is about four times smaller than the estimate in [Bol90], which is $\epsilon = 0.01$.

In the following, the value of ϵ for the TITAN Penning trap has been determined experimentally. According to [Gab09], the measured cyclotron frequency $\bar{\nu}_c$ is shifted from the ideal trap cyclotron frequency ν_c by

$$\bar{\nu}_c = \nu_c + \bar{\nu}_- \cdot \left(\frac{9}{4}\theta^2 - \frac{1}{2}\epsilon^2 \right). \quad (3.26)$$

This suggests that the measured cyclotron frequency shifts quadratically with ϵ . Therefore, by varying the amplitude V_{quad} of a constant quadrupolar potential

$$V = \frac{V_{quad}}{4a^2} (x^2 - y^2) \quad (3.27)$$

applied on segmented guard electrodes one can artificially change the value of ϵ . We then obtain a quadratic change in $\bar{\nu}_c$,

$$\bar{\nu}_c = \bar{\nu}_{c,max} + A \cdot (V_{quad} - V_{quad,max})^2 \quad (3.28)$$

where A , $\bar{\nu}_{c,max}$ and $V_{quad,max}$ are fitting parameters. Figure 3.4 shows the observed variation in $\bar{\nu}_c$ with V_{quad} together with a fit of (3.28). The

Parameter	Value
$\bar{\nu}_{c,max}$	1 458 879.50(1) Hz
A	0.0425(7) Hz V ⁻²
$V_{quad,max}$	-0.08(5) V

Table 3.1: Fitting parameters from (3.28) describing the quadratic change in $\bar{\nu}_c$ with the amplitude V_{quad} .

observed parameters are shown in table 3.1. They show that a small voltage of -0.08(5) V, for a trapping potential of $V_0 = 36$ V would be needed to fully cancel the asymmetry parameter ϵ_0 of the TITAN Penning trap. Using (3.26) and (3.28), ϵ_0 is calculated to be

$$\epsilon_0 = \sqrt{\frac{2A}{\bar{\nu}_-}} \cdot V_{quad,max} = 3(2) \times 10^{-4}. \quad (3.29)$$

Taking the upper error on ϵ_0 gives a contribution of $(\Delta R/R)_\epsilon = 1.3 \times 10^{-11} \cdot \Delta A$.

3.2. Trapping potentials of a real Penning trap and trap-related systematic error

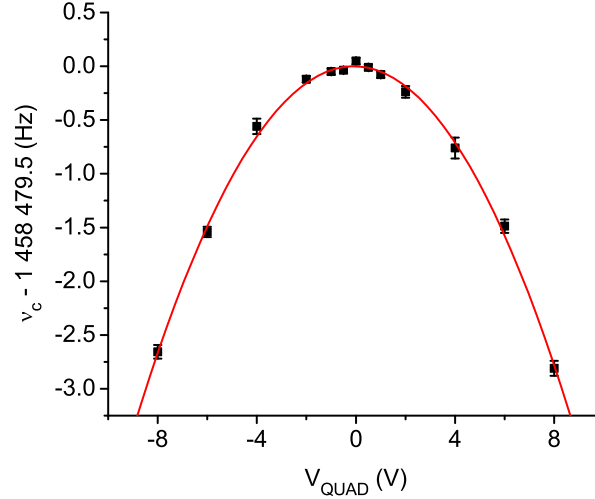


Figure 3.4: Variation of the measured cyclotron frequency $\bar{\nu}_c$ with the amplitude V_{quad} of a constant quadrupolar field applied on the correction guard electrode.

3.2.2.2 Misalignment of the magnetic field axis with the Penning trap electrode geometry

The misalignment between the Penning trap electrode axis and the axial direction of the magnetic field modifies the cyclotron frequency compared to the case where the field would be perfectly aligned. This change in frequency leads to a shift in the frequency ratio as expressed by equation (3.21) and explained in section 3.2.2. As this effect could limit the accuracy on the frequency ratio determination, it needs to be minimized. The angle of misalignment θ can be minimized by a precise alignment of the Penning trap structure with the magnetic field using an electron beam and also by requiring tight machining tolerances for the trap electrodes. In this section we discuss the error from both the alignment of the chamber with the magnetic field and the alignment of the trap with respect to the vacuum chamber. But first, we give a brief description of the vacuum chamber alignment procedure.

The trap vacuum chamber has been carefully aligned using an electron beam. For the alignment we used an electron source positioned at the trap

3.2. Trapping potentials of a real Penning trap and trap-related systematic error

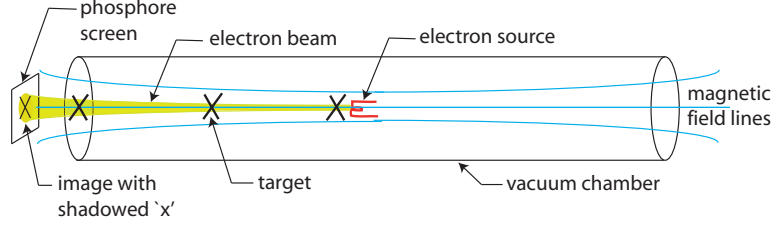


Figure 3.5: Schematic of the Penning trap vacuum chamber alignment using an electron source.

centre, a phosphor screen placed at the end of the vacuum chamber and three co-centric targets as shown in figure 3.5. The targets are made of an aperture with two metal stripes forming a co-centric “x” to the hole.

In the magnetic field, the electrons are guided along the field lines. Therefore, the chamber is pre-aligned once it is put in a position that allows the electron beam to pass through the three apertures. A fine alignment is then done by having the shadows of the three “x”s aligned on the phosphor screen. The alignment is done by moving the chamber in the x-y direction using an external mechanical alignment mechanism.

The chamber has been finely adjusted until a displacement with an upper error of 0.04 mm between the two most separated targets has been reached. Considering that the distance between these two aperture is 590.5(1) mm, this gives an upper limit on the misalignment of the vacuum chamber with respect to the magnetic field of $\theta_{chamber} < 7.3 \times 10^{-5}$ rad.

An additional source of error comes from a misalignment of the trap with respect to the support frame. As described in the previous section, the Penning trap electrodes are isolated from each other and from the support frame using sapphire spheres that are placed on a groove on the electrode surface. The whole structure is then held in place by compression (see figure 3.2) and this support structure is connected to the vacuum tube. The maximal misalignment of the trap with respect to the support structure happens when the support-giving sapphire balls are too wide, while the holes in which they are located are made too small. This combination with extreme opposites on either side of the electrode structure, as shown in figure 3.6, would lead to a maximal disturbance.

We consider sphericity tolerances on the sapphire balls of 2.5 μm and tolerances of 10 μm for the groove in which the balls are placed. In the worse case both the tube electrode with respect to the support and the end cap

3.2. Trapping potentials of a real Penning trap and trap-related systematic error

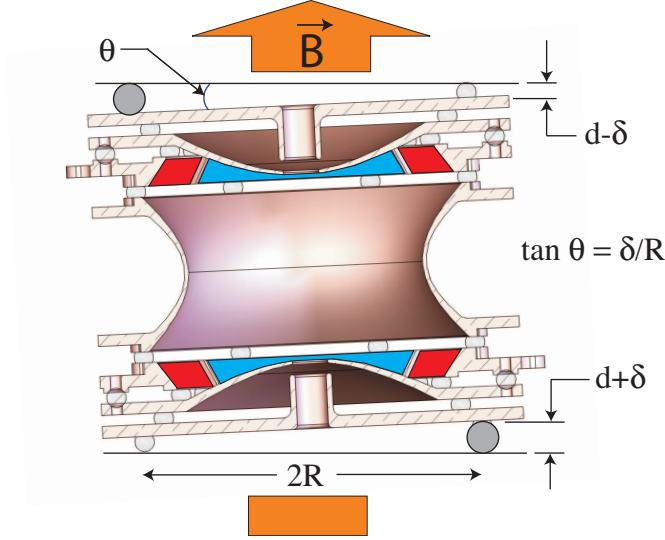


Figure 3.6: Unequal sapphire sphere and holding hole size leading to a trap axis misalignment with the magnetic field axis.

with respect to the tube electrode are misaligned. Under these conditions, the misalignment is $\delta = 90 \mu\text{m}$, where, to be conservative, we used double the machining tolerances. Considering that the support sphere are placed along a circle of radius $R = 21.6 \text{ mm}$, the largest possible tilt is

$$\theta_{supp.} = \delta/R = 4 \times 10^{-3}. \quad (3.30)$$

Since the error coming from the machining tolerances dominates ($\theta_{supp.} \gg \theta_{chamber}$) the error from the chamber alignment, the upper value on theta is $\theta_{max} = 4 \times 10^{-3}$. The error on the frequency ratio due to both the asymmetry parameter ϵ and the angle θ is given by equation (3.21). The maximal error on the frequency ratio is obtained when $\epsilon = 0$ and $\theta = 4 \times 10^{-3}$ and is equal to $(\Delta R/R)_{mis.} = 4.2 \times 10^{-9} \cdot \Delta A$. This value is for a trapping potential of $V_0 = 35 \text{ V}$. When a smaller trapping potential is used, the magnetron frequency

$$\nu_- \approx \frac{V_0}{4\pi d_0^2 B} \quad (3.31)$$

is reduced. As $(\Delta R/R)_{mis.} \propto \nu_-$, this leads to a smaller uncertainty due to the misalignment and harmonic distortion. For the ${}^6,8\text{He}$ mass measurements, the trapping potential was $V_0 = 3.6 \text{ V}$, which leads to $(\Delta R/R)_{mis.} = 0.4 \times 10^{-9} \cdot \Delta A$.

3.2.3 Non-harmonic imperfections of the trapping potential

The non-harmonic imperfections of the trapping potential are caused by the finite size of the trap and the holes in the end-cap electrodes. These imperfections cause shifts in the trap eigenfrequencies (ν_z, ν_-, ν_+) and consequently in the cyclotron frequency ($\nu_c = \nu_+ + \nu_-$). The procedure to calculate these frequency shifts is given in detail in [Bro86] and [Bol90]. In this section we only provide the results of these calculations. The shifts in the radial eigenfrequency for the octupole (C_4) and dodecapole (C_6) terms are

$$\delta\nu_{\pm} \approx \pm \frac{3}{4} \frac{C_4}{d^2} \nu_- \{ (r_{\pm}^2 + 2r_{\mp}^2) - 2z^2 \} \quad (3.32)$$

$$\delta\nu_{\pm} \approx \pm \frac{15}{16} \frac{C_6}{d^4} \nu_- \{ -3z^4 + 6z^2(r_{\pm}^2 + 2r_{\mp}^2) - (r_{\pm}^4 + 3r_{\mp}^4 + 6r_{\mp}^2 r_{\pm}^2) \}, \quad (3.33)$$

where the frequency shifts are almost mass independent. This is because the magnetron frequency is very weakly mass-dependent. Substituting $\nu_c = \nu_+ + \nu_-$, it gives

$$\begin{aligned} \delta\nu_c \approx & \frac{3}{4} \frac{(r_-^2 - r_+^2)}{d^2} \nu_- \{ C_4 + \frac{5}{2} \frac{C_6}{d^2} (3z^2 - r_+^2 - r_-^2) + \\ & + \frac{35}{8} \frac{C_8}{d^4} (r_+^4 + 3r_+^2 r_-^2 + r_-^4 - 8z^2 r_+^2 + 6z^4) \}. \end{aligned} \quad (3.34)$$

One notes that the octupole correction (C_4) does not depend on the amplitude of the axial oscillations z of the ions in the trap. Equation (3.34)

Multipole	$z = 0$	$z = 2$	$z = 4$	$z = 8$
$l = 4$	36	36	36	36
$l = 6$	0.72	-8	-34	138
$l = 8$	0.01	1	15	248

Table 3.2: Contribution of the first three multipole to the electrical potential for various axial oscillations amplitude z (in mm). For comparison purpose, we assume $C_4 = C_6 = C_8 = 1$. Units are in Hz.

shows that if the size of each multipole goes down by a factor $1/d^2$, this is compensated by the large factor (e.g. $5/2$, $35/8$, etc.). Table 3.2 shows that higher order multiples dominate when the axial oscillations amplitudes are large. Therefore, it is important to ensure that the ions axial oscillation amplitudes are minimal in order to minimize frequency shifts.

3.3. Compensation of the Penning trap electrical potential

Frequency shifts from the non-harmonic terms in the trap potential are almost mass independent, hence the frequency ratio relative shift from equation (3.3) is

$$\left(\frac{\Delta R}{R}\right)_{pot.inhom.} = \Delta\nu \cdot \left(\frac{1}{\nu_1} - \frac{1}{\nu_2}\right) = \frac{\Delta\nu}{\nu_1 A_1} \Delta A. \quad (3.35)$$

Applying the conservative values $C_4 = 0.23$ and $C_6 = -0.26$ from the literature [Bol90], we get $\frac{\Delta\nu}{\nu_1 A_1} = 1.8 \times 10^{-7}$. This is at least a factor 100 times larger than any other sources of frequency shifts we have discussed so far. Therefore, it is necessary to minimize the $C_{N>2}$ coefficients to perform accurate mass measurement at the 10^{-9} range.

3.3 Compensation of the Penning trap electrical potential

In order to achieve accurate mass measurement at the 10^{-9} range, one needs to study and minimize the sources of systematic errors. From the previous sections, we saw that the largest possible source of error on the measured frequency ratio would come from the non-harmonic terms in the trapping potential.

Therefore the non-harmonic terms in the trapping potential need to be minimized as they could potentially induce large shift in the cyclotron frequency. This is done using the correction guard and tube electrodes shown in figure 2.10. The potentials V_{guard} and V_{tube} that provide the optimal compensation of the non-harmonic terms in the trapping potential can be obtained using several methods. TITAN's Penning trap used two different methods: the compensation using a dipole excitation and the compensation using a quadrupole excitation.

The first method, outlined in [Bec09] and described in section 3.3.2, consists of finding the potentials V_{guard} and V_{tube} that minimize the change in the reduced cyclotron frequency ν_+ with different axial oscillations amplitude z of the ion in the trap. The reason to chose the reduced cyclotron frequency is due to its larger sensitivity to the trapping potential V_0 than the cyclotron frequency ν_c as shown by:

$$\nu_+ \approx \nu_c - \frac{V_0}{4\pi B d^2}. \quad (3.36)$$

The second method is a novel approach described in section 3.3.3 and consists of finding the potential V_{guard} and V_{tube} that minimizes changes

in the cyclotron frequency ν_c with the conversion factor η . The second compensation method is used to confirm and refine the settings found by the first method.

3.3.1 Calculated correction tube and guard potentials

Before starting to compensate the non-harmonic terms using the methods outlined in sections 2.2.8.2 and 2.2.8.3, one needs to estimate the potentials V_{guard} and V_{tube} that would minimize the non-harmonic coefficients $C_{N>2}$. This is done by minimizing the difference between the potential produced by the trap electrodes and a quadratic target potential.

The potential produced by the individual electrodes along the axis was obtained using the software SIMION [Dah00]. Figure 3.7 shows the po-

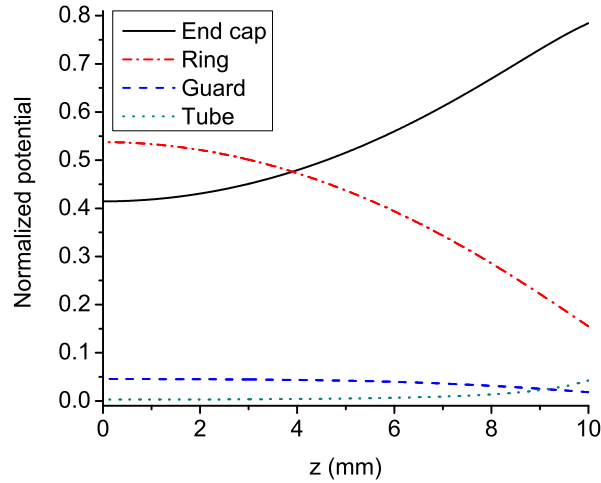


Figure 3.7: Normalized potentials produced by the different Penning trap electrode along the trap axis. The distance z is measured from the trap centre.

tentials of the four electrodes: the correction tube, the correction guard, the end caps and the ring electrode produced along the z -axis when 1 V is applied on these electrode individually.

The axial potential is given by a linear combination of these individual

3.3. Compensation of the Penning trap electrical potential

potentials:

$$V_{th}(z) = k_{cap}V_{cap}(z) + k_{ring}V_{ring}(z) + k_{guard}V_{guard}(z) + k_{tube}V_{tube}(z) \quad (3.37)$$

where k_i are scaling coefficients that needs to be determined. These coefficients minimize

$$\chi^2 = \sum \{V_{target}(z) - V_{th}(z)\}^2 \quad (3.38)$$

where the target potential V_{target} is purely harmonic:

$$V_{target}(z) = \frac{z^2}{z_0^2}. \quad (3.39)$$

Before minimizing equation (3.38), one needs to find initial scaling coefficient values. The values are chosen using the ideal quadratic potential given by equation (3.1). First, the end cap scaling factor was fixed to $k_{cap} = 1$. This removes one floating parameter in the χ^2 minimization. Then, using equation (3.1) and $k_{cap} = 1$, the starting value for the ring electrode scaling factor is found to be:

$$k_{ring} = -\frac{r_0^2}{2z_0^2} = -0.81. \quad (3.40)$$

The chosen starting value for the correction guard and tube electrodes scaling factor are respectively $k_{guard} = 0$ and $k_{tube} = 1$, which represents no correction.

Depending on the range along z over which the χ^2 minimization is performed, different scaling coefficients are found. A minimization range near the end cap holes (situated 11.785 mm from the trap centre) would result in a poorer compensation near the trap centre due to the large deviation from a quadratic form near the holes. However, if the minimization region is too close to the trap centre the scaling coefficients obtained would create a potential that rapidly diverges from the quadratic form outside the minimization region. Hence, we performed the minimization over the four scaling ranges shown in figure 3.8 and each time we computed the residuals

$$V_{res.} = V_{harm.} - V_{th} \quad (3.41)$$

where $V_{harm.}$ is a quadratic fit of the optimal potential V_{th} . At the 10 mm minimization range, the residuals diverge less with large z but fluctuate more when compared to the smaller minimization ranges. When the minimization range is less than 8 mm, the residuals start to diverge rapidly outside the

3.3. Compensation of the Penning trap electrical potential

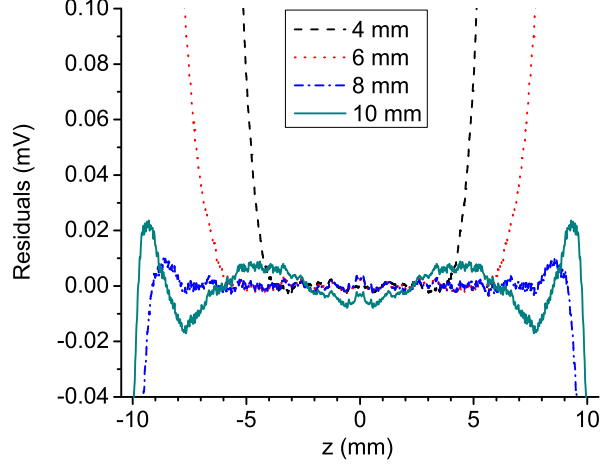


Figure 3.8: Residuals as a function of the minimization range.

k_{ring}	k_{tube}	k_{guard}	C_4	C_6
-0.786	1.640	0.078	-7×10^{-6}	5×10^{-5}

Table 3.3: Calculated normalized potential k_i needed to be applied on the ring, correction tube and guard electrodes in order to have an optimal compensation over a range of 8 mm from the trap centre.

minimization range while no net-improvement in the residuals fluctuations near the trap centre are observed. Therefore, we chose the scaling coefficient k_i obtained using a minimization range of 8 mm. The results are shown in table 3.3. The axial potential V_{th} has been fitted using

$$V(z) = \frac{V_0}{2} \left(C_0 + \frac{C_2}{d^2} z^2 + \frac{C_4}{d^4} z^4 + \frac{C_6}{d^6} z^6 \right), \quad (3.42)$$

in order to determine the size of the C_4 and C_6 coefficients obtained using the k_i shown in table 3.3. The obtained coefficients, presented in table 3.3, are a factor 10^{-4} smaller than the values from the literature [Bol90] presented earlier. This results in a similar decrease in the cyclotron frequency shift due to the non-harmonic terms in the trapping potential and this shows the importance of a proper compensation of the trap potential.

3.3. Compensation of the Penning trap electrical potential

Then, we investigated how the C_4 and C_6 coefficients change with k_{tube} and k_{guard} . To do so, we varied the scaling coefficients over the ranges $-1.0 \text{ V} < k_{guard} < 1.0 \text{ V}$ and $0.8 \text{ V} < k_{tube} < 2.0 \text{ V}$ and calculated the C_4 and C_6 coefficients using equation (3.42). Figure 3.9 shows that the C_4 and C_6

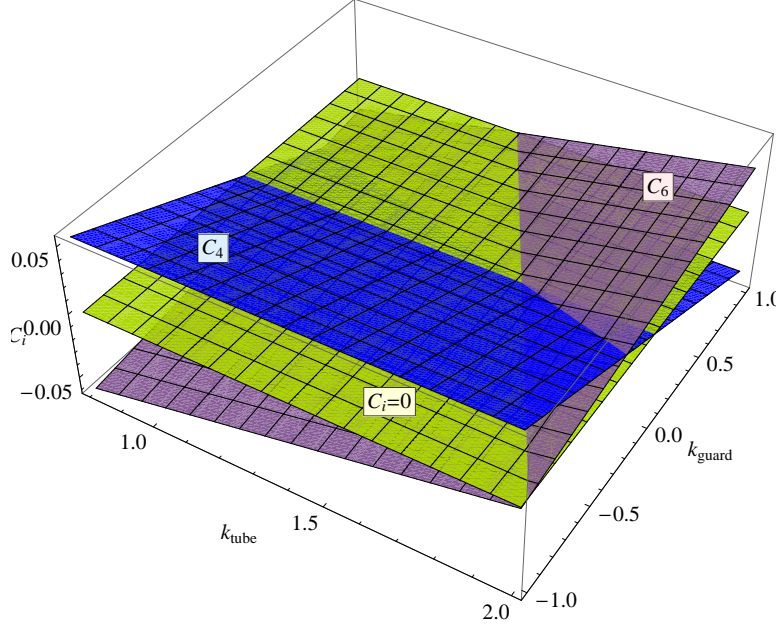


Figure 3.9: Linear variation in the strength of the C_4 and C_6 coefficients with k_{tube} and k_{guard} . Note that the planes crosses at $k_{tube} = 1.64\text{V}$ and $k_{guard} = 0.08\text{V}$.

coefficients vary linearly with both k_{tube} and k_{guard} . This gives rise to planes of equations

$$C_4 = 0.004 - 0.0003k_{tube} - 0.051k_{guard} \quad (3.43)$$

$$C_6 = -0.083 + 0.050k_{tube} + 0.017k_{guard} \quad (3.44)$$

in the $k_{tube} k_{guard}$ -space. Solving (3.43) and (3.44) for $C_4 = C_6 = 0$, gives consistent correction tube and guard voltages as presented in table 3.3.

As discussed in [Bro86], the octupolar term C_4 can be corrected by placing a correction guard electrode between the ring and end caps electrodes. This is confirmed by the stronger dependance of C_4 with k_{guard} as shown in (3.43). Figure 3.9 also shows that the dodecapole term C_6 is mainly affected by k_{tube} , confirming what was seen in the literature [Bol90].

3.3. Compensation of the Penning trap electrical potential

To finish this section, we discuss the effect of the correction tube and guard voltage on the reduced cyclotron frequency. In section 3.3.2, the non-harmonic components of the trapping potential are compensated by measuring the reduced cyclotron frequency difference

$$\Delta\nu_+ = \nu_+(z = z_0) - \nu_+(z = 0) \quad (3.45)$$

where the axial amplitude z is varied by changing the capture timing in the trap. $z = 0$ correspond to the trap centre and $z = z_0$ to a large axial amplitude. The compensation is performed by varying k_{tube} and k_{guard} until no changes in the reduced cyclotron frequency ($\Delta\nu_+ = 0$) are seen. The k_{tube} and k_{guard} found corresponds to the optimal compensation.

Then using the linear change of the C_4 and C_6 coefficients with k_{tube} and k_{guard} :

$$C_i = a_i k_{tube} + b_i k_{guard} + c_i \quad (3.46)$$

allows one to write the reduced cyclotron frequency difference as:

$$\Delta\nu_+ = \sum_{i=2}^{\infty} a_{2i} h_{2i} k_{tube} + \sum_{i=2}^{\infty} b_{2i} h_{2i} k_{guard} + \sum_{i=2}^{\infty} c_{2i} h_{2i}, \quad (3.47)$$

where h_{2i} are functions of the axial and radial position of the ions in the trap, e.g. for h_4 and h_6 we have

$$h_4 \approx -\frac{3\nu_-}{2d^2} z^2 \quad (3.48)$$

$$h_6 \approx -\frac{45\nu_- z^2}{16d^4} \{z^2 - 2(r_+^2 + 2r_-^2)\}. \quad (3.49)$$

Both coefficients are unaffected by a variation of C_4 and C_6 . The optimal compensation condition $\Delta\nu_+ = 0$ leads to several optimal values for k_{tube} and k_{guard} , all lying along a straight line of equation

$$k_{tube} = -\frac{\sum_{i=2}^{\infty} b_{2i} h_{2i}}{\sum_{i=2}^{\infty} a_{2i} h_{2i}} k_{guard} - \frac{\sum_{i=2}^{\infty} c_{2i} h_{2i}}{\sum_{i=2}^{\infty} a_{2i} h_{2i}}. \quad (3.50)$$

Since there can be only one sets of k_{tube} and k_{guard} that leads to a minimal value of the C_4 and C_6 coefficients (see figure 3.9), and therefore to an optimal compensation, one needs a second compensation approach that selects the correct setting along this line. This is the reason for carrying out two different methods of compensating the trap.

3.3.2 Penning trap compensation using a dipole excitation

The traditional procedure to compensate the electrical potential of a Penning trap consists of measuring the reduced cyclotron frequency ν_+ of the ion in the trap for two extreme axial oscillations amplitude z : one with minimal oscillation and the other with large oscillations. The optimal compensation is the one that minimizes the change in the reduced cyclotron frequency with the axial oscillation amplitude.

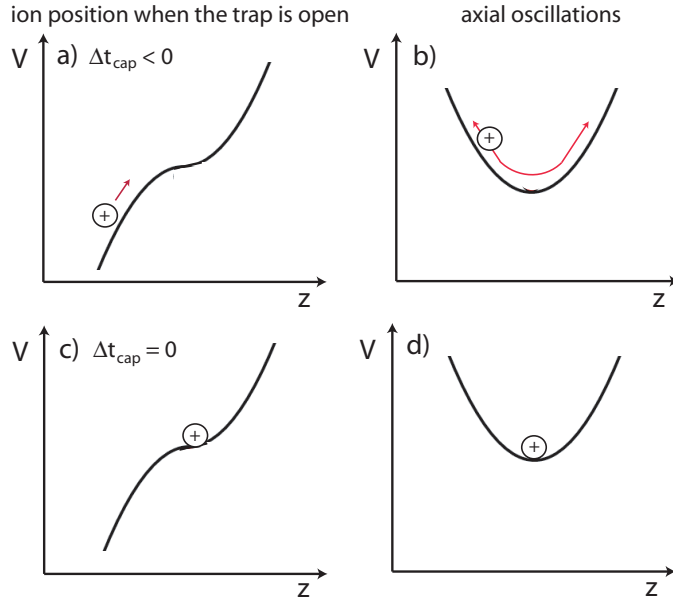


Figure 3.10: Axial oscillations of the ion in the trap as function of the closing time of the trap. a) The ion did not reach the trap centre when it was closed b) results in large axial oscillations c) the ion stopped in the trap centre when it was closed d) results in minimal oscillations.

The size of the oscillations is controlled by the closing time of the trap when the ions are injected as shown in figure 3.10. Assuming that the ions have the correct energy, they will stop once they reach the trap centre and if at this point the trap is closed, the ions should have minimal axial oscillation amplitude (see figure 3.10 (c) and (d)). However, if the trap is closed earlier or later, it results in larger axial oscillation amplitudes (see figure 3.10 (a) and (b)).

From equation (3.32), the reduced cyclotron frequency changes with the

3.3. Compensation of the Penning trap electrical potential

axial oscillation amplitude quadratically. However, the position of the ion in the trap at the closing time depends on time quadratically (as they are decelerating towards the trap centre). Therefore, the change in reduced cyclotron frequency with the closing time t_{cap} of the trap has a quatic form: $\nu_+ \propto ct_{cap}^4 + dt_{cap}^3 + \dots$ and the location of the trap centre $z = 0$ corresponds to where the frequency is either maximal or minimal. Figure 3.11 shows that

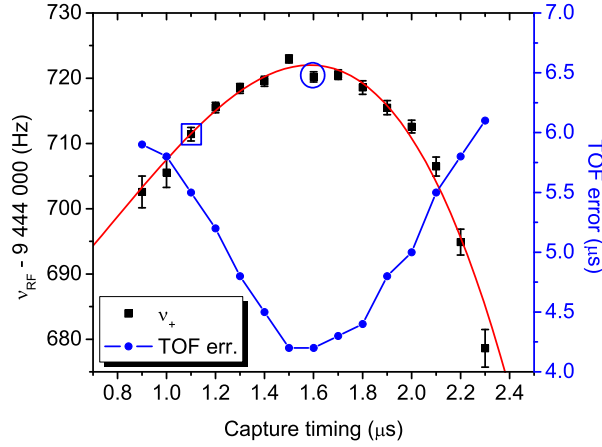


Figure 3.11: Left axis: reduced cyclotron frequency as a function of the capture timing in the Penning trap. The curve is a quatic fit and is centred where the TOF error is minimal (circled). This corresponds to the location of the trap centre. Right axis: time-of-flight distribution width, which is minimal at the trap centre. The circle and square indicates the two capture timings that are compared when optimizing the correction electrodes potential.

for $k_{tube} = 1.60$, $k_{guard} = -0.05$, the values of the different C_i coefficients is such that the reduced cyclotron frequency is maximal at the trap centre (indicated by the circle). This trap centre capture timing is confirmed by the width of the time-of-flight distribution being minimal at this point (see Appendix B.2 for more details).

By changing either the correction guard or tube potential, one changes the values of the C_i coefficients as expressed in equation (3.46). This changes the amplitude and direction of the concavity of the equation $\nu_+ = az^2 + b$, as shown by figure 3.12.

3.3. Compensation of the Penning trap electrical potential

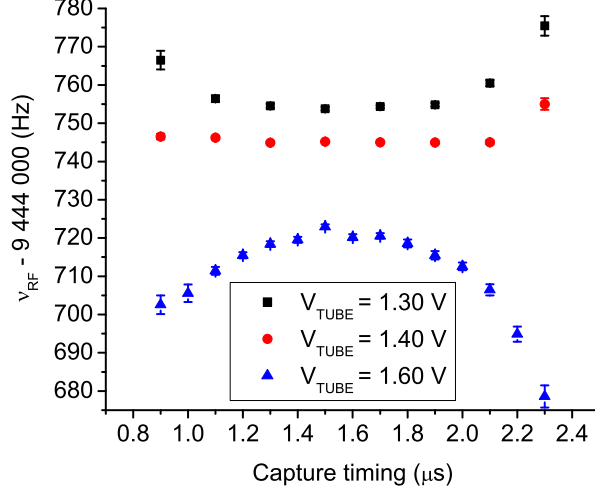


Figure 3.12: Variation in the reduced cyclotron frequency with the capture timing in the Penning trap for different correction tube potential k_{tube} . Note that close to $k_{tube} = 1.40$, the variation in ν_+ seems to be minimal. For these scans, $k_{guard} = -0.05$.

Thus, the $C_{i>2}$ coefficients are minimized by changing the potential on the correction electrodes and taking the difference between the measured ν_+ at the trap centre (circled in figure 3.11) and the ν_+ at a location away from the centre (squared in figure 3.11) $\Delta\nu_+ = \nu_+(t_{cap} = 1.1\mu s) - \nu_+(t_{cap} = 1.6\mu s)$.

Figure 3.13 shows the linear behaviour in the reduced cyclotron frequency difference $\Delta\nu_+$ with the correction tube voltage for $k_{guard} = -0.05$. A linear regression of the data shows that $\Delta\nu_+$ crosses zero for $k_{tube} = 1.464(4)$. As discussed in section 3.3.1, this would correspond to one of the possible optimal compensation. Therefore, we repeated the procedure for different correction guard potentials k_{guard} . Figure 3.14 shows that all the optimal k_{guard} and k_{tube} values lie along a straight lines as expected from equation (3.50). In order to select the setting that optimizes the compensation, we need a second approach of compensating the trap.

3.3. Compensation of the Penning trap electrical potential

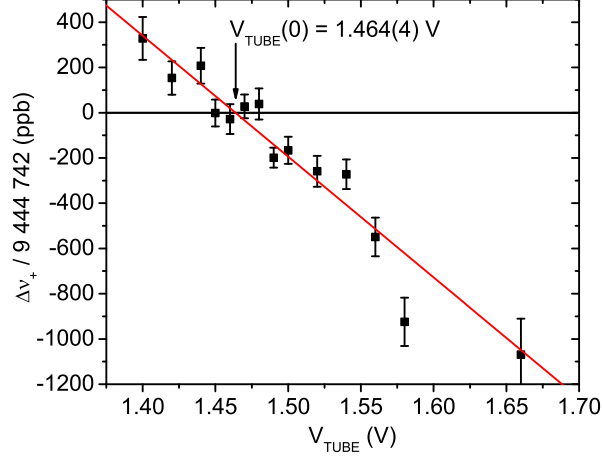


Figure 3.13: Change in the reduced cyclotron frequency difference $\Delta\nu_+$ with the correction tube potential k_{tube} for a correction guard potential of $k_{guard} = -0.05$. Note the linear change in $\Delta\nu_+$ with t_{cap} . The linear fit crosses $\Delta\nu_+ = 0$ for $k_{tube} = 1.464(4)$.

3.3.3 Penning trap compensation using a quadrupole excitation

This is a novel approach to compensate the Penning trap electrical potential. It consists of measuring the cyclotron frequency of the ion for two different conversion factor η (see section 2.4.4), which defines the sizes of the magnetron and reduced cyclotron radii at the end of the excitation phase. Hence from equation (3.34), their cyclotron frequency will be different. The non-harmonic terms are minimized by finding the potential k_{guard} and k_{tube} that minimizes the change in the cyclotron frequency with η .

Since both octupole and dodecapole terms depend on the difference between the reduced cyclotron and the magnetron eigenmotion amplitudes $r_+^2 - r_-^2$, one can optimize the trapping potential by looking at differences in ν_c for different r_+ and r_- amplitudes. The relative size of the radial amplitudes r_{\pm} is changed by using different degree of conversion of the initial magnetron motion into reduced cyclotron motion. This is done through a variation of the RF amplitude V_{RF} .

3.3. Compensation of the Penning trap electrical potential

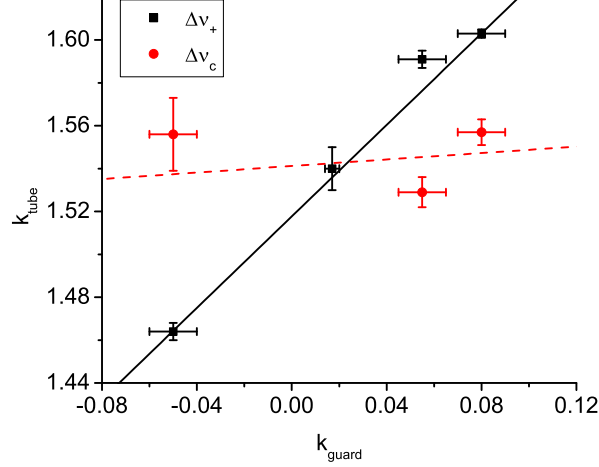


Figure 3.14: Optimal k_{guard} and k_{tube} founded using a minimization of $\Delta\nu_+$ and $\Delta\nu_c$. The intersection of the solid and dashed lines correspond to the optimal combination of k_{guard} and k_{tube} .

In order to have a better understanding of the change of the cyclotron frequency with η , we study the behaviour of the radial eigenmotion amplitudes r_{\pm} with the conversion factor η . For an ideal Penning trap with $C_{i>2} = 0$, when the ions are excited at the cyclotron frequency, the amplitude of their radial eigenmotions are given by

$$r_+(t) = -\frac{r_0 k_0^+}{2\omega_B} \sin \omega_B t e^{-\delta t/2} \quad (3.51)$$

$$r_-(t) = r_0 \left\{ \cos \omega_B t + \frac{\gamma \omega_c}{2\omega_B} \sin \omega_B t \right\} e^{-\delta t/2} \quad (3.52)$$

where we assume that the initial radii $r_+(0) = 0$ and $r_-(0) = r_0$. Without any damping ($\delta = 0$), the radius of the two motions is the same at half conversion ($\eta = 0.5$). For non-zero damping ($\delta \neq 0$), this is not the case, as the magnetron radius is reduced with time. This leads to the radii of the two motions being equal at a smaller conversion factor ($\eta < 0.5$).

In the case where $C_{i>2} \neq 0$, it is no longer possible to use equation (3.51) and (3.52), as the non-quadratic terms modify the equation of motion. Therefore, in order to study how ν_c changes with V_{RF} , we numerically solved

3.3. Compensation of the Penning trap electrical potential

the equation of motion with an added C_4 term

$$\ddot{x} = \frac{\omega_z^2}{2} x \left\{ 1 + \frac{C_4}{d^2} \left(6z^2 - \frac{3}{2}(x^2 + y^2) \right) \right\} - \omega_c \dot{y} + k_0 \cos(\omega_{RF} t) y \quad (3.53)$$

$$\ddot{y} = \frac{\omega_z^2}{2} y \left\{ 1 + \frac{C_4}{d^2} \left(6z^2 - \frac{3}{2}(x^2 + y^2) \right) \right\} + \omega_c \dot{x} + k_0 \cos(\omega_{RF} t) x \quad (3.54)$$

$$\ddot{z} = -\omega_z^2 z \left\{ 1 + \frac{C_4}{d^2} (2z^2 - 3(x^2 + y^2)) \right\}. \quad (3.55)$$

The addition of the C_4 term the equation of motions for the x and y radial motions couples with the axial z motion. But by numerically solving this system for small axial amplitudes in z , one finds that the radial and axial motions only weakly affect each another. Therefore, in order to minimize computing time, only the simplified case were $z = 0$ is considered.

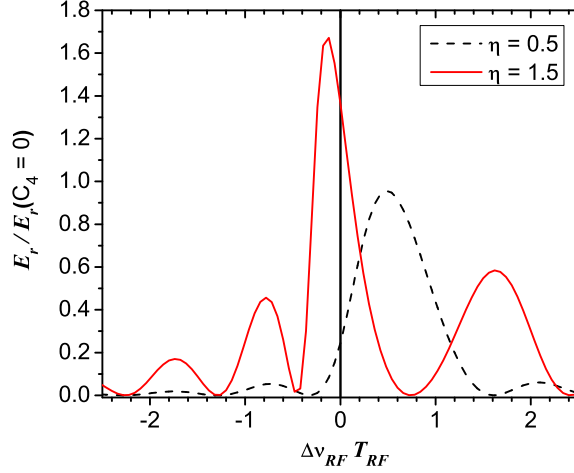


Figure 3.15: Radial energy gain E_r as a function of the detuning $\Delta\nu_{RF} T_{RF}$ for conversion factor $\eta = 0.5$ and 1.5 for $C_4 T_{RF} = 0.01$. The energy gain was normalized to the radial energy obtained from $C_4 = 0$.

Upon solving these equations, one receives the radial energy

$$E_r(\Delta\nu_{RF}) = \frac{1}{2} m (\dot{x}(\Delta\nu_{RF})^2 + \dot{y}(\Delta\nu_{RF})^2) \quad (3.56)$$

3.3. Compensation of the Penning trap electrical potential

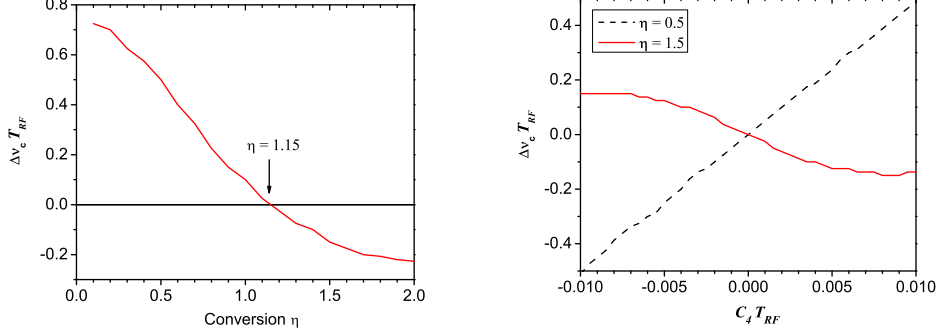


Figure 3.16: Left: Shift in the cyclotron frequency as a function of the conversion factor η for $C_4 T_{RF} = 0.01$. Note that there is no shift for $\eta = 1.15$. Right: Change in the frequency shift $\Delta\nu_c$ as function of the octupole coefficient C_4 with $\eta = 0.5, 1.5$.

profiles as a function of the frequency detuning $\Delta\nu_{RF}$ shown in figure 3.15. Notice that with a $C_4 \neq 0$, the radial energy profile is no longer symmetric. The deformation is more pronounced for over-converted resonances ($\eta > 1$), as their line width is smaller. For the under-converted case ($\eta < 1$), the centre frequency gets more shifted. This is due to the fact that the ion magnetron motion is not fully converted into reduced cyclotron motion. Hence the ion then spent more time in regions where the $C_{i>2}$ components are larger, leading to a larger shift in the centroid frequency.

The left panel of figure 3.16 shows that the cyclotron frequency ν_c shifts strongly for $\eta < 1$, and once full conversion is reached, it changes more slowly. Therefore, as shown by the right panel of figure 3.16, by investigating the difference in cyclotron frequency between an under-converted ($\eta = 0.5$) and over-converted ($\eta = 1.5$) time-of-flight resonance spectra, one finds where $C_{i>2} = 0$. The linear behaviour of C_4 with $\Delta\nu_c$ shown in figure 3.16 demonstrates that the $r_+^2 - r_-^2$ term in equation (3.34) is independent of C_4 . The $\eta = 1.5$ case however, does not present a linear behaviour and the conclusion is that for this case, the term $r_+^2 - r_-^2$ is dependant on the C_4 parameter.

For a given correction guard potential k_{guard} , the optimal k_{tube} is the one that minimizes $\Delta\nu_c = \nu_c(\eta = 0.5) - \nu_c(\eta = 1.5)$ and that also leads to the most symmetric over-converted time-of-flight resonance spectra. We will now present the k_{tube} scan performed using $k_{guard} = 0.06$. For this scan,

3.3. Compensation of the Penning trap electrical potential

there were three tube voltages that gave symmetric time-of-flight resonance spectra. The cyclotron frequency for these k_{tube} was determined and are

k_{tube}	ν_c (Hz)
1.52	9 450 812.021(25)
1.55	9 450 812.040(26)
1.58	9 450 812.053(27)
mean	9 450 812.038(15)

Table 3.4: Cyclotron frequency for correction tube potential k_{tube} that gave symmetric over-converted time-of-flight resonance spectra. Also given is the weighted mean of the frequencies. Statistical error is given in brackets.

summarized in table 3.4. These three cyclotron frequencies agree within uncertainty and their weighted mean was taken as the cyclotron frequency for which the $C_{i>2}$ are minimized. Then, the difference between the under-converted cyclotron frequency and the over-converted cyclotron frequency of table 3.4 was calculated for different correction tube voltage as shown in figure 3.17. A linear regression of $\Delta\nu_c$ leads to an optimal correction tube voltage of $k_{tube} = 1.53(1)$.

Method	slope	y-intercept (V)
$\Delta\nu_+$	1.07(3)	1.520(2)
$\Delta\nu_c$	0.07(14)	1.541(9)

Table 3.5: Slope and y-intercept of the linear fits shown in figure 3.14.

The same procedure was repeated for correction guard voltages of $k_{guard} = 0.08$ and -0.05 . The three different optimal k_{guard} and k_{tube} found using this method, together with a linear regression, are presented in figure 3.14. The optimal compensation of the non-harmonic terms in the trapping potential was taken as the intersect of the two straight lines. The slope and y-intercept values of these two linear regressions is given in table 3.5. These two lines intersect for $k_{tube} = 1.54(1)$ and $k_{guard} = 0.02(1)$. The validity of this result was verified by looking for potential changes in the cyclotron frequency with the conversion factor η . Figure 3.18 shows that the changes in the cyclotron frequency is minimal for the optimal $k_{tube} = 1.54(1)$ and $k_{guard} = 0.02(1)$ compensation. The largest change in frequency with the conversion factor observed is 80(50) mHz. For comparison purposes, three

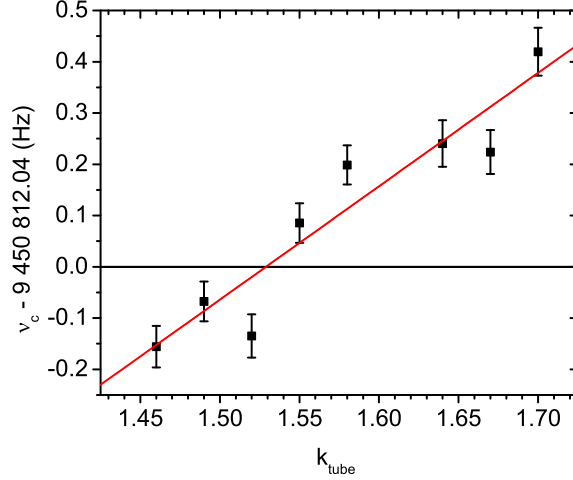


Figure 3.17: Change in the fitted cyclotron frequency $\Delta\nu_c$ with a the voltage applied on the correction tube electrode k_{tube} for an RF amplitude that yield a conversion factor $\eta = 0.54$.

other settings are shown. When k_{tube} is very different from the optimal value, it induces a strong shift in the cyclotron frequency for low ($\eta < 1$) conversion factor, while for ($\eta > 1$), the frequency presents minimal changes. This is the same behaviour as discussed previously in figure 3.16.

Figure 3.18 also shows that the cyclotron frequency changes with the conversion factor η for the setting $k_{tube} = 1.46$ and $k_{guard} = -0.05$. This setting was previously found as being optimal using the minimization of $\Delta\nu_+$ method. However, the observed change in frequency is 260(80) mHz, which is three times larger than $k_{tube} = 1.54(1)$ and $k_{guard} = 0.02(1)$ compensation. Therefore, this confirm the importance of compensating the non-harmonic terms of the potential by using two different observables.

3.3.4 Effect of the incomplete compensation of the trapping potential of the TITAN Penning trap on the measured frequency ratio

After the compensation is performed, the magnitude of the systematic error due to the incomplete compensation of the non-harmonic terms in the trap-

3.3. Compensation of the Penning trap electrical potential

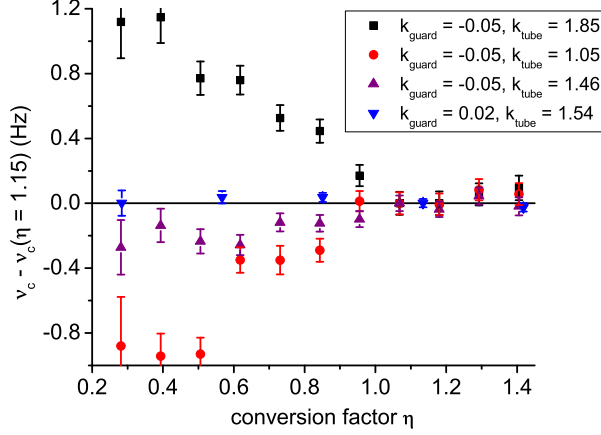


Figure 3.18: Fitted cyclotron frequency as a function of the conversion factor η for different correction tube (k_{tube}) and guard (k_{guard}) potentials.

ping potential, $\Delta\nu/(\nu A)$ in equation (3.35), needs to be evaluated. This is done by measuring the frequency ratio of ions with two different mass number A . The frequency ratio is used to calculate the atomic mass of one of the two species using equation (2.49). The mass obtained is compared to the value of the AME03 [Aud03] and the difference in mass $\Delta m = m(\text{TITAN}) - m(\text{AME03})$ is used to compute the systematic error due to the incomplete compensation of the trap:

$$\frac{\Delta\nu}{\nu A} = \frac{\Delta m}{m\Delta A} \quad (3.57)$$

where $\Delta A = A_{cal} - A$ is the difference in mass number between the calibration and the measured species.

The systematic error due to the incomplete compensation of the trap has been calculated from a mass measurement of ^{23}Na using H_3O ($A = 19$) as calibration and similarly for ^{39}K using ^{23}Na as calibration. The resulting ^{23}Na and ^{39}K masses difference with the AME03 are shown in table 3.6. Both measurement show a smaller value of the mass when a calibrant less massive than the ion of interest is used. The total shift in frequency ratio due to the incomplete compensation of the trap was then taken as the weighted mean of the $\Delta\nu/(\nu A)$ for $\Delta A = 4$ and 16. The resulting $\Delta\nu/(\nu A) = -0.5(5)$ ppb/u, is below the aimed-for uncertainty at TITAN.

3.4. TITAN Penning trap trap-independent systematic errors

Specie	ΔA	Δm (eV)	$\Delta\nu/(\nu A)$ (ppb/u)	N
^{23}Na	4	-71(77)	-0.8(9)	12
^{39}K	16	-243(263)	-0.4(6)	13
Total			-0.5(5)	25

Table 3.6: Difference in the mass excess of ^{23}Na and ^{39}K as measured with the TITAN Penning trap and from the AME03. ^{23}Na used H_3O as calibration and ^{39}K used ^{23}Na as calibration. From these measurements the systematic error due to the incomplete compensation $\Delta\nu/(\nu A)$ is derived.

3.4 TITAN Penning trap trap-independent systematic errors

In this section, we present trap-independent systematic errors. These are systematic effects that are not caused by the trap geometry, the alignment of the trap or the magnetic field inhomogeneties. These systematic effects includes magnetic field fluctuations over time, ion-ion interaction and relativistic effects.

3.4.1 Effects of nonlinear magnetic field fluctuations

In the TOF-ICR technique, the value of the magnetic field during the measurement of the cyclotron frequency of the ion of interest is calculated using equation (2.47) where the calibration cyclotron frequency is obtained from a linear interpolation between two calibration measurements as shown in figure 2.15. This procedure assumes that the magnetic field change between the two calibrations is linear. This is valid for a “short” time span between calibrations. However, variation of the magnetic field due to temperature and pressure fluctuations are present [Kel03]. Such variations are nonlinear and result in an error in the determination of the calibration cyclotron frequency by linear interpolation. Therefore, the length of this “short” time span depends on the aimed precision and the size of the magnetic field fluctuations. In order to estimate the error due to the linear interpolation of the magnetic field, a series of ^7Li frequency measurement separated by 6 minutes, were performed over 16 hours. The resulting change in the frequency are shown in the top graph of figure 3.19. Then, the ^7Li cyclotron frequencies were interpolated between calibrations. After, the difference between these interpolations and the actual frequency measurement are calculated.

3.4. TITAN Penning trap trap-independent systematic errors

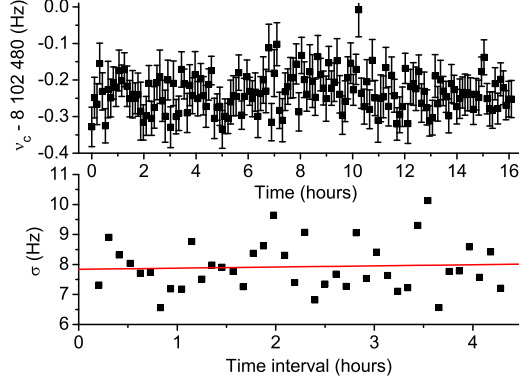


Figure 3.19: Upper plot shows the variation in the cyclotron frequency of ${}^7\text{Li}$ over a period of 16 hours. The lower plot gives the standard deviation of differences between measured and interpolated values for increasing time interval between calibration. The linear regression gives the systematic error due to the linear frequency interpolation.

The standard deviation of these measurements is derived for different time intervals between calibration. The results are shown in the bottom half of figure 3.19. This routine was performed for intervals of up to 4 hours, and a linear fit of the deviations gave an increase in the standard deviation of $\delta\nu/\nu = 0.04(11)$ ppb/h.

Measurement	max. time span (h)	$(\Delta R/R)_{inter.}$ (ppb)
${}^6\text{Li}$	1.0	0.2
${}^{6,8}\text{He}$	3.4	0.5

Table 3.7: Systematic error due to the magnetic field fluctuations $(\Delta R/R)_{inter.}$ depending on the largest time span between calibrations for the ${}^6\text{Li}$ and ${}^{6,8}\text{He}$ mass measurements.

Table 3.8 gives the systematic error due to the magnetic field fluctuations used for the ${}^6\text{Li}$ and ${}^{6,8}\text{He}$ mass measurements. To be conservative, we determined the error from the largest time span seen between the ${}^7\text{Li}$ calibrations.

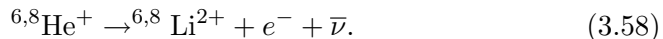
3.4.2 Effect of ion-ion interaction in the Penning trap

When more than one ion is present in a Penning trap, the individual eigenmotions are perturbed by the Coulomb interaction between the ions. This effect can happen for simultaneous trapping of multiple ions of the same species or different species. Frequency shift due to the storage of multiple ions can be minimized by ensuring to have small numbers of ions in the trap and by reducing the unwanted species contamination. In general, only one to at most five ions are stored simultaneously in the trap, where the number is determined from the number of counts recorded on the MCP detector. Possible contamination ions could either come with the beam or can be created in the Penning trap.

The first type of contamination comes either from the ion source (ISAC or off-line source) or is generated in the RFQ when using singly charged ions. When contamination is produced at ISAC, depending on its mass difference with respect to the desirable species, it could be resolved and removed using the separator. The resolution of the mass separator is $m/\Delta m = 3000$. In the case of ${}^6\text{He}$ and ${}^8\text{He}$, all the contamination has been resolved using the mass separator (table 2.1).

Other type of contamination could come from the RFQ, where the beam can undergo charge exchange with the buffer gas or residual gas. However, the RFQ can perform a mass-selection and the mass difference between the lightest contaminant ($A = 18$) and mass $A = 6, 8$ is large enough to remove it from the RFQ. When two species cannot be resolved using the RFQ, such as ${}^6\text{Li}$ and ${}^7\text{Li}$, it could be removed using the time-of-flight gate, which has a resolving power of 20. In the case that all pre-selection is insufficient, the contaminant is removed by the application of a dipolar excitation at the reduced cyclotron frequency in the Penning trap. This excitation results in an increase of the reduced cyclotron motion radius and can achieve resolving power of at least 10^6 .

The second class of contamination is formed inside the Penning trap and depending on the nature of the ion, it could also interact with a residual gas molecule via charge exchange or form a molecule. Another source of contamination, which arises only for radioactive ions, is when decay products remain in the trap. Both ${}^6\text{He}^+$ and ${}^8\text{He}^+$ decay through β^- emission



Because of the relatively low trapping potential $V_0 = 3.6$ V compared to the Q -value of the decay, only a tiny fraction of the ${}^{6,8}\text{Li}^{2+}$ produced by the decay remains trapped. However, the outgoing electron or positron can

3.4. TITAN Penning trap trap-independent systematic errors

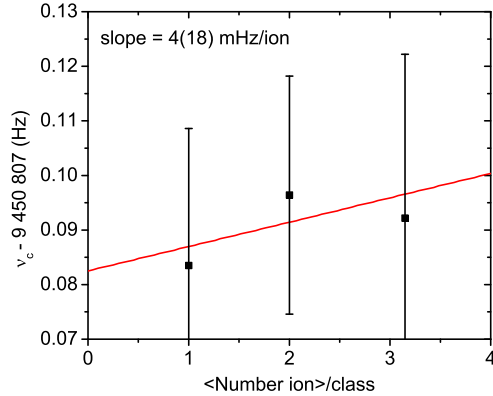


Figure 3.20: Typical count rate analysis for one ${}^6\text{Li}$ spectrum. The slope of the linear regression is 4 ± 18 mHz/ion.

ionize residual gas or sputter material from the electrodes. The contamination formed in the trap during the quadrupolar excitation phase cannot be removed. Therefore, because the ion can interact with residual gas or decay products, the effect of that contamination on the measured cyclotron frequency needs to be investigated.

The possible frequency shifts are investigated by a count rate analysis [Kel03] on the individual measurements. In such an analysis, the data of a given measurement is divided into three different classes regarding the number of detected ions. For each of these classes, the cyclotron frequency is fitted and a linear regression of the frequencies is performed. Figure 3.20 shows an example of such a linear regression. As it can be seen, the fluctuations in the frequency are well within error, which results in a negligible slope of 4 ± 18 mHz/ion.

However, in order to have quantitative information about the change in frequency with the number of ions, such fits were performed for all spectra taken during the measurements (if there were enough recorded counts to perform the fit) presented in this thesis. The shift in frequency due to the number of trapped ions was taken as the weighted mean of all the slopes from the fits.

The resulting shifts in frequency as a function of the number of trapped ions are shown in table 3.8. While the measurements for ${}^7\text{Li}$ display a down-

3.4. TITAN Penning trap trap-independent systematic errors

Specie	Slope $\Delta\nu_c$ (mHz/ion)	N
${}^7\text{Li}$	-1.4(2.9)	115
${}^6\text{Li}$	8.4(3.2)	77
Both Li	3.1(2.2)	189
${}^4\text{He}$	-18.5(14.2)	5
${}^6\text{He}$	-9.3(51.4)	8
${}^8\text{He}$	100.2(150.0)	5

Table 3.8: Cyclotron frequency shift due to the interaction of multiple ions in the Penning trap for all measurements presented in this thesis. N is the number of measurements used to calculate the average slope.

wards frequency shifts within error, the measurements for ${}^6\text{Li}$ are consistent with a non-zero upward shift. This excludes possible interaction of ${}^6\text{Li}$ with ionized background gas, as it would have shifted the frequency downwards. The frequency shift were taken as the weighted mean of the ${}^6\text{Li}$ and ${}^7\text{Li}$ shifts leading to a shift of 3.1(2.2) mHz/ion. Table 3.8 also shows the frequency shifts for ${}^4\text{He}$, ${}^6\text{He}$ and ${}^8\text{He}$. The larger error for ${}^8\text{He}$ comes from lower statistics.

Specie	N	$(\Delta R/R)_{ion}$ (ppb)
${}^4\text{He}$	2	4.3
${}^6\text{Li}$	3	0.2
${}^6\text{He}$	2	8.1
${}^8\text{He}$	1	13.3

Table 3.9: Cyclotron frequency ratio shift $(\Delta R/R)_{ion}$ due to the interaction of multiple ions in the Penning trap. N is the number of ions chosen in the analysis. $N_{cal.} = 3$ for ${}^7\text{Li}$.

Based on equation (3.3), the shift in the frequency ratios due to the ion-ion interaction is calculated using

$$(\Delta R/R)_{ion} = (N_{cal.} - \varepsilon)\Delta\nu_{c,cal.}/\nu_{c,cal.} - (N - \varepsilon)\Delta\nu_c/\nu_c, \quad (3.59)$$

where $\varepsilon = 0.6$ is the detection efficiency of the MCP and $\Delta\nu_c$, $\Delta\nu_{c,cal.}$ are the frequency shifts with the number of ions for the ion of interest and calibration respectively. The maximum number of detected ions chosen in the analysis for the ion of interest and the calibrant are given by N and

$N_{cal.}$ respectively. This gives a conservative estimate of the error due to the ion-ion interaction and in the present cases most of the events contain less than the maximum number of detected ions. In fact, considering the detection efficiency of the MCP, the average number of true ions at the end of a trap cycle for ${}^6\text{He}$ and ${}^8\text{He}$ were respectively less than 0.7 and 0.2 ions.

Using equation (3.59), we calculated the error on the frequency ratio due to the multiple ions in the Penning trap using the values from table 3.8 and the results are in table 3.9. $N = N_{cal.} = 3$, was chosen for ${}^6\text{Li}$ and ${}^7\text{Li}$ as the slope (and its uncertainty) for these species is relatively small, and very little contamination was seen in the TOF distribution of these species. As more contaminant are present for the helium isotopes, we decided to keep at most two detected ions for ${}^{4,6}\text{He}$, in order to be conservative. For ${}^8\text{He}$, due to its low count rate and the large uncertainty in $\Delta\nu_c$, we decided to keep only one detected ion. The values for the frequency ratio shift $(\Delta R/R)_{ion}$ shown in table 3.9 are taken as the upper value on the uncertainty.

3.4.3 Relativistic effects on the cyclotron frequency

The derivation of the equation of motion in section 2.1.1 assumes that the ion motion is non-relativistic. However, when the cyclotron frequency of a light ion is measured with enough precision, relativistic effects are important and have to be taken into account. For example, the average velocity of a ${}^6\text{Li}^+$ ion moving at the reduced cyclotron frequency with an initial magnetron radius of 1 mm in TITAN's Penning trap is approximately $1 \times 10^{-4} c$. This, according to special relativity, would modify the measured cyclotron frequency from the one given in equation (2.46) by 5×10^{-9} , which is at the level of precision that the masses of ${}^6\text{Li}$, ${}^6,8\text{He}$ are determined.

The relativistic expression for the cyclotron frequency is

$$\nu_c(t) = \frac{1}{2\pi} \frac{q \cdot B}{\gamma \cdot M_0} = \nu_{c,0} \cdot \sqrt{1 - \beta(t)^2} \quad (3.60)$$

where $\beta(t)$ is the velocity of the ion in the trap divided by the speed of light, M_0 is the ion rest mass and $\nu_{c,0}$ is the non-relativistic cyclotron frequency. As the velocity of the ion changes over the excitation time, this consequently modifies the cyclotron frequency. Therefore, we approximate the ion's velocity in the trap as the time-averaged velocity $\bar{\beta}c$.

Since the reduced cyclotron frequency ν_+ is several orders of magnitude larger than the magnetron frequency ν_- , the average velocity of the ion in the trap is dominated by the reduced cyclotron motion ν_+

$$\bar{\beta} \simeq \bar{\rho}_+ \cdot 2\pi \cdot \nu_+ / c = \rho_{-,ini} \cdot k \cdot 2\pi \cdot \nu_+ / c, \quad (3.61)$$

3.4. TITAN Penning trap trap-independent systematic errors

where $\rho_{-,ini}$ is the initial magnetron radius of the ion in the trap and k is a integration constant obtained by integrating the radius of the reduced cyclotron motion ρ_+ over the measurement period:

$$k = \frac{1}{T_{RF}} \int_0^{T_{RF}} \left| \frac{k_0 \sin \omega_B t e^{-\delta t/2}}{2\omega_B} \right| dt. \quad (3.62)$$

The ions are provided with their initial magnetron radius prior to their injection in the Penning trap using a Lorentz steerer. Studies and simulations of this device have shown that the initial magnetron radius $\rho_{-,ini}$ provided by the Lorentz steerer is proportional to its steering voltage ΔV_{LS} :

$$\rho_{-,ini} = s \cdot \Delta V_{LS}, \quad (3.63)$$

where s is the steering strength. Hence, the size of the cyclotron frequency shift can be controlled by changing the steering voltage ΔV_{LS} :

$$\nu_c = \nu_{c,0} \sqrt{1 - (a \cdot \Delta V_{LS})^2} \quad (3.64)$$

where

$$a = s \cdot k \cdot 2\pi \cdot \nu_+ / c. \quad (3.65)$$

Then, the corrected mean frequency ratio to account for relativistic effects is given by

$$\bar{R}_{rel.corr.} = \bar{R}_{meas.} \cdot (1 - (\Delta R/R)_{rel.}) \quad (3.66)$$

where $\bar{R}_{meas.}$ is the measured mean frequency ratio for the given ΔV_{LS} and $\Delta V_{LS,cal.}$ and

$$(\Delta R/R)_{rel.} = 1 - \frac{\sqrt{1 - (a \cdot \Delta V_{LS})^2}}{\sqrt{1 - (a_{cal.} \cdot \Delta V_{LS,cal.})^2}} \quad (3.67)$$

is the relative change in the frequency ratio. In section 3.4.3.1, we show how the change in frequency ratio due to relativistic effect is calculated for ${}^6\text{Li}$ and in section 3.4.3.2, we show how it is done for ${}^{6,8}\text{He}$.

3.4.3.1 Case study of relativistic shift at the TITAN Penning trap: ${}^6\text{Li}$

The change in the frequency ratio stemming from relativistic effect is important when the mass of a light nuclei is measured with a precision below the 10^{-8} range. As the precision we aim for the ${}^6\text{Li}$ mass measurement is in the 10^{-9} range, we need to account for this effect and minimize it. In this

3.4. TITAN Penning trap trap-independent systematic errors

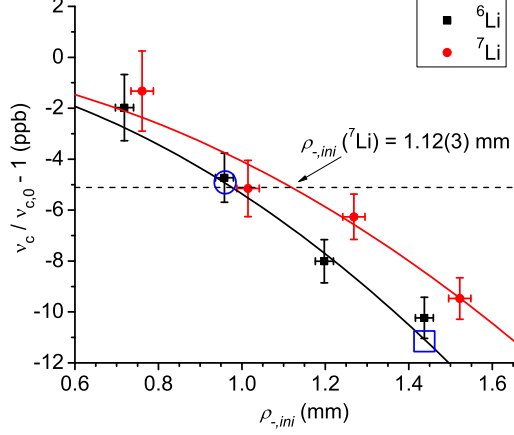


Figure 3.21: Decrease in the measured cyclotron frequency of ${}^6\text{Li}$ and ${}^7\text{Li}$ due to relativistic effects as a function of $\rho_{-,ini}$. When $\rho_{-,ini}({}^7\text{Li}) = 1.12(3)$ mm and $\rho_{-,ini}({}^6\text{Li}) = 0.96(2)$ mm (circle), the shift in cyclotron frequency for ${}^6\text{Li}$ and ${}^7\text{Li}$ are similar. For the same value of $\rho_{-,ini}({}^7\text{Li})$, if $\rho_{-,ini}({}^6\text{Li}) = 1.44(2)$ mm (square), the cyclotron frequency of ${}^6\text{Li}$ shifts down by 6 ppb.

section we outline how the relativistic correction was accounted for during the ${}^6\text{Li}$ mass measurement. Prior to the ${}^6\text{Li}$ mass measurement, shifts in cyclotron frequency due to the relativistic effect have been investigated for ${}^6\text{Li}$ and ${}^7\text{Li}$ ions by varying the steering voltage ΔV_{LS} . The results are shown in figure 3.21. This figure shows the change in frequency for the two species in part-per-billion (ppb) as a function of the initial magnetron radius of the ion $\rho_{-,ini}$. The cyclotron frequencies of ${}^6\text{Li}$ and ${}^7\text{Li}$ shows a decrease with increasing $\rho_{-,ini}$ following the behaviour of equation (3.64).

Depending of the relative velocities of ${}^6\text{Li}$ and ${}^7\text{Li}$, the shift in the cyclotron frequency ratio due to relativistic effects $(\Delta R/R)_{rel.}$ is different. In order to verify the effect of different velocities for ${}^6\text{Li}$ and ${}^7\text{Li}$ in the Penning trap on $\bar{R}_{meas.}$, four independent series of ${}^6\text{Li}$ to ${}^7\text{Li}$ frequency ratio measurements were performed. Different values of ΔV_{LS} (and consequently $\rho_{-,ini}$) were chosen and the measured average frequency ratio $\bar{R}_{meas.}$ are shown in table 3.10.

The frequency ratio of data sets A-B-C all agree within error while data set D deviates by 5.5×10^{-9} . Figure 3.22 shows that this is because of

3.4. TITAN Penning trap trap-independent systematic errors

D.S.	$\rho_{-,ini}$ (${}^6\text{Li}$, ${}^7\text{Li}$) (mm)	$\overline{R}_{meas.} \times 10^6$	$\overline{R}_{rel.corr.} \times 10^6$	N
A	1.10(2), 1.20(3)	857 332.053 7(8)	857 332.054 0(17)	12
B	0.96(2), 1.12(3)	857 332.053 9(9)	857 332.054 2(15)	9
C	1.20(2), 1.20(3)	857 332.054 8(7)	857 332.054 2(17)	13
D	1.44(2), 1.12(3)	857 332.058 6(8)	857 332.053 9(19)	9
		Total	857 332.054 1(8)	43

Table 3.10: Measured mean frequency ratios $\overline{R}_{meas.}$ (and their statistical uncertainties) for different $\rho_{-,ini}$ for the four data sets (D.S.). $\overline{R}_{rel.corr.}$ are the ratios corrected for the relativistic mass increase and include both statistical and systematic errors. N is the total number of frequency ratios measured in the data set.

the large difference in velocity $\Delta\overline{\beta}c = \overline{\beta}({}^6\text{Li})c - \overline{\beta}({}^7\text{Li})c = 45(16) \times 10^{-6}$ between ${}^6\text{Li}$ and ${}^7\text{Li}$ for data set D. This large difference in velocity results in an enlarged frequency shift. However, as table 3.10 and figure 3.22 shows, once corrected using equation (3.66), the four frequency ratios agree within error.

The error on $\overline{R}_{rel.corr.}$ includes the errors on the fitting parameter a from equation (3.65) and ΔV_{LS} added quadratically to the statistical errors. Table 3.10 shows that the four corrected mean frequency ratios agrees within error. The total corrected frequency ratio $\overline{R}_{tot.rel.corr.} = 0.857\ 332\ 054\ 1(8)$ is then taken as the weighted mean of the $\overline{R}_{rel.corr.}$ from the four data sets. More information about the ${}^6\text{Li}$ mass determination is found in section 3.6.

3.4.3.2 Case study of relativistic shift at the TITAN Penning trap: ${}^6\text{He}$ and ${}^8\text{He}$

The ${}^6\text{He}$ and ${}^8\text{He}$ cyclotron frequencies are affected by relativistic effects (because of their light masses) at the level of precision for which measurements aimed for. However, the change in frequency due to relativistic effects was not measured directly prior to these measurements. Therefore, the relativistic corrections have to be evaluated from studies and simulations.

The basic idea consists of evaluating the various components of equation (3.65) and then, using equation (3.67) to calculate the relativistic relative change in the frequency ratio $(\Delta R/R)_{rel.}$ for a given steering voltage for the different species during the ${}^6\text{He}$ and ${}^8\text{He}$ measurement.

The first coefficient of equation (3.65) we calculate is the steering strength s . This quantity dictates the potential needed on the Lorentz steerer in order

3.4. TITAN Penning trap trap-independent systematic errors

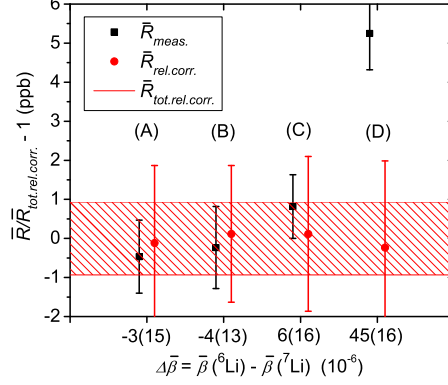


Figure 3.22: Deviation of the four $\bar{R}_{meas.}$ and $\bar{R}_{corr.}$ presented in table 3.10 with respect to $\bar{R}_{tot,rel.corr.}$, represented by the error band. The relativistic effect can be effectively corrected using Eq. (3.66) as all $\bar{R}_{corr.}$ agrees within error including the case D for which its $\bar{R}_{meas.}$ was inconsistent with the other measurement.

to provide the ion with a certain magnetron radius. The steering strength s is determined from a SIMION [Dah00] simulation. Such a simulation calculates the motion of an ion inside the electric field produced by the electrode geometry of the ion optics and through the magnetic field produced by the 3.7 T magnet. In order to determine the steering strength in such a simulation, the key parameters are the ion’s mass and its kinetic energy inside the steerer [Rin07].

The ion’s energy in the Lorentz steerer depends on its transport energy along the beam line and the potential applied on the Lorentz steerer. In theory, the transport energy of the beam between the RFQ and the Penning trap depends on the potential difference between the RFQ floating potential (HV) and the pulse drift tube (PB5) potential $E \approx \Delta V = V_{HV} - V_{PB5}$. To test this, the ion beam energy has been measured using a retarding field analyzer (see [Cha09] for more info) for various differences in applied voltage ΔV . The results are shown in the first four rows of table 3.11. Also shown are the corresponding potentials applied on the 2×45 degree benders situated between the vertical beam line section above the RFQ and the horizontal section prior to the Penning trap (see chapter 2). The acceptance of the beam through these benders is very energy sensitive and

3.4. TITAN Penning trap trap-independent systematic errors

ΔV (V)	$\Delta B1$ (V)	$E(\text{meas.})$ (eV)	FWHM (eV)
954	304	1035.8	5.6
1 028	323	1079.7	7.2
(2500)	739	2513.2	8.4
2 936	916	3050.4	8.2
ΔV (V)	$\Delta B1$ (V)	$E(\text{inter.})$ (eV)	error (eV)
1 015	N/A	1069	23
N/A	326	1098	22
ΔV (V)	$\Delta B1$ (V)	$\bar{E}(\text{inter.})$ (eV)	error (eV)
1 015	326	1084	16

Table 3.11: The first four rows gives the measured beam energy $E(\text{meas.})$ using a retarding field analyzer as a function of the potential difference ΔV between the RFQ HV bias and pulse drift tube read back voltage. For the third row, pulse drift tube was not used. The 5th and 6th rows gives the beam energy from a linear interpolation using the bending and pulse drift tube voltage. Both of these values agrees within error. The last row is a weighted average of the 5th and 6th rows.

therefore the knowledge of the bending voltage $\Delta B1$ can also help to estimate the beam energy.

All measurements were taken using the pulse drift tube, except for the third row result, shown in brackets. For this measurement, the RFQ was floated at 2.5 kV. The last column is the measured energy spread of the beam, provided for future reference. Table 3.11 shows that the only case where the relation $E \approx \Delta V$ is obeyed is when the pulse drift tube was not used. For the three other cases, the measured beam energy is larger. This indicates that the voltage outputted from the HV switch of the pulse drift tube does not correspond to the voltage delivered to it.

Therefore the beam energy used during the ${}^6\text{He}$ and ${}^8\text{He}$ measurement does not correspond to a difference in applied voltage ΔV . In order to estimate the beam energy during the measurement, we performed a linear interpolation of the ΔV versus E . A second estimate, based on the applied bending voltage, shown in figure 3.23, was also made. Both energies $E(\text{inter.})$ are given in the fifth and sixth rows of table 3.11. The two results agrees within error and their weighted mean $\bar{E}(\text{inter.})$ is given in the last row of table 3.11. Since the ion's energy in the Lorentz steerer depends also

3.4. TITAN Penning trap trap-independent systematic errors

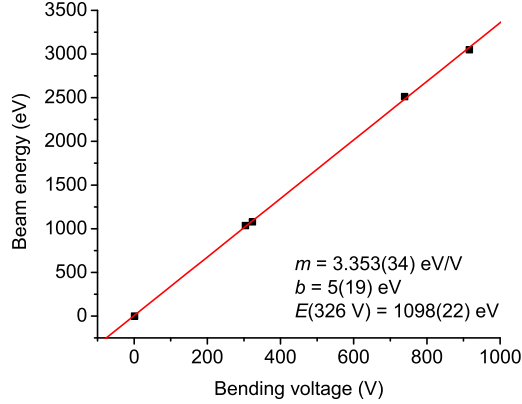


Figure 3.23: Beam energy as a function of the optimal bending voltage. Given are the slope m and y-intercept b of the linear regression as well as an estimation of the beam energy during the ${}^6\text{He}$ and ${}^8\text{He}$ mass measurement.

on the bias potential of the Lorentz steerer, we also need to take this into account in the simulation. During the experiment this potential was 955 V.

Given all these data, the steering strength s was determined for the different atomic masses measured during the experiment by changing the steering potential ΔV_{LS} and recording the radial displacement $\rho_{-,ini}$ of the ion once it reaches the Penning trap. The steering strength s is then given by a linear regression of $\rho_{-,ini}$ versus ΔV_{LS} . Table 3.12 shows the resulting steering strength s calculated for two beam energies corresponding to the lowest and highest values on $\bar{E}(\text{inter.})$. The average steering strength is simply the average value for the two energies.

The next quantity to evaluate in equation (3.65) is the constant k given by equation (3.65). Using a damping parameter $\delta \sim 1 \text{ s}^{-1}$, estimated from the theoretical line shape of time-of-flight resonance spectra, as well as the excitation time and amplitude used during the measurement, we found that $k = 0.62$.

The last quantity to evaluate is the reduced cyclotron frequency ν_+ of the various ions. This was calculated from the measured magnetron frequency of ${}^7\text{Li}$ ($\nu_- = 672.3(4) \text{ Hz}$) obtained during the ${}^6\text{He}$ and ${}^8\text{He}$ mass measurement and using equation (2.22).

We then calculated the coefficients a presented in table 3.13 using equa-

3.5. Summary of the systematic errors

A	$s(1068 \text{ eV}) (\mu\text{m}/\text{V})$	$s(1100 \text{ eV}) (\mu\text{m}/\text{V})$	$\bar{s} (\mu\text{m}/\text{V})$	$a \times 10^{-6} \text{V}^{-1}$
4	25.8	23.0	24.4(1.4)	4.5(3)
6	31.4	28.1	29.7(1.7)	3.7(2)
7	33.9	30.2	32.1(1.8)	3.4(2)
8	36.2	32.2	34.2(1.9)	3.2(2)

Table 3.12: Steering strength s obtained from simulation using the upper and lower values of the beam energy for the atomic masses of interest. \bar{s} is the average value.

A	$\Delta V_{LS} (\text{V})$	$\beta \times 10^{-5}$	$\beta_{cal.} \times 10^{-5}$	$(\Delta R/R)_{rel.} \times 10^{-9}$
4	15	6.8(4)	5.1(3)	1.0(3)
6	15	5.5(3)	5.1(3)	0.2(2)
6	23	8.4(5)	7.8(3)	0.5(5)
8	15	4.7(3)	5.1(3)	-0.2(2)
8	23	7.3(4)	7.8(3)	-0.4(5)

Table 3.13: Relative frequency ratio shift $(\Delta R/R)_{rel.}$ due to relativistic effect for singly charged ions with mass number $A = 4, 6, 8$ using a singly charged ion with mass number $A_{cal.} = 7$ for calibration. The calibration have the same steering potential as the ion of mass number A .

tion (3.67). Finally, using these coefficients and the Lorentz steering voltage ΔV_{LS} applied during the experiment, we calculated the relative frequency ratio shifts shown in table 3.13 using equation (3.66). As table 3.13 shows, the frequency ratios are mainly unaffected by the relativistic effect. This is because by giving the same steering voltage for both the ion of interest and the calibration, the two ions moves at about the same speed in the Penning trap resulting in a minimal change in the frequency ratio.

3.5 Summary of the systematic errors

We presented the different sources of systematic error on the measured cyclotron frequency arising from the imperfections of the real Penning trap, such as the magnetic field inhomogeneities, the misalignment with the magnetic field, the harmonic distortion of the trap potential and the non-harmonic terms in the trapping potential. We also presented trap-independent sys-

3.6. Benchmark high-precision mass measurement at TITAN Penning trap: ${}^6\text{Li}$

tematic errors such as the error due to the interaction of multiple ions in the trap, the magnetic field time-fluctuations and the error due to relativistic effects. Table 3.14 summarize the various sources of systematic errors

Error	$\Delta R/R (\times 10^{-10})$
Magnetic field inhomogeneities	$0.2 \cdot \Delta A$
Misalignment and harm. distort.	$42 \cdot \Delta A$
Incomplete compensation	$5(5) \cdot \Delta A$
Non-lin. mag. fluct.	$1.5 \cdot \Delta t$

Table 3.14: Sources of systematic errors on the frequency ratio measurement arising from imperfections of TITAN’s Penning trap. $\Delta A = A_{cal.} - A$ is the mass difference between the calibration and ion of interest. Δt is the time span between two calibrations in hours.

discussed and their size. All the estimated errors are for a trap with $V_0 = 36$ V. The largest source of error comes from the conservative estimate of the misalignment with the Penning trap with the magnetic field. All these systematic errors depend on the mass number difference ΔA , which means that when the mass measurement is performed using a calibrant and species of the same mass number, the shift on the frequency ratio will be effectively quenched. The error due to the number of ions in the trap are not shown as they are species-dependent. For the magnitude of this error for the ${}^6\text{Li}$, ${}^6\text{He}$ and ${}^8\text{He}$ measurements, refer to section 3.4.2. The error due to relativistic effects is not shown as its dependance on several factors such as the beam energy, the masses involved and their relative steering voltages. For the calculations of this source of error for the ${}^6\text{Li}$ measurement, refer to section 3.4.3.1 and for the ${}^6\text{He}$ and ${}^8\text{He}$ measurement, refer to section 3.4.3.2.

3.6 Benchmark high-precision mass measurement at TITAN Penning trap: ${}^6\text{Li}$

Precise and accurate stable masses are important in nuclear physics because of their use as calibrants for mass measurements on radioactive species. One example is ${}^6\text{Li}$, which is the calibration mass used for the mass measurement of the radio-active nuclei ${}^8\text{He}$ [Ryj08], ${}^8\text{Li}$, ${}^9\text{Li}$ and ${}^{11}\text{Li}$ [Smi08b] by the TITAN experiment.

A recent Penning trap mass measurement of ${}^6\text{Li}$ by SMILETRAP [Nag06] shows a disagreement of 5σ with the AME03 value [Aud03]. The AME03

3.6. Benchmark high-precision mass measurement at TITAN Penning trap: ${}^6\text{Li}$

value is based entirely on a Penning trap measurement from the JILATRAP Penning trap experiment [Hea01]. Such a discrepancy needs to be resolved before mass measurements on unstable ions can be performed to a level of precision below 10^{-8} using ${}^6\text{Li}$ as a calibration species. To do so, the mass of ${}^6\text{Li}$ has been measured at the TITAN facility using ${}^7\text{Li}$ as a calibrant, which has a relative uncertainty of only $\delta m/m = 6 \times 10^{-10}$ [Nag06].

In this section we present the mass measurement of ${}^6\text{Li}$. This is the first stable mass measured at the TITAN facility and it represents a test case regarding the precision achievable by the mass spectrometer.

3.6.1 The ${}^6\text{Li}$ mass measurement

The ${}^6\text{Li}$ mass measurement was carried out in May 2009 after the detailed systematic studies of the TITAN Penning trap had been completed. Both ${}^6\text{Li}$ and its calibrant ${}^7\text{Li}$ were produced by the TITAN off-line ion source, transported at an energy of 2 keV and non-isobaric contamination was filtered out using the time-of-flight gate. The injection and capturing of the beam has been carefully optimized prior to the measurement. Four series of measurements were taken, each lasting approximately 12 hours. Both species were excited for 997 ms to reach the required precision on the measurement. To minimize possible shifts due to time-dependent variation of the magnetic field, each TOF spectrum measurement lasted 30 minutes and each ${}^6\text{Li}$ measurement was bracketed between two ${}^7\text{Li}$ measurements.

Figure 2.15 shows a ${}^6\text{Li}$ resonance taken during the measurement together with a fit of the theoretical function given by equation (2.45). The different sources of systematic error in the determination of the frequency ratios were investigated prior to the measurement and summarized in section 3.5.

$\overline{R}_{tot.rel.corr.}$	0.857 332 054 1(8)
$\overline{R}_{mas.corr.}$	0.857 332 053 6(9)
\overline{R}_{final}	0.857 332 053 6(37)

Table 3.15: Weighted mean of these corrected frequency ratios $\overline{R}_{tot.rel.corr.}$, frequency ratio once corrected for the incomplete compensation of the trapping potential $\overline{R}_{mas.corr.}$ and final frequency ratio of ${}^6\text{Li}$ versus ${}^7\text{Li}$.

The frequency ratios of the four series of measurements are corrected for relativistic effects as presented in section 3.4.3.1. The weighted mean of these corrected frequency ratios $\overline{R}_{tot.rel.corr.}$ is presented in table 3.15. This

3.6. Benchmark high-precision mass measurement at TITAN Penning trap: ${}^6\text{Li}$

Error	$\Delta R/R \times 10^{-9}$
Relativistic and statistical	1.0
Compensation	0.4
Ion-ion interaction	0.2
Nonlinear B -field fluct.	0.2
Misalignment and harm. distort.	4.2
Total	4.3

Table 3.16: Error budget for the frequency ratio measurement \overline{R}_{final} which includes the different causes of error discussed in the text.

table shows the frequency ratio $\overline{R}_{mas.corr.}$ once corrected for the incomplete compensation of the trapping potential. The most dominant sources of uncertainty are presented in table 3.16 together with the statistical uncertainty and the uncertainty due to the incomplete compensation. The other systematic effects include the error due to the interaction of multiple ions in the trap and the error due to the non-linear fluctuations of the magnetic field. The dominant source of uncertainty, of 4.2×10^{-9} , comes from the estimate of the misalignment of the trap with the magnetic field axis. All other sources of uncertainty are below the 10^{-9} range. Table 3.15 presents the final frequency ratio \overline{R}_{final} including all the sources of uncertainties.

Using equation (2.49), the ${}^7\text{Li}$ mass $m({}^7\text{Li}) = 7.016\,003\,425\,6(45)$ u (1 u = $931\,494.009$ keV in natural units) and including the first electron ionization energy of Li [Lor82], the ${}^6\text{Li}$ mass measured by TITAN is $m({}^6\text{Li}) = 6.015\,122\,889(26)$ u with a corresponding mass excess of $\text{ME}({}^6\text{Li}) = 14\,086.881(25)$ keV. Figure 3.24 shows that this new ${}^6\text{Li}$ mass confirms the SMILETRAP mass value $m(\text{SMILE}) = 6\,015\,122.890(40)$ u [Nag06] while improving the precision by a factor of 1.5.

3.6. Benchmark high-precision mass measurement at TITAN Penning trap: ${}^6\text{Li}$

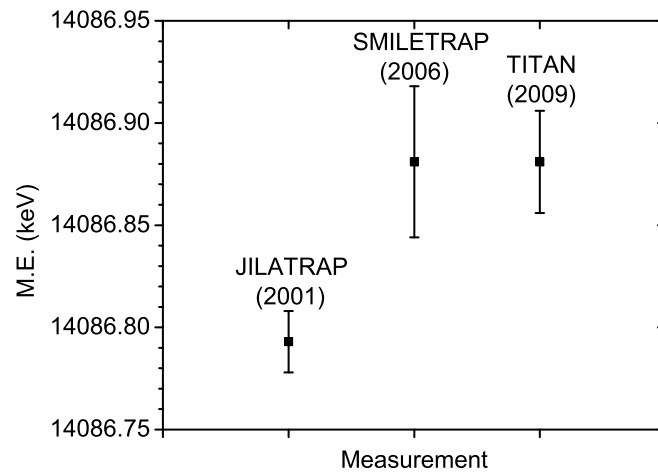


Figure 3.24: ${}^6\text{Li}$ mass excess as measured by the JILATRAP [Hea01], SMILETRAP [Nag06] groups and the present work. The TITAN value is in good agreement with [Nag06].

Chapter 4

${}^6\text{He}$ and ${}^8\text{He}$ mass measurement results and discussion

Halo nuclei are a well-suited test-bench for nuclear ab-initio methods. This is because the extreme properties of halo nuclei, such as their low valence neutron separation energies and large difference in matter and charge radii are a challenge for theory. Testing ab-initio methods against charge radii, binding energies and two-neutron separation energies derived from the TITAN masses gives us a chance to reveal strengths and weaknesses of the different methods and also motivate improvements from the theory side.

This chapter presents the results of the mass measurements of the halo nuclei ${}^6\text{He}$ and ${}^8\text{He}$ using the TITAN Penning trap. To compare our results to theory, we use the TITAN masses to obtain new charge radius values. The more precise and accurate mass removes the atomic mass as a sources of systematic error on the charge radius determination. These new charge radii and masses are then used to test nuclear theories based on ab-initio methods.

4.1 First ${}^8\text{He}$ mass measurement

The first ${}^8\text{He}$ mass measurement at TITAN was carried out in November 2007. The ${}^8\text{He}$ were produced using 500 MeV protons from the TRIUMF cyclotron at a current of 20 μA hitting a high power silicon-carbide target. The beam was ionized using the FEBIAD ion source (see section 2.1). The beam was transported at an energy of 20 keV and cooled with hydrogen in the RFQ. The ${}^6\text{Li}$ used as calibrant was produced by the TITAN off-line ion source. A ${}^{20}\text{Ne}$ pilot beam was used to tune through the RFQ yielding a 57 % transmission efficiency. The ${}^8\text{He}$ yield measured at the yield station was 3100 counts/s. Thus, because of this low incoming count rate, each ${}^8\text{He}$ time-of-flight measurement took 68 minutes. The count rate on the time-of-

4.1. First ^8He mass measurement

flight detector was three ^8He ions per minute. ^8He was excited for 90 ms, while the ^6Li was excited for 400 ms.

This first mass measurement of ^8He is based on three ^8He resonance curves, each bracketed by ^6Li resonance curves. Table 4.1 shows the three

Isotope	$R \times 10^6$	N
^8He	1.335 653 449 (90)	201
^8He	1.335 653 711 (120)	192
^8He	1.335 653 447 (80)	220
Mean	1.335 653 480 (54)(107)	613

Table 4.1: Measured cyclotron frequency ratios $R = \nu_c(^6\text{Li})/\nu_c(^8\text{He})$ for ^8He using ^6Li as calibration. N is the number of measurement in each series. Also shown is the weighted mean of these frequency ratios. The first number in parentheses represent the statistical uncertainty and the second number the systematic uncertainty.

corresponding frequency ratios as well as their weighted mean.

After the ^8He mass measurement, it was found that the cyclotron frequency of the ion changes with the repetition rate leading to a shift in the frequency ratio when the calibration and the ion of interest cyclotron frequencies are measured using different repetition rates. This effect has been investigated and found to be due to a repetition rate-dependant change of the beam energy coming from the RFQ. As changes in the cyclotron frequency of 8×10^{-8} were found during these studies, this was the largest source of systematic error for this measurement. This systematic uncertainty is given by the second number in parentheses for the weighted mean value of the frequency ratio shown in table 4.1.

Experiment	$m(^6\text{Li})$ (u)	$\Delta(^6\text{Li})$ (keV)
SMILETRAP	6.015122891(40)	14086.882(37)
TITAN	6.015122889(26)	14086.881(25)
Average	6.015122890(22)	14086.881(20)

Table 4.2: ^6Li masses m and mass excess Δ as determined from the frequency ratios measured by SMILETRAP [Nag06] and TITAN experiment [Bro09].

Using the weighted mean of the TITAN ^6Li mass measurement and the

4.2. Second ^8He and the ^6He mass measurements

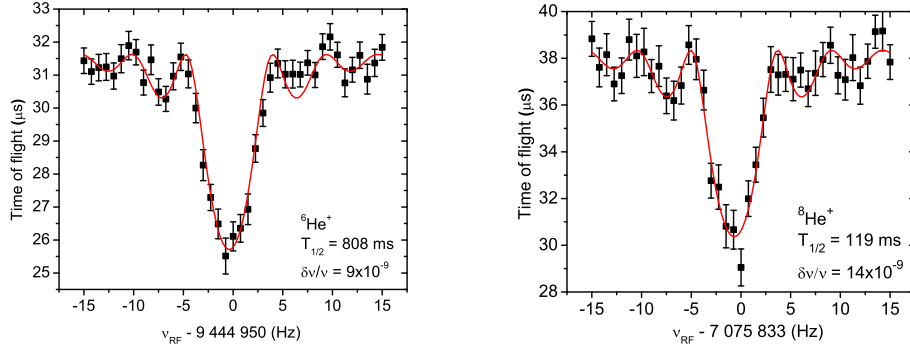


Figure 4.1: ^6He (left) and ^8He (right) time-of-flight resonance spectra. Also shown are the half-life of these species and the relative statistical uncertainty on the fitted cyclotron frequency.

value from [Nag06] as ^6Li mass (see table 4.2) and using equation (2.49), we determined the ^8He mass as 8.033 935 669(722) u with a corresponding mass excess of 31 610.872(673) keV. This is within the given error bar but is 110 eV more massive than the result presented in [Ryj08], which used a ^6Li mass based on the weighted mean of the masses from [Nag06] and [Hea01].

4.2 Second ^8He and the ^6He mass measurements

A ^6He and a second ^8He mass measurement was performed in May and June 2008. The beam was produced and ionized using the same technique as for the first ^8He mass measurement, except a higher proton current of 80 μA was used. The cyclotron frequency measurements performed in May were done with a 37 keV beam energy, while the beam energy in June was 20 keV. Similar transmission efficiency of the ^{20}Ne pilot beam through the RFQ as for the first ^8He mass measurements were seen.

This series of measurements includes 12 ^6He and 17 ^8He frequency ratios determination using ^7Li as the calibrant. Time-of-flight resonance spectra of both species are shown in figure 4.1. All the measurements are shown in figure 4.2 and sorted according to the Lorentz steerer voltage used in order to apply different relativistic corrections on them. This is because different steering voltages lead to a change of the ion velocity in the trap and therefore different relativistic effect. The first four ^8He measurements with Lorentz

4.2. Second ^8He and the ^6He mass measurements

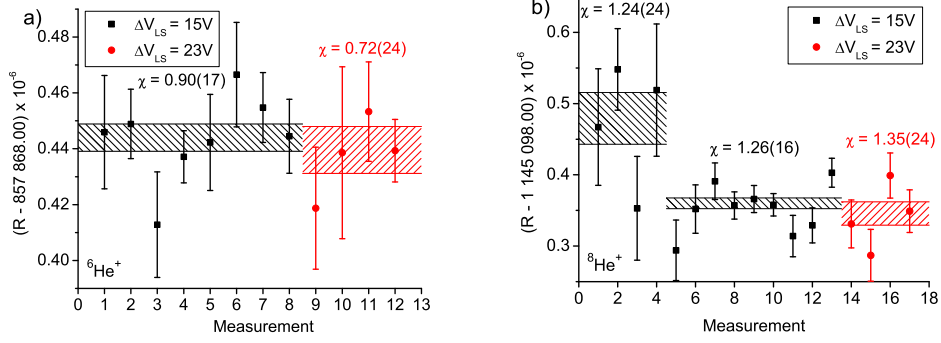


Figure 4.2: ^6He (a) and ^8He (b) frequencies ratio R measurements.

steering voltage $\Delta V_{LS} = 15\text{V}$ are treated separately as they were performed in non-optimal conditions. The bands represents the one sigma statistical uncertainty on the weighted mean of the frequency ratios in the data set.

In order to test the consistency of the data, we calculated the Birge ratio χ [Bir32]:

$$\chi = \sqrt{\frac{1}{N-1} \sum_{i=1}^N \left(\frac{R_i - \bar{R}}{\sigma R_i} \right)^2}, \quad (4.1)$$

where N is the number of frequency ratio measurements, R_i are the individual frequency ratios and \bar{R} is their weighted mean. The uncertainty on the Birge ratio is given by $0.4769/\sqrt{N}$ [Bir32]. A Birge ratio of one means that the fluctuations are purely statistical, if it is greater than one it means that there could be systematic effect present that are not accounted for, while a Birge ratio smaller than one indicates that the uncertainties could be overestimated. The Birge ratios of the various data sets are shown figure 4.2. The $\Delta V_{LS} = 15\text{V}$ ^6He data set has a Birge ratio in agreement with one, while the second data set is slightly below one. The ^8He data have a larger scatter than the ^6He data, which is shown by its Birge ratios that are slightly above one. Note that the weighted mean of the all the $\Delta V_{LS} = 15\text{V}$ ^8He data, including the first four measurements, gives a Birge ratio of 1.52(13), which is clearly above one. This is one indication that the first four measurements should be treated differently.

The pressure in the chamber during these measurements was 4.6×10^{-9} torr, which is considerably higher than the typical 1.9×10^{-9} torr seen for the other measurements. This poorer vacuum was due to higher tem-

4.2. Second ^8He and the ^6He mass measurements

perature in the experimental hall. Large temperature changes have shown to affect the output potential of the power supply providing the potential for the pulse drift tube after the RFQ. As this drift tube determines the energy of the beam entering the Penning trap, the injection condition for these measurements could have been non-optimal. In fact, the number of recorded counts for the three ^7Li calibration time-of-flight resonance spectra taken during these measurements decreased from 10 390 down to 1 287. After these measurements, we realized that the power supply of some optics element between the RFQ and Penning trap had tripped off probably due to over-heat. This could have resulted in a different beam injection in the Penning trap and a consequent change in frequency. As we discussed in section 4.1, the largest change in cyclotron frequency due to non-optimal conditions found from previous studies is 8×10^{-8} . Therefore, we assigned this conservative value as systematic uncertainty on the averaged frequency ratio of the first four measurements.

In order to test the accuracy of the Penning trap, the frequency ratio of 23 ^6Li and 5 ^4He using ^7Li calibration were measured and their masses are compared with the literature values at the end of the analysis. Table 4.3

Isotope	ΔV_{LS} (V)	$\overline{R}_{meas.} \times 10^6$	N
^4He	15	570 462.612 3(15)	5
^6Li	15	857 332.055 4(27)	4
^6Li	23	857 332.050 8(12)	19
^6He	15	857 868.444 0(51)	8
^6He	15	857 868.439 6(84)	4
$^8\text{He}^*$	15	1 145 098.479 3(363)	4
^8He	15	1 145 098.360 0(75)	9
^8He	23	1 145 098.345 6(164)	4

Table 4.3: Mean measured cyclotron frequency ratios $\overline{R}_{meas.}$ for ^4He , ^6Li , ^6He and ^8He using ^7Li for calibration. The $\overline{R}_{meas.}$ are sorted according to the correction tube V_{TUBE} and Lorentz steering ΔV_{LS} voltage used. N is the number of measurements in each series. The errors are purely statistical.

gives the weighted mean of the ^4He , ^6Li , ^6He and ^8He to ^7Li frequency ratios, sorted according to the Lorentz steerer voltage used during the measurement. The star (*) denotes the ^8He measurement series taken in non-optimal condition.

The relativistic effects are not the dominant sources of systematic error

4.2. Second ^8He and the ^6He mass measurements

on the measurements. In fact, the main sources of systematic errors on

Error	$\Delta R/R \times 10^{-9}$ (^6He)	$\Delta R/R \times 10^{-9}$ (^8He)
Statistical	4.9	5.9
Ion-ion interaction	8.1	13.3
Total	9.4	14.6

Table 4.4: Error budget for the frequency ratio measurement \bar{R}_{final} for $^6,^8\text{He}$, which includes the statistical error and the error due to the interaction of multiple ions in the trap.

the ^6He and ^8He cyclotron frequency ratios comes from the interaction of multiple ions in the trap as shown in table 4.4. The contribution from the other effects are all below the 10^{-9} level and therefore have a negligible contribution to the final uncertainty.

Lastly, we checked the accuracy of the Penning trap by measuring the frequency ratios of ^4He to ^7Li and ^6Li to ^7Li . Using these frequency ratios, presented in table 4.3 and equation (2.49), we evaluated the mass of ^4He and ^6Li and compared it with the values from the literature ([Aud03] for ^4He and table 4.2 for ^6Li). Table 4.5 gives the difference $\delta\Delta = \Delta(\text{TITAN}) - \Delta(\text{lit.})$

Isotope	$\Delta(\text{TITAN})$ (keV)	$\Delta(\text{lit.})$ (keV)	$\delta\Delta$ (eV)
^4He	2 424.915(18)	2 424.915 65(6)	-1(18)
^6Li	14 086.867(9)	14 086.881(20)	-14(22)

Table 4.5: Difference between TITAN’s and the literature mass excesses Δ . The literature M.E. for ^4He and ^{24}Mg are from [Aud03], while for ^6Li we took the weighted mean of the values from [Nag06] and [Bro09].

between the mass excess measured by TITAN during this experiment and the literature mass excess. The error on this difference is taken as the error of the TITAN and literature mass excess added in quadrature. These differences are all within error, which shows that there is a good agreement between the stable masses measured during the ^6He and ^8He mass measurement and the values from the literature. This is an indication that the systematic errors have not been under-estimated. This leads to the final frequency ratios \bar{R}_{final} shown in table 4.6. Using the \bar{R}_{final} presented in table 4.6 together with equation (2.49), we evaluated the masses of $^6,^8\text{He}$ and the results are shown in table 4.7. The table compares the latest ^8He measurement with

4.3. Calculation of the binding energy and point-proton radius for ${}^6\text{He}$ and ${}^8\text{He}$

Isotope	$\overline{R}_{final} \times 10^6$	$\delta R/R$ (ppb)
${}^6\text{He}$	857 868.442 9(82)	9.5
${}^8\text{He}^*$	1 145 098.479 2(997)	87.1
${}^8\text{He}$	1 145 098.357 4(167)	14.6
${}^8\text{He}$ (average)	1 145 098.360 7(164)	14.4

Table 4.6: Mean corrected cyclotron frequency ratios \overline{R}_{final} of ${}^6,{}^8\text{He}$, together with the relative uncertainty on these ratios.

Isotope	mass ($\times 10^6$ u)	M.E. (keV)
${}^6\text{He}$	6 018 885.883(38)	17 592.087(35)
${}^8\text{He}$ (1^{st})	8 033 935.669(722)	31 610.872(673)
${}^8\text{He}$ (2^{nd})	8 033 934.404(115)	31 609.694(107)
${}^8\text{He}$ (average)	8 033 934.435(114)	31 609.723(106)

Table 4.7: Masses and mass excesses of ${}^6,{}^8\text{He}$. Both the first and second mass determination of ${}^8\text{He}$ are shown. Also shown is the weighted mean of the two ${}^8\text{He}$ masses.

the published one [Ryj08]. Both results agree within two sigma.

4.3 Calculation of the binding energy and point-proton radius for ${}^6\text{He}$ and ${}^8\text{He}$

In this section, we calculate the charge radius, point-proton radius, two neutron separation energy and binding energy of ${}^6\text{He}$ and ${}^8\text{He}$. The last three quantities are used to compare with theory.

The binding energies are compared in order to investigate any possible systematic difference between the predicted binding energies and the experimental ones.

The reason for a comparison of the predicted two-neutron separation energy S_{2N} with the measured values is the following: ${}^6\text{He}$ and ${}^8\text{He}$ are bound if they have a $S_{2N} > 0$. Then, using the two-neutron separation energy, the prediction of a bound or unbound state for an ab-initio method can easily be checked. When the values from theory are available, the two-

4.3. Calculation of the binding energy and point-proton radius for ${}^6\text{He}$ and ${}^8\text{He}$

neutrons separation energy of the ab-initio method is calculated:

$$S_{2N}({}^{6,8}\text{He}) = E_B^{\text{pred.}}({}^{4,6}\text{He}) - E_B^{\text{pred.}}({}^{6,8}\text{He}) \quad (4.2)$$

where $E_B^{\text{pred.}}$ are the predicted binding energies.

The point-proton radius is calculated in order to compare the measured charge radius with the ab-initio prediction. These methods assume that the protons and neutrons are point-like particles. As the charge radius obtained experimentally includes the physical extent of the proton and neutrons, it needs to be adjusted.

4.3.1 Binding and two-neutron separation energy of ${}^{6,8}\text{He}$

The binding energy of a nucleus is the energy necessary to break the nucleus into individual proton and neutrons, while the two-neutron separation energy is the energy necessary to remove two neutrons from the nucleus. Table 4.8 gives the ${}^{6,8}\text{He}$ binding energies E_B :

Isotope	E_B (keV)	S_{2N} (keV)
${}^6\text{He}$	-29 271.123(35)	975.46(19)
${}^8\text{He}$	-31 396.155(59)	2125.03(25)

Table 4.8: Binding energies E_B and two-neutrons separation energies S_{2N} of ${}^{6,8}\text{He}$ using TITAN's mass excesses and the AME03 ${}^4\text{He}$ mass excess.

$$E_B(N, Z) = m(N, Z) - Zm_H - Nm_n \quad (4.3)$$

where m_H is the hydrogen mass, m is the atomic mass, m_n the neutron mass and Z , N , the number of protons and neutrons in the nucleus. Table 4.8 also gives the two-neutron separation energies S_{2N} calculated using equation (4.2). The two-neutron separation energy of ${}^6\text{He}$ is calculated using the ${}^4\text{He}$ mass from the AME03 [Aud03].

4.3.2 Charge and point-proton radius of ${}^{6,8}\text{He}$

The nuclear charge radius is defined as

$$\langle r_c^2 \rangle = \frac{1}{Ze} \int r^2 \rho(r) d^3r \quad (4.4)$$

4.3. Calculation of the binding energy and point-proton radius for ${}^6\text{He}$ and ${}^8\text{He}$

where Z is the nuclear charge, e the elementary charge, r the radial distance from the nucleus centre and ρ is the radial charge density. From equation (4.4), it can be seen that the charge radius is a measure of the extent of the charge distribution in the nucleus and hence the proton distribution. As described in section 1.1.2.4, it can be determined using a combination of isotopic shift measurements and atomic physics calculations.

Transition	$\delta\nu_{MS}^{A,4}(\text{AME03})$	$\delta\nu_{MS}^{A,4}(\text{TITAN})$
${}^6\text{He } 2^3\text{S}_1 \rightarrow 3^3\text{P}_0$	43 196.204(15)	43 196.1573(8)
${}^6\text{He } 2^3\text{S}_1 \rightarrow 3^3\text{P}_1$	43 195.943(15)	43 195.8966(8)
${}^6\text{He } 2^3\text{S}_1 \rightarrow 3^3\text{P}_2$	43 196.217(15)	43 196.1706(8)
${}^8\text{He } 2^3\text{S}_1 \rightarrow 3^3\text{P}_1$	64 701.999(74)	64 702.0982(9)
${}^8\text{He } 2^3\text{S}_1 \rightarrow 3^3\text{P}_2$	64 702.409(74)	64 702.5086(9)

Table 4.9: Mass shift $\delta\nu_{MS}^{A,4}$ term for ${}^6,8\text{He}$ using AME03 [Aud03] and TITAN masses.

The charge radii $\langle r_c^2 \rangle^{1/2}$ are calculated using

$$\langle r_c^2 \rangle^A = \langle r_c^2 \rangle^4 + \frac{\delta\nu^{A,4} - \delta\nu_{MS}^{A,4}}{K_{FS}}, \quad (4.5)$$

where $\langle r_c^2 \rangle^4$ is the mean-square charge radius of ${}^4\text{He}$. The mass is relevant for the calculation of the mass shift $\delta\nu_{MS}^{A,4}$. Table 4.9 shows that the new mass values improved the precision of $\delta\nu_{MS}^{A,4}$ by a factor of almost 20 for ${}^6\text{He}$ and over 80 for ${}^8\text{He}$. This makes the nuclear mass uncertainty a negligible factor in the charge radii uncertainty for ${}^6\text{He}$ and ${}^8\text{He}$ and leads to an improved precision of 9% for ${}^6\text{He}$ and 36% for ${}^8\text{He}$.

The point-proton radius $\langle r^2 \rangle_{pp}^{1/2}$ is defined as the expectation value of the proton's position vector squared and can be calculated from the charge radius using

$$\langle r^2 \rangle_{pp} = \langle r^2 \rangle_c - \langle R_p^2 \rangle - \frac{N}{Z} \langle R_n^2 \rangle - \frac{3}{4M_p^2} \quad (4.6)$$

where $\langle R_p^2 \rangle = 0.769(12) \text{ fm}^2$ and $\langle R_n^2 \rangle = -0.1161(22) \text{ fm}^2$ are the proton and neutron mean square radii [Yao06] and $\frac{3}{4M_p^2} = 0.033 \text{ fm}^2$ is a first-order relativistic correction called Darwin-Foldy term [Fri97]. The negative value for the neutron charge radius is caused by the negative charge distribution of the neutron at larger distance from the neutron centre [Kop97].

4.4. Comparison of the results for ${}^{6,8}\text{He}$ with theory

Isotope	$\langle r^2 \rangle_c^{1/2}$ (AME03)	$\langle r^2 \rangle_c^{1/2}$ (TITAN)	$\langle r^2 \rangle_{pp}^{1/2}$ (TITAN)
${}^6\text{He}$	2.068(11)	2.056(10)	1.913(9)
${}^8\text{He}$	1.929(26)	1.955(18)	1.835(18)

Table 4.10: New charge $\langle r^2 \rangle_c^{1/2}$ and point-proton $\langle r^2 \rangle_{pp}^{1/2}$ radii in fm, of ${}^{6,8}\text{He}$ using TITAN masses.

Table 4.10 shows the charge and point-proton radii of ${}^{6,8}\text{He}$, calculated using equation (4.5) and (4.6) and taking into account other sources of uncertainty in the isotopic shift measurement [Mue07]. The ${}^8\text{He}$ TITAN mass improved the precision of the charge radius uncertainty of that nuclei by 36% while increasing its value by 0.026 fm (1.3%) due to the 11.7 keV change in the mass value. Because of the better precision on the ${}^6\text{He}$ mass value in the AME03 [Aud03], the improvement of the charge radius from the TITAN mass is smaller, but the 3 keV difference modifies the charge radius by 0.012 fm (0.6%). Therefore the new mass values from TITAN led to a reduction of the difference in charge radii between ${}^{6,8}\text{He}$ by 0.04(3) fm.

4.4 Comparison of the results for ${}^{6,8}\text{He}$ with theory

In this section, the achieved results are compared to theoretical predictions, in particular key features are tested, such as the ${}^6\text{He}$ and ${}^8\text{He}$ point-proton radii, binding energies and two-neutrons separation energies. The values are directly or indirectly derived from the TITAN mass measurement and compared to results from the ab-initio methods described in section 1.2. The purpose of this exercise is to address and determine the predictive powers of the various models by comparing their output results with sensitive quantities for two different halo nuclei.

Figure 4.3 shows the binding energies predictions for ${}^6\text{He}$ and ${}^8\text{He}$ from Green Function Monte Carlo (GFMC), using the AV18 two-body potential and the Illinois-2 three body potential [Pie04], the No-Core Shell Model (NCSM) using the CD-Bonn 2000 and INOY potentials [Cau06] and the No-Core Full Configuration (NCFC) using a JISP16 potential [Mar09]. Also, we show results from Hyperspherical Harmonics (HH) and Coupled Cluster theory (CC) that uses a chiral V_{lowk} potential [Bac09a]. As the error bars are not visible for the experimental binding energies at this scale, they are

4.4. Comparison of the results for ${}^6,8\text{He}$ with theory

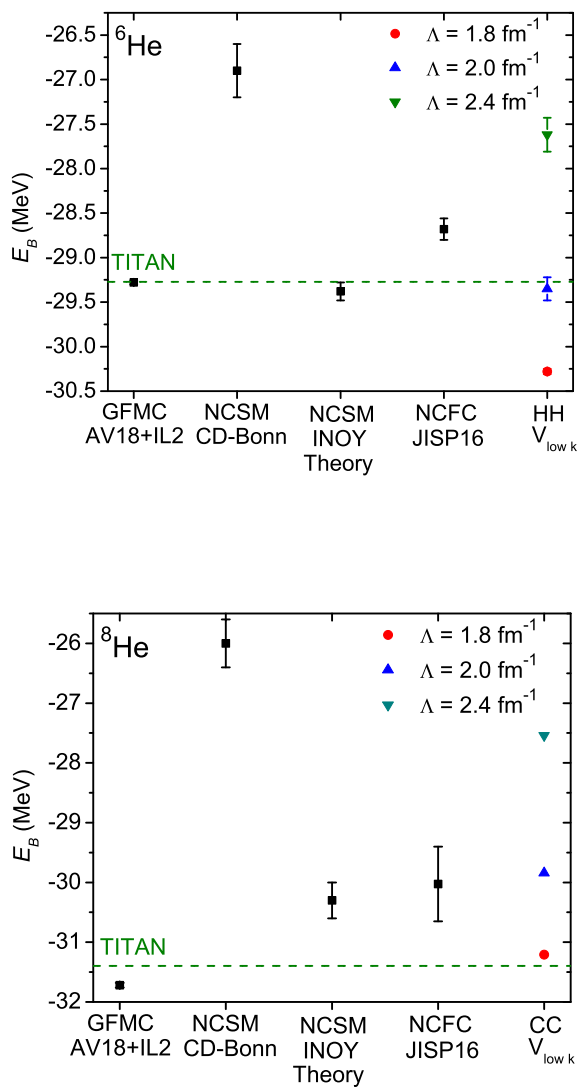


Figure 4.3: Binding energies E_B of from various ab-initio methods for ${}^6\text{He}$ and ${}^8\text{He}$ compared to the TITAN value shown by the dashed line. See text for more details.

represented by a straight line.

Figure 4.4 shows the two-neutron separation energy predictions for ${}^6\text{He}$ and ${}^8\text{He}$ from the same methods and using the same potentials as for the binding energies presented in figure 4.3. There are no CC results shown as calculations results for ${}^6\text{He}$ are not reliable within this theory [Hag07a].

Figure 4.5 shows the point-proton radius of ${}^6\text{He}$ and ${}^8\text{He}$ for GFMC [Pie05], NCSM [Cau06] and preliminary HH and CC [Bac09b] results. Results from NCFC are not found in literature. Also shown are the matter radius obtained from nuclear scattering experiments. These values are used for comparison with the model predictions. The error on the matter radius of ${}^6\text{He}$ and ${}^8\text{He}$ is conservatively taken as the outer error from the three experiments [Kis05, Tan92, Alk97] shown in figure 4.5.

4.4.1 Green Function Monte-Carlo results for ${}^6\text{He}$ and ${}^8\text{He}$

The Green Function Monte-Carlo (GFMC) (see section 1.2.2.1) is the only method that calculated properties of ${}^6\text{He}$ and ${}^8\text{He}$ using three-nucleon interaction. The parameters of the three-body potential Illinois were obtained by fitting the binding energies of nuclei with mass numbers $3 \geq A \geq 8$, including ${}^6\text{He}$ and ${}^8\text{He}$. Hence one would expect to have a good agreement with the measured binding energies. The binding energy of ${}^6\text{He}$ calculated using GFMC agrees within error with the TITAN value. On the other hand, the binding energy of ${}^8\text{He}$ is 320 ± 40 keV more bound than the TITAN value, which corresponds to a 8σ deviation. However, in absolute value, the GFMC results are the closest to experiment. Concerning the ${}^6\text{He}$ two-neutron separation energy, the GFMC presents larger deviations with the TITAN values and this is due to their ${}^4\text{He}$ over-binding by 70(30) keV. Their ${}^8\text{He}$ two-neutron separation energy is 8σ away from the TITAN value, just as the binding energy.

For the point-proton radius, GFMC calculations are difficult because of the small two-neutrons separation energies of ${}^6\text{He}$ and ${}^8\text{He}$ [Pie07]. Changes in the trial wave function Ψ_{trial} and other parameters can result in changes in the two-neutron separation energy of 200-400 keV. Because of the strong sensitivity of the point-proton radius on the two-neutron separation energy, this can result in a large radius as S_{2N} approaches zero. As a solution, the two-neutron separation energy and point-proton radius of ${}^6\text{He}$ and ${}^8\text{He}$ were calculated using different Illinois potentials and also by varying the parameters of these potentials. Figure 4.6 shows that the results all fall within a certain band that includes the experimental values. Then, from the results of Figure 4.6, the point-proton radius for both ${}^{6,8}\text{He}$ were calculated

4.4. Comparison of the results for ${}^6\text{He}$ and ${}^8\text{He}$ with theory

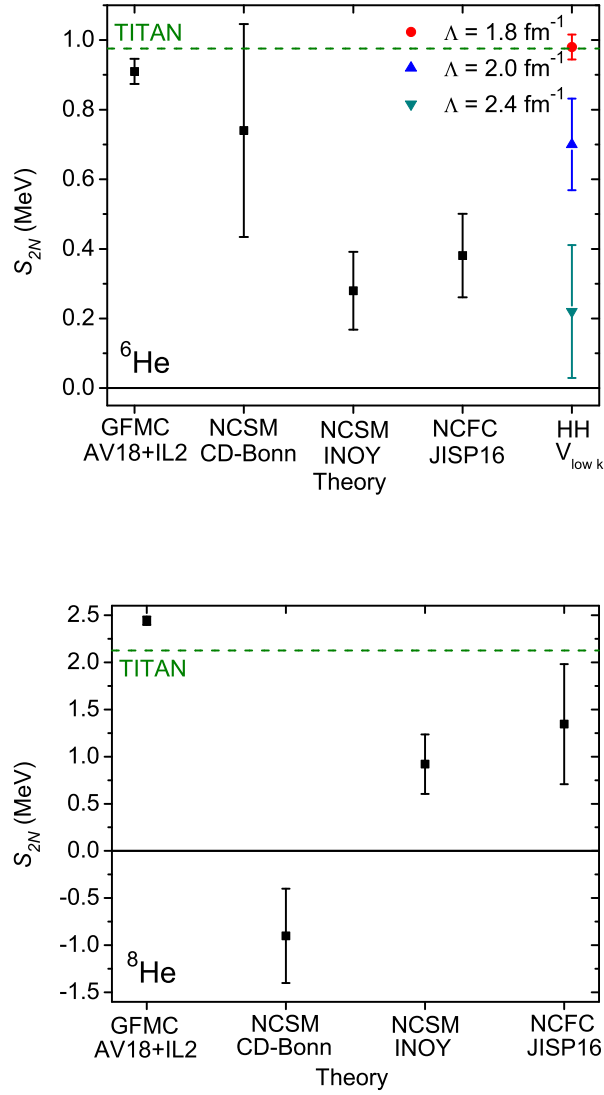


Figure 4.4: Two-neutron separation energies S_{2N} of from various ab-initio methods for ${}^6\text{He}$ and ${}^8\text{He}$ compared to the TITAN value shown by the dashed line. S_{2N} values below zero describe an unbound nucleus. See text for more details.

4.4. Comparison of the results for ${}^6,8\text{He}$ with theory

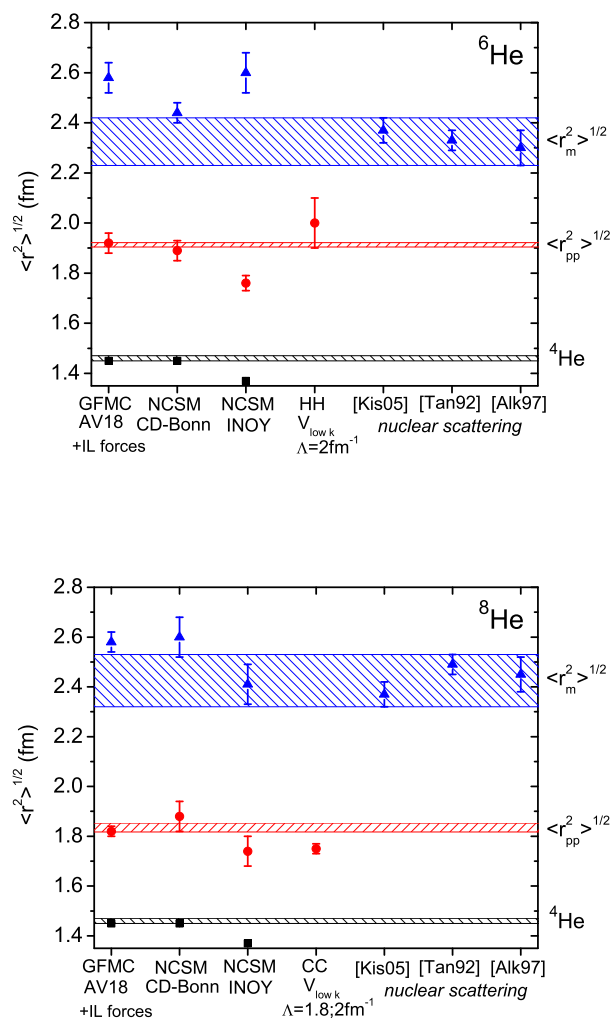


Figure 4.5: rms point-proton and matter radius of various ab-initio methods compared with the experimental data. See text for more details.

4.4. Comparison of the results for ${}^{6,8}\text{He}$ with theory

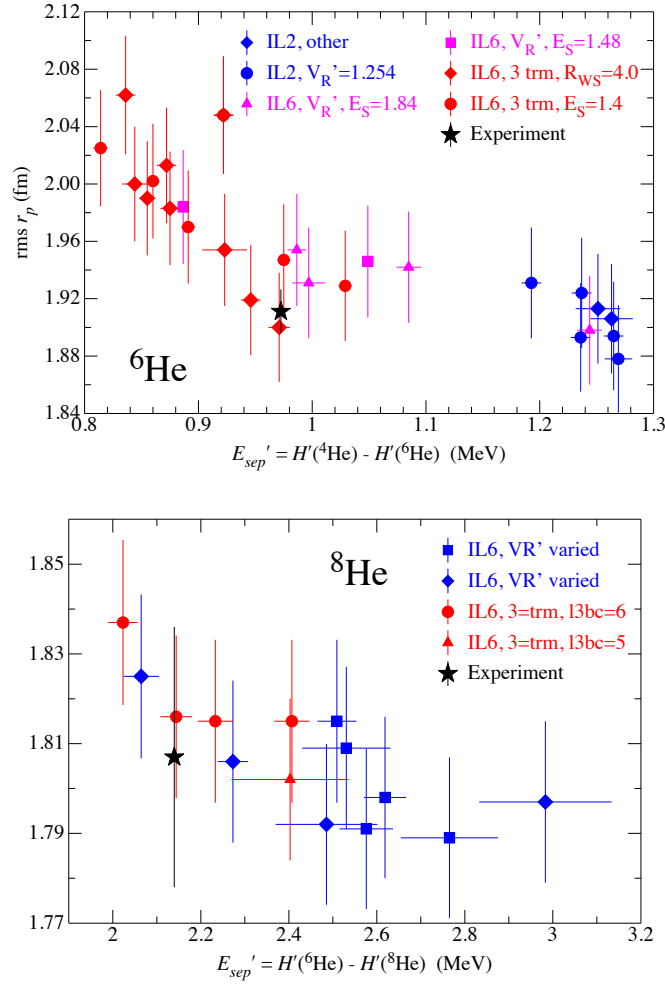


Figure 4.6: Point-proton radius r_p for ${}^6\text{He}$ (top) and ${}^8\text{He}$ (bottom) as a function of the two-neutrons separation energy (E'_{sep}) for various modified Illinois interactions. The star shows the experimental values from [Mue07]. Figure from [Pie07].

leading to results that agree within error with the experimental values. The matter radii of ${}^6,8\text{He}$, however, are both larger than the values obtained from nuclear scattering.

4.4.2 No-Core Shell Model results for ${}^6\text{He}$ and ${}^8\text{He}$

The No-Core Shell Model (NCSM) (see section 1.2.2.2) ${}^6\text{He}$ and ${}^8\text{He}$ point-proton radii and two-neutron separation energies were calculated using two different potentials: CD-Bonn 2000 and the INOY. The CD-Bonn 2000 is a meson-exchange two-body potential. The INOY potential includes a short range phenomenological two-body potential that mimics three-body effects [Dol03].

Using the CD-Bonn 2000 potential, the NCSM binding energies for ${}^6\text{He}$ and ${}^8\text{He}$ underbinds these nuclei compared to TITAN by 2.4(3) MeV and 5.4(4) MeV respectively. This is not uncommon when only a two-body potential is used. For instance, when using only the two-body AV18 potential, the GFMC values for ${}^6\text{He}$ and ${}^8\text{He}$ are underbound by 5.5(1) MeV and 8.4(1) MeV respectively. However, while the NCSM ${}^6\text{He}$ two-neutron separation energy using a CD-Bonn 2000 potential agrees within error with the TITAN value, it produces an unbound ${}^8\text{He}$ (negative S_{2N}). Again, this is not uncommon as the GFMC two-neutron separations energies values for ${}^6\text{He}$ and ${}^8\text{He}$ using only a two-body AV18 potential are -0.3(1) MeV and -0.8(1) MeV respectively. According to the authors [Cau06], having a correct two-neutron separation energy for ${}^6\text{He}$ while ${}^8\text{He}$ is unbound is said to be caused by a wrong dependence of the binding energy with the difference between the number of protons and neutrons.

However, the CD-Bonn 2000 potential correctly predicts the point-proton and matter radii of both ${}^6\text{He}$ and ${}^8\text{He}$. Although one could argue that an unbound nucleus should not have a physical extent and therefore, it should not be possible to define a charge and matter radii. This unphysical behaviour could be a combination of the faster Gaussian fall-off of the wave function compared to the expected exponential asymptotic behaviour and the small size of the Hilbert space where the calculations were performed.

The two-body INOY potential, which mimics three-body effects, binds both ${}^6\text{He}$ and ${}^8\text{He}$ as seen by their positive two-neutron separation energies. This potential reproduces very well the binding energy of ${}^6\text{He}$ while it underbinds ${}^8\text{He}$ by about 1 MeV. However, the radii predictions for ${}^6\text{He}$ strongly disagree with the measurements. For ${}^8\text{He}$, the INOY potential predicts a matter radius that is in good agreement with experiment and a slightly lower point-proton radius.

Concerning the No-Core Full Configuration [Mar09] calculations using a JISP16 potential, there is no literature value for the point-proton radius, so we only consider their two-neutron separation energy predictions. The NCFC value for the ${}^6\text{He}$ two-neutron separation energy predicts a bound state and a binding energy that gives a better agreement with the TITAN value than the NCSM with the CD-Bonn potential. This could be partly due to one of the input parameter that forms the JISP16 potential is the ${}^6\text{He}$ binding energy. However, the JISP16 results deviates more with TITAN's binding energy for ${}^6\text{He}$ compared to NCSM using the INOY potential. The ${}^8\text{He}$ binding energies and two-neutron separation energies offers similar agreement with experiment than the NCSM using the INOY potential.

In conclusion, because of the exponential behaviour of the valance neutron wave function, halo nuclei are difficult for theoretical approaches such as the NCSM (which uses wave functions with a Gaussian fall-off). Furthermore, it seems unlikely to accurately predict both their binding energy and point-proton radius with a two-body potential only.

4.4.3 Hyperspherical harmonics expansion results for ${}^6\text{He}$ and coupled cluster theory results for ${}^8\text{He}$

The hyperspherical harmonics expansion (HH) (see section 1.2.2.3) and coupled cluster theory method (CC) (see section 1.2.2.4) binding energy and two-neutrons separation energy results are shown for different cut-off Λ . This cut-off (or resolution scale) defines the size of the basis in momentum space in which the potential is defined. In principle, once all the terms in the Hamiltonian (equation (1.22)) are included, the calculation results should not depend on Λ [Bog03]. Therefore, the cut-off is varied in order to probe the effects of the non-accounted for three-nucleon interactions in the ${}^6\text{He}$ and ${}^8\text{He}$ systems. The dependance on the resolution scale have not been investigated with methods like GFMC, NCSM and NCFC.

The calculations show that for both ${}^6\text{He}$ and ${}^8\text{He}$, there is a strong dependence on the cut-off Λ and the coupled cluster calculations of ${}^8\text{He}$ underbinds this nucleus for all Λ . However, it is noticeable that the HH and CC calculations can already produce a bound state for ${}^6\text{He}$ and ${}^8\text{He}$ with only a two-body potential, which is promising. Figure 4.5 shows the preliminary point-proton radius for ${}^6\text{He}$ using HH and ${}^8\text{He}$ using CC [Bac09b]. The hyperspherical harmonics over-estimate the point-proton radius of ${}^6\text{He}$ while the coupled cluster under-estimate the point-proton radius of ${}^8\text{He}$. However, larger Hilbert space calculations are needed to confirm it.

In conclusion, both the strong dependence of the ${}^6\text{He}$ and ${}^8\text{He}$ binding

energies with Λ and the systematic underbinding of ${}^8\text{He}$ could be explained by the missing three-nucleon potential. If the two-nucleon potential was sufficient to describe ${}^6\text{He}$ and ${}^8\text{He}$, their binding energies should be independent of the cut-off (see section 1.2.3). The underbinding of ${}^8\text{He}$ could be another consequence of the missing three-nucleon interactions in the theory in analogy to what is observed in GFMC. In fact, GFMC underbinds ${}^8\text{He}$ by 8.7 MeV [Pie04] when only the two-body AV18 potential is used, but with the addition of the attractive contribution of the three-body Illinois potential, the ${}^8\text{He}$ binding energy is only 320 ± 40 keV from the TITAN value.

4.4.4 Summary

Using three different quantities: the binding energy, the two-neutron separation energy, and the point-proton radius, various ab-initio methods predictions were compared. Comparing the predictions of these methods against more than one experimental observable allows us to test the limitations of the methods. For instance, using the CD-Bonn 2000 potential, the NCSM correctly predicts the charge radius of both ${}^6\text{He}$ and ${}^8\text{He}$. However, weaknesses are revealed once we compare its predictions for the binding energies of ${}^6\text{He}$ and ${}^8\text{He}$ with experiment. We show that the inverse is also true for the INOY potential; it reproduces the binding energies but fails at predicting the point-proton radius. Such comparison questions the description of halo nuclei using two-body interactions only without explicitly studying the model dependence.

The comparison of the binding energy predictions with the experiment also confirmed the need for three-body interactions in systems comprised of more than two nucleons. This is because unlike the electromagnetic force, for the strong force the interaction between two particles is different in the presence of a third particle than when the two particles are isolated (see section 1.2.1). In section 1.2.3, we showed that calculations using only two-body potentials cannot correctly predict the binding energies of ${}^4\text{He}$ and ${}^3\text{H}$. However, once three-body potentials are included predictions closer to the experimental values for both nuclei are reached. The missing three-body potential could explain the systematic underbinding of the ${}^6\text{He}$ and ${}^8\text{He}$ nuclei resulting from the NCSM calculation using a CD-Bonn 2000, the NCFC using the JISP16 potential, the HH and CC using the V_{lowk} potential and the GFMC using only the AV18 potential as all these potentials involve only two-body interactions. Furthermore, as the number of nucleons within the nucleus increase the effect of these missing three-body interactions increases

4.4. Comparison of the results for ${}^{6,8}\text{He}$ with theory

[Pie01a]. This would explain the larger deviations seen in the binding energies of ${}^8\text{He}$ compared to ${}^6\text{He}$. Finally, the only method that performed calculations on ${}^6\text{He}$ and ${}^8\text{He}$ using three-nucleons interactions, the GFMC, gives the results that are the closest to the experimental binding energies. In conclusion, we showed that in order to have a stringent test of ab-initio methods, one needs to test their predictions for more than one observable.

Chapter 5

Summary and outlook

Modern nuclear physics is an active field of research pushing the limit of our understanding of the nucleus towards more extreme systems such as deformed nuclei [Jan91], super heavy elements [Blo10] and halo nuclei with the ultimate quest to understand the strong interaction. These studies are possible due to the recent development of radioactive beam facilities. These facilities allow the production of quantities of unstable short-lived nuclei in order to study their properties. With the development of new facilities world-wide, such as the FRIB in the US and the FAIR project in Europe, this will extend the production of larger quantities of heavier dripline nuclei.

Halo nuclei are a threshold phenomenon occurring at the verge of the neutron dripline, where the binding energy of the last few neutrons is minimal. This small neutron separation energy results in the quantum mechanical tunnelling of the valence neutrons forming an extended neutron distribution around a more confined core distribution. Explaining the extreme properties of these nuclei poses a challenge to theory. However, these nuclei can be used as test benches for ab-initio methods, which treat nucleons as effective degrees of freedom. This thesis aimed at providing accurate and precise experimental data to test ab-initio methods by probing predictions for the binding energies and charge radius of the halo nuclei ${}^6,8\text{He}$.

Key to achieving reliable experimental values for the binding energies and charge radius of ${}^6,8\text{He}$, is to perform precise and accurate direct mass measurement of these nuclei. Penning traps are the only mass spectrometer that can perform direct accurate mass measurement at the desired level of precision, in the sub-keV range. Hence the measurements were carried-out with the TITAN Penning trap mass spectrometer, which is coupled to the ISAC radioactive ion beam facility of TRIUMF. We measured the ${}^6,8\text{He}$ masses with a precisions of 54 eV for ${}^6\text{He}$ and 106 eV for ${}^8\text{He}$ and found deviations of these masses with the literature values [Aud03] of 1.7σ for ${}^8\text{He}$ and 4.0σ for ${}^6\text{He}$. The considerable increase in precision of these masses yields a significantly improved value of the charge radius while the more accurate mass value shifted the charge radius values of both nuclei.

We used the more precise and accurate TITAN masses to calculate the

point-proton radii, two-neutron separation and binding energies of ${}^6\text{He}$ and ${}^8\text{He}$. We showed that using these quantities one can test the predictions and point out potential areas of improvements of various ab-initio models. A key finding is the inconsistency of the No-Core Shell Model at predicting the correct point-proton radius while producing unbound nuclei. This unveils the importance of the asymptotic behaviour of the halo neutron wave function. We also show the importance of including three-body interactions in the effective nuclear potential to correctly describe the properties of many-body system such as ${}^6\text{He}$ and ${}^8\text{He}$.

We performed a mass measurement on ${}^6\text{Li}$ that solved a 2.3σ discrepancy between two different Penning trap mass measurements and confirmed the value from the SMILETRAP group [Nag06]. This measurement shows that the TITAN experiment can perform 10^{-9} -level mass measurements. Measurements to that level of precision and accuracy are only made possible if a detailed systematic study of the Penning trap system is performed. This led to the detailed systematic study of the Penning trap presented in this thesis. The studies included compensation of the trapping potential. We performed this compensation using two different methods in order to pin-down the combination of correction tube and guard voltage that provide the optimal compensation of the trapping potential. The resulting shift in frequency ratio due to the incomplete compensation of the trapping potential is $(\Delta R/R)_{inc.} = 0.5(5) \times 10^{-9} \cdot \Delta A$. All other known systematic effects were assigned to be below 1×10^{-9} , except for our conservative estimate on the error due to the misalignment of the trap with the magnetic field. This error is found to be $(\Delta R/R)_{mis.} = 4.2 \times 10^{-9} \cdot \Delta A$. However, there are plans to determine experimentally the size of this error. Also, both this uncertainty and the uncertainty due to the incomplete compensation of the trapping potential depends linearly with the trapping potential. These estimates are based on the large trapping potential $V_0 = 36$ V used to calculate them. Therefore, the contribution of these effects to the mass measurement systematic error can be reduced by using a smaller trapping potential.

In summary, the work presented in this thesis is important for several reasons. Firstly, we showed that precise and accurate mass measurements are important for halo nuclei. Until the mass measurement of ${}^8\text{He}$ by the TITAN experiment, no Penning trap measured the mass of a neutron-halo nuclei before. The problem residing mainly in their short half-life, typically low production yields and losses in the RFQ due to their light masses. With the highest production yields among ISOL facility for halo-nuclei, coupled with the high transfers efficiency close to 60% for light nuclei using hydrogen as buffer gas in the RFQ, the TITAN facility is a unique facility to measure

the masses of the very-short lived halo nuclei. Future halo nuclei mass measurements plans at TITAN includes the two-neutron halo ^{14}Be . The current mass value for ^{14}Be [Aud03] is based on two slightly conflicting measurements [Gil84, Wou88] that differs by 370 ± 210 keV. The resolution of this conflict through an accurate mass measurement would provide a more reliable mass for planned charge radii measurement on ^{14}Be [Nor09] and also cluster-model based description of this halo nuclei [Tar04].

Secondly, precise and accurate mass measurement are critical for the planned mass measurement of the super-allowed $0^+ \rightarrow 0^+$ β -emitter ^{74}Rb . A more accurate mass of this nuclei would help to increase the precision on the ft -value theoretical corrections and ultimately decrease the uncertainty on the V_{ud} CKM matrix element. This measurement has to be performed with a precision and accuracy of 5×10^{-9} . The mass measurement of ^6Li at a precision of 4.2×10^{-9} shows that the TITAN Penning trap is ready for such measurement and can perform an accurate mass measurement with a precision below 5×10^{-9} .

Lastly, we demonstrated that ab-initio methods can be tested by comparing the predictions for binding energy, two-neutron separation energy and point-proton radius of halo nuclei. Comparisons, for example confirmed the importance of three-nucleons interactions for systems with a larger number of nucleons than two. Two of the theoretical approaches presented, the hyperspherical harmonics expansion and coupled cluster theory are currently working on the incorporation of a three-body interactions in their calculation of the ^6He and ^8He properties [Bac09b]. It is hoped that in the near future few-nucleon systems can be well predicted based on first-principle theoretical approaches, opening the path for nuclear physics theory from a descriptive to a predictive theory. Moreover, extensions of such approaches to heavier systems seem possible.

Bibliography

- [Alk97] G.D. Alkhazov *et al.*, Phys. Rev. Lett. **78**, 2313 (1997).
- [Aud03] G. Audi *et al.*, Nucl. Phys. A **729**, 337 (2003).
- [Aue09] N. Auerbach, Phys. Rev. C **79**, 035502 (2009).
- [Bac09a] S. Bacca *et al.*, Eur. Phys. J. A **42**, 553 (2009).
- [Bac09b] S. Bacca, Private Communication
- [Bar97] N. Barnea and A. Novoselsky, Ann. Phys. **256**, 192 (1997).
- [Baz95] D. Bazin *et al.*, Phys. Rev. Lett. **74**, 3569 (1995).
- [Baz98] D. Bazin *et al.*, Phys. Rev. C **57**, 2158 (1998).
- [Bec09] D. Beck *et al.*, Nucl. Instr. and Meth. A **598**, 635 (2009).
- [Ber07] C.A. Bertulani and M.S. Hussein, Phys. Rev. C **76**, 051602(R) (2007).
- [Bir32] R.T. Birge, Phys. Rev. **40**, 207 (1932).
- [Bla06] K. Blaum, Phys. Rep. **425**, 1 (2006).
- [Blo10] M. Block *et al.*, Nature **463**, 785 (2010).
- [Bog03] S.K. Bognera, T.T.S. Kuob and A. Schwenk, Phys. Rep. **386**, 1 (2003)
- [Bol90] G. Bollen *et al.*, J. Appl. Phys. **68**, 4355 (1990).
- [Bol01] G. Bollen *et al.*, Nucl. Phys. A **693**, 3 (2001).
- [Bri08] P. Bricault *et al.*, Rev. Sci. Instrum. **79**, 02A908 (2008).
- [Bro82] L.S. Brown and G. Gabrielse, Phys. Rev. A. **25**, 2423 (1982).
- [Bro86] L.S. Brown and G. Gabrielse, Rev. Mod. Phys. **58**, 233 (1986).

Bibliography

- [Bro09] M. Brodeur *et al.*, Phys. Rev. C **80**, 044318 (2009).
- [Cab63] N. Cabibbo, Phys. Rev. Lett. **10**, 531 (1963).
- [Cak09] R.B. Cakirli *et al.*, Phys. Rev. Lett. **102**, 082501 (2009).
- [Car98] J. Carlson and R. Schiavilla, Rev. Mod. Phys. **70**, **743** (1998).
- [Cau06] E. Caurier and P. Navrátil, Phys. Rev. C **73**, 021302(R) (2006).
- [Cha09] C. Champagne, *A Retarding Field Analyser For TITAN*, M.Sc. thesis, McGill University (2009).
- [Cor09] L. Corragio *et al.*, Phys. Rev. C **80**, 044311 (2009).
- [Dah00] D.A. Dahl, Int. J. Mass. Spectr., **3**, 200 (2000).
- [Dil06] J. Dilling *et al.*, Int. J. Mass Spectr. **251**, 198 (2006).
- [Dol03] P. Doleschall *et al.*, Phys. Rev. C **67**, 064005 (2003).
- [Dom00] M. Dombisky *et al.*, Rev. Sci. Instrum. **71**, 978 (2000).
- [Dom02] M. Dombisky *et al.*, Nucl. Phys. A, **701**, 486c (2002).
- [Dra04] G.W.F. Drake, Nucl. Phys. A **737**, 25 (2004).
- [Epe02] E. Epelbaum *et al.*, Phys. Rev. C **66**, 064001 (2002).
- [Ero06] T. Eronen *et al.*, Phys. Rev. Lett. **97**, 232501 (2006).
- [Ero08] T. Eronen *et al.*, Phys. Rev. Lett. **100**, 132502 (2008).
- [Fri97] J. L. Friar, J. Martorell, and D.W.L. Sprung, Phys. Rev. A **56**, 4579 (1997).
- [Fro06] M. Froese *et al.*, Hyperfine Interact. **173**, 85 (2006).
- [Gab09] G. Gabrielse, Phys. Rev. Lett. **102**, 172501 (2009).
- [Gaz06] D. Gazit *et al.*, Phys. Rev. Lett. **96**, 112301 (2006).
- [Gil84] R. Gilman *et al.*, Phys. Rev. C **29**, 958 (1984).
- [Gla58] R.J. Glauber, *Lecture in theoretical physics* (New York, Interscience Publishers, 1958).

Bibliography

- [Gor09] S. Goriely, N. Chamel and J.M. Pearson, Phys. Rev. Lett. **102**, 152503 (2009).
- [Gos95] P.K. Ghosh, *Ion traps*, Oxford University Press (1995).
- [Gue06] C. Guénaut *et al.*, Phys. Rev. C **75**, 044303 (2007).
- [Hag06] G. Hagen, M. Hjorth-Jensen and N. Michel, Phys. Rev. C **73**, 064307 (2006).
- [Hag07a] G. Hagen *et al.*, Phys. Lett. B **656**, 169 (2007).
- [Hag07b] G. Hagen *et al.*, Phys. Rev. C **76**, 034302 (2007).
- [Hak08] J. Hakala *et al.*, Phys. Rev. Lett. **101**, 052502 (2008).
- [Han87] P.G. Hansen and B. Jonson, Europhys. Lett., **4** (4), 409 (1987).
- [Har05] J.C. Hardy and I.S. Towner, Phys. Rev. C **71**, 055501 (2005).
- [Har09] J.C. Hardy and I.S. Towner, Phys. Rev. C **79**, 055502 (2009).
- [Hax49] O. Haxel, Phys. Rev. **75**, 1766 (1949).
- [Hea01] T.P. Heavner, S.R. Jefferts, G.H. Dunn, Phys. Rev. A **64**, 062504 (2001).
- [Jan91] R.V.F. Janssens *et al.*, Annu. Rev. Nucl. Part. Sci. **41**, 321 (1991).
- [Jen04] A.S. Jensen *et al.*, Rev. Mod. Phys. **76**, 215 (2004).
- [Jon04] B. Jonson, Phys. Rep. **389**, 1 (2004).
- [Jur09] E.D. Jurgenson, P. Navrátil and R.J. Furnstahl, Phys. Rev. Lett. **103**, 082501 (2009).
- [Kan02] R. Kanungo *et al.*, Phys. Lett. B **528**, 58 (2002).
- [Kar75] P.J. Karol, Phys. Rev. C **11**, 1203 (1975).
- [Kel03] A. Kellerbauer *et al.*, Eur. Phys. J D **22**, 53 (2003).
- [Kel04] A. Kellerbauer *et al.*, Phys. Rev. Lett. **93**, 072502 (2004).
- [Kis05] O.A. Kiselev *et al.*, Eur. Phys. J. A **25**, s01, 215 (2005).
- [Kra88] K.S. Krane, *Introductory nuclear physics* (Hoboken, John Wiley and Sons, 1988).

Bibliography

- [Kre91] M. Kretschmar, Eur. J. Phys. **12**, 240 (1991).
- [Kre08] M. Kretschmar, Int. J of Mass Spec. **275**, 21 (2008).
- [Kob73] M. Kobayashi and K. Maskawa, Prog. Theor. Phys. **49**, 652 (1973).
- [Kop97] S. Kopecky *et al.*, Phys. Rev. C **56**, 2229 (1997).
- [Kon95] M. König *et al.*, Int. J. Mass Spectr. Ion. Proc., **142**, 95 (1995).
- [Kou75] R. Kouzes and W.H. Moore, Phys. Rev. C, **12**, 1511 (1975).
- [Lia09] H. Liang *et al.*, Phys. Rev. C **79**, 064316 (2009).
- [Lor82] C.J. Lorenzen and K. Niemax, J. Phys. B **15**, L139 (1982).
- [Mac01] R. Machleidt, Phys. Rev. C **63**, 024001 (2001).
- [Mac07] R. Machleidt, arXiv:0704.0807v1.
- [Mar87] W.J. Marciano and A. Sirlin, Phys. Rev. D **35**, 1672 (1987).
- [Mar09] P. Maris, J.P. Vary and A.M. Shirokov, Phys. Rev. C **79**, 014308 (2009).
- [May49] M.G. Mayer, Phys. Rev. **75**, 1969 (1949).
- [Mil09] G.A. Miller and A. Schwenk, Phys. Rev. C **80**, 064319 (2009).
- [Min92] T. Minamisono *et al.*, Phys. Rev. Lett. **69**, 2058 (1992).
- [Mue07] P. Mueller *et al.*, Phys. Rev. Lett. **99**, 252501 (2007).
- [Mye96] W.D. Myers and W.J. Swiatecki, Nucl. Phys. A **601**, 141 (1996).
- [Nag06] S. Nagy *et al.*, Phys. Rev. Lett. **96**, 163004 (2006).
- [Nav07] P. Navrátil *et al.*, arXiv:0711.2702v1 [nucl-th] (2007).
- [Nes01] A.V. Nesterov, V.S. Vasilevsky, O.F. Chernov, Phys. of Atom. Nucl. **64**, 1409 (2001).
- [Nog04] A. Nogga, S.K. Bogner and A. Schwenk, Phys. Rev. C **70**, 061002(R) (2004).
- [Nor09] W. Nörtershäuser *et al.*, Phys. Rev. Lett. **102**, 062503 (2009).
- [Oga92] Y. Ogawa, Y. Suzuki, K. Yabana, Nucl. Phys. A, **543**, 722 (1992).

Bibliography

- [Orm95] W.E. Ormond and B.A. Brown, Phys. Rev. C **52**, 2455 (1995).
- [Ott87] W.E. Otten, *Nuclear Radii and Moments of Unstable Isotopes* (New York, Plenum Press, 1987).
- [Oza00] A. Ozawa *et al.*, Phys. Rev. Lett. **84**, 5493 (2000).
- [Oza01] A. Ozawa *et al.*, Nucl. Phys. A **691**, 599 (2001).
- [Pie01a] S.C. Pieper and R.B. Wiringa, Annu. Rev. Nucl. Part. Sci. **51**, 53 (2001).
- [Pie01b] S.C. Pieper *et al.*, Phys. Rev. C **64**, 014001 (2001).
- [Pie04] S.C. Pieper, R.B. Wiringa and J. Carlson, Phys. Rev. C **70**, 054325 (2004).
- [Pie05] S.C. Pieper, Nucl. Phys. A **751**, 516c (2005).
- [Pie07] S.C. Pieper, arXiv0711.1500, Proceeding of Enrico Fermi School (2007).
- [Pud95] B.S. Pudlinger *et al.*, Phys. Rev. Lett. **74**, 4396 (1995).
- [Rin07] R. Ringle *et al.*, Int. J. Mass Spectr. **263**, 38 (2007).
- [Rin09a] R. Ringle *et al.*, Phys. Lett. B **675**, 170 (2009).
- [Rin09b] R. Ringle *et al.*, Nucl. Instr. and Meth. A **604**, 536 (2009).
- [Ryj08] V. Ryjkov *et al.*, Phys. Rev. Lett. **101**, 012501 (2008).
- [San06] R. Sánchez *et al.*, Phys. Rev. Lett. **96**, 033002 (2006).
- [Sav04] G. Savard *et al.*, Phys. Rev. Lett. **95**, 102501 (2005).
- [Sav05] G. Savard *et al.*, Phys. Rev. Lett. **95**, 102501 (2005).
- [Sci08] B. Sciascia and the FlaviaNet Kaon Working Group, Nucl. Phys. Proc. Suppl. **181**, 83 (2008).
- [Sch06] H. Schatz, Int. J. Mass Spectrom. **251**, 293 (2006).
- [Sic82] I. Sick, Phys. Lett. B **116**, 212 (1982).
- [Smi06] M. Smith *et al.*, Hyperfine Interact. **173**, 171 (2006).

Bibliography

- [Smi08a] M. Smith, *A Mass Measurement of the Short-lived Halo Nucleus ^{11}Li with the TITAN Penning Trap Spectrometer*, Ph.D. thesis, University of British Columbia (2008).
- [Smi08b] M. Smith *et al.*, Phys. Rev. Lett. **101**, 202501 (2008).
- [Tan85a] I. Tanihata *et al.*, Phys. Rev. Lett. **55**, 2676 (1985).
- [Tan85b] I. Tanihata *et al.*, Phys. Lett. B **160**, 380 (1985).
- [Tan88] I. Tanihata *et al.*, Phys. Lett. B **202**, 592 (1988).
- [Tan92] I. Tanihata *et al.*, Phys. Lett. B **289**, 261 (1992).
- [Tan10] K. Tanaka *et al.*, Phys. Rev. Lett. **104**, 062701 (2010).
- [Tar04] T. Tarutina, I.J. Thompson and J.A. Tostevin, Nucl. Phys. A **733**, 53 (2004).
- [Tes97] G. Testera *et al.*, Hyperfine Interact. **109**, 303 (1997).
- [Tjo75] J.A. Tjon, Phys. Lett. B **56**, 217 (1975).
- [Tow77] I.S. Towner *et al.*, Nucl. Phys. A **284**, 269 (1977).
- [Tow02] I.S. Towner and J. C. Hardy, Phys. Rev. C **66**, 035501 (2002).
- [Tri77] R.E. Tribble *et al.*, Phys. Rev. C **16**, 1835 (1977).
- [Var94] K. Varga, Y. Suzuki and Y. Ohbayasi, Phys. Rev. C **50**, 189 (1994).
- [Von77] H. Vonach *et al.*, Nucl. Phys. A **278**, 189.
- [Wan04] L.B. Wang *et al.*, Phys. Rev. Lett. **93**, 142501 (2004).
- [Wir95] R.B. Wiringa, V.G.J. Stoks and R. Schiavilla, Phys. Rev. C **51**, 38 (1995).
- [Wou88] J.M. Wouters *et al.*, Z. Phys. A **331**, 229 (1988).
- [Yao06] W.-M. Yao *et al.* (Particle Data Group), J. Phys. G **33**, 1 (2006).
- [Yos07] Yoshiko Kanada-En'yo, Phys. Rev. C **76**, 044323 (2007).
- [Yuk34] H. Yukawa, Proc. Phys. Math. **17**, 48 (1935).

Appendix A

Ion beam capture optimization

The proper capturing of the ion bunches in the Penning trap is critical to have an optimal cyclotron frequency determination. Ideally, once captured, the ions bunches should have minimal kinetic energy. Any residual kinetic energy results in the ion oscillating axially in the trap. Large axial oscillation amplitudes causes the ions to venture in region of the trapping potential that have are inevitably non-harmonic, which results in a change in the ion's cyclotron frequency (see section 3.2.3 and 3.3 for more details). Also, if the initial energy of the ions is comparable to their energy gain at the end of the magnetron to reduced cyclotron conversion phase, this results in a reduction of the time-of-flight effect. This effect is shown in figure A.1 for ${}^7\text{Li}^+$ ions. This figure shows the effect of the closing time of the trap on the time-of-flight resonance spectra. The data in red correspond to an optimal capturing, while the blue data correspond to a capturing where the trap is closed $\Delta t_{cap} = 1 \mu\text{s}$ too soon. The effect of closing the trap not at the right time is obvious from figure A.1. Firstly, the blue curve in figure A.1 (a) shows that more ions arrives with short time-of-flight that are comparable to on-resonance ions (shown by a “bump” in the red curve at a time-of-flight of $16 \mu\text{s}$). This results in a reduction of the amplitude of the time-of-flight resonance as shown by the blue curve in figure A.1 (b). This figure also shows that this can cause a change in the cyclotron frequency. In this section we explain how the ion capturing in the Penning trap is optimized.

The ion bunch capturing in the Penning trap is optimized by adjusting the closing time of the trap and ion energy upon capture. This energy depends on several factors. Firstly, the transport energy E of the beam, which depends on the potential difference between the RFQ high voltage potential and the RFQ pulse drift tube potential. Secondly, the potentials applied on the drift tube prior to the Penning trap. The role of this drift tube is to remove most of the ions energy without perturbing them. This is done by applying a potential $V_{PLT(+)}$ on the drift tube that is about 65 V below the beam energy and once the ions reach the drift tube centre, we

Appendix A. Ion beam capture optimization

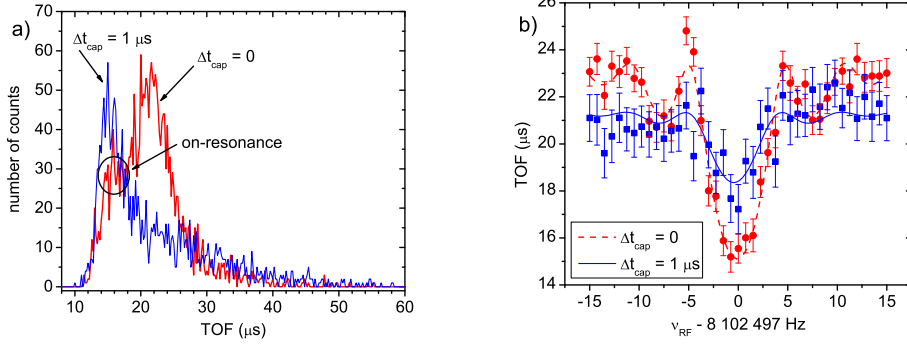


Figure A.1: a) ${}^7\text{Li}$ time-of-flight distribution for an ideal capture timing $\Delta t_{cap} = 0 \mu s$ and when the ions are captured $1 \mu s$ too soon. b) Corresponding TOF spectra. Note the shift in frequency and the reduction in the TOF resonance amplitude.

pulse its potential down below ground potential. Then, the ion beam energy leaving the drift tube is simply $E - V_{PLT(+)}$. In order to have the ions stop once they reach the trap centre, we adjust the low voltage of the pulse drift tube $V_{PLT(-)}$ until $V_{PLT(-)} \approx E - V_{PLT(+)}$.

The effect of the trap closing time t_{cap} and the pulse drift tube low potential $V_{PLT(-)}$ on the axial oscillations of the ions in the trap has been simulated using SIMION [Dah00]. For this simulation, we used singly charged ions with mass number $A = 6$, a beam energy of $E = 1993 \text{ eV}$ and a drift tube high potential $V_{PLT(+)} = 1936 \text{ V}$. Figure A.2 is a contour plot that shows the results of this simulation. The contours represent different size of axial oscillations amplitude in mm. Figure A.2 shows that the size of the axial oscillation amplitudes is very sensitive with the capture timing when $V_{PLT(-)}$ is at its optimal value. At this point, the amplitude of the bunches grows with a rate of about $1 \text{ mm}/100 \text{ ns}$. The amplitude of the axial oscillations are also sensitive to $V_{PLT(-)}$, considering that a change in the beam energy of 5 eV is enough to change the amplitude by 4 mm . This makes the ion capturing in the Penning trap particularly sensitive on the ion energy.

The optimal injection setting in the trap are found using two different methods. In the first method we adjust the closing time of the trap and the pulse drift tube low potential in order to minimize the width of the time-of-flight distributions. If no RF excitation of the ions is performed, they should

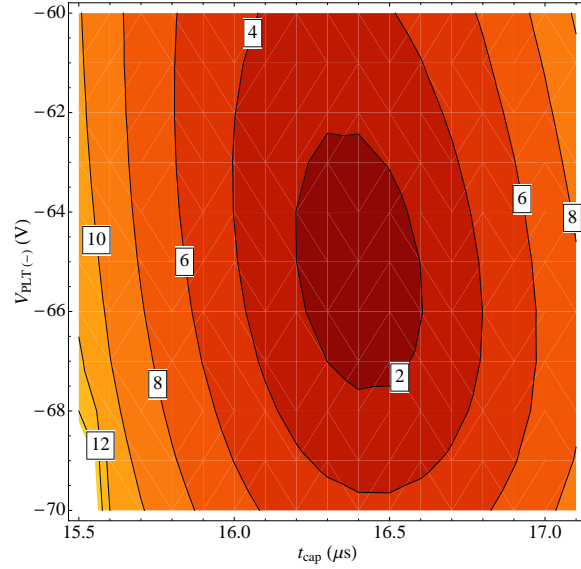


Figure A.2: Variation of the axial amplitudes (shown in the boxes, in mm) of the ions in the Penning trap as a function of the capture timing and the low level of the pulse drift tube.

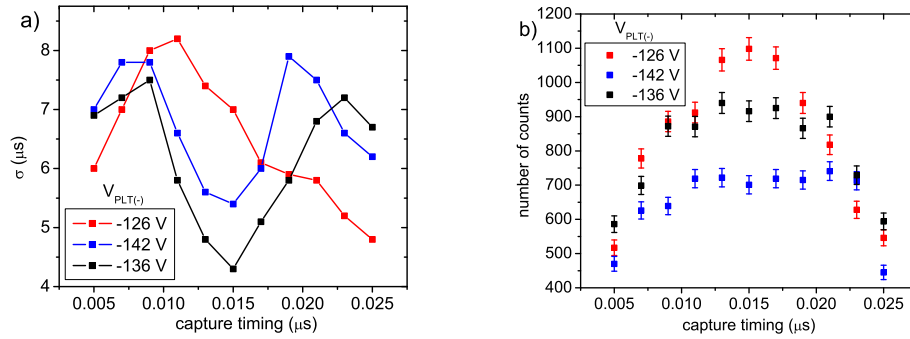


Figure A.3: a) TOF distribution width as a function of the capture timing for various MPET PTL negative voltages $V_{\text{PLT}(-)}$ (lines are guide to the eye). b) Corresponding number of counts recorded on the MPC. See text for more details.

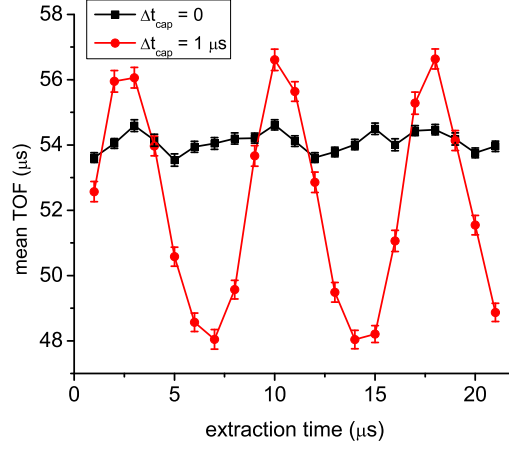


Figure A.4: Variation of the mean time-of-flight as a function of the extraction time of the ions from the Penning trap for ^{39}K . $\Delta t_{cap} = 0$ is the optimal capture timing.

arrive on the detector with similar time. The minimal spread in their arrival time should be dictated by the initial energy spread and spacial extent of the bunch. When the ions still have some kinetic energy once captured, their spread in time-of-flight between their extraction and arrival to the detector is larger as evidenced by the blue curve in figure A.1 (a). Therefore, one can optimize the capturing by finding the trap closing time t_{cap} and pulse drift tube low potential $V_{PLT(-)}$ that minimizes the time-of-flight width.

Figure A.3 (a) shows the time-of-flight width σ as a function of the capture timing for three different pulse drift tube low potential $V_{PLT(-)}$. The optimal capture occurs for $V_{PLT(-)} = -136$ V and $t_{cap} = 1.5$ μs , where the width σ is minimal. Figure A.3 (b) shows that this timing also corresponds to where number of detected ions is maximal. For $V_{PLT(-)} = -142$ V, there is generally less ions getting in the trap and this is because the pulse drift tube low potential is too small, causing the beam to have too little energy to reach the trap centre. At the opposite, more counts are seen for $V_{PLT(-)} = -126$ V, which corresponds to a more energetic beam injected into the Penning trap than the optimal $V_{PLT(-)} = -136$ V. This might be because for the optimal setting, the ions with lower kinetic energy cannot make it into the trap.

The second method involves a more direct measurement of the axial oscillations amplitude. In this method, the mean time-of-flight of the ion bunch leaving the trap is plot as a function of a delay in the extraction time from the Penning trap. By changing this delay, the ions bunches leaves the Penning trap when they are in different position in the trap resulting in a sinusoidal change in the mean TOF with the extraction time. As we discussed previously, when the ions are captured with minimal energy in the centre of the trap, their axial oscillation amplitude is minimal, which results in a minimal variation in the mean TOF.

An example of these sinusoidal fluctuations in shown in figure A.4 for two different capture timing for ^{39}K . This figure shows that for a proper capture timing ($\Delta t_{cap} = 0$), the change in the amplitude is minimal as expected. For an improper capture timing, the amplitude of the oscillations are significantly larger and the centroid of these oscillations is shifted towards smaller time-of-flight as a result of the larger kinetic energy of the ion in the Penning trap. In conclusion, the ion beam captured in the Penning trap can be optimized using two different techniques in order to ensure that the ions have minimal axial oscillations amplitude in the trap.